A NEW METHOD OF CALCULATING VERTICAL MOTION IN ISENTROPIC SPACE

A Thesis

presented to

the Faculty of the Graduate School

at the University of Missouri-Columbia

In Partial Fulfillment

of the Requirements for the Degree

Soil, Environmental, and Atmospheric Sciences

---

by

MICHEAL JOSEPH SIMPSON

Dr. Patrick Market, Thesis Supervisor

MAY 2014

The undersigned, appointed by the dean of the Graduate School, have examined the thesis entitled

A New Method of Calculating Vertical Motion in Isentropic Space

presented by Micheal Simpson,

a candidate for the degree of master of atmospheric science, and hereby certify that, in their opinion, it is worthy of acceptance.

Professor Patrick Market

Professor Anthony Lupo

Professor Jason Hubbart

Professor Scott Rochette

This thesis is dedicated to my parents, who have never stopped believing in me. Without their love and support, the opportunity to write this paper would not have been possible.

ACKNOWLEDGEMENTS

The Weather Forecast Office in Springfield, Missouri provided the impetus for the writing of this paper; without the individuals at this office, this paper would not have been possible. I am eternally grateful to everyone at the Springfield WFO. Dr. Scott Rochette and Dr. Patrick Market must be thanked for serving as my advisors and helping me get to where I am today. My committee members: Dr. Patrick Market, Dr. Scott Rochette, Dr. Anthony Lupo, and Dr. Jason Hubbart for taking the time and effort to be on my committee; their guidance as professionals is inspiring and appreciated beyond words. Dr. Neil Fox and Andrew Jensen have helped with the writing and mathematics of this paper, and their help is greatly appreciated.

TABLE OF CONTENTS

LIST OF ILLUSTRATIONS

LIST OF TABLES

A NEW METHOD OF CALCULATING VERTICAL MOTION IN ISENTROPIC SPACE

Micheal Simpson

Dr. Patrick Market, Thesis Supervisor

ABSTRACT

A full isentropic vertical motion (ω_θ) has long been difficult to calculate in an operational forecasting environment. However, recent interactions with the Springfield, MO National Weather Service Office spurred the development of the current method of estimating the total ω_θ. During the winter of 2012-13, this expression was developed into its current form, and initial tests were undertaken to test its usefulness. Using output from NCEP's operational WRF-NAM model, individual points were evaluated for isentropic surfaces RH values $\geq$ 95% and compared against the existing isobaric omega (ω) as a truth value. Results show that the difference between ω_θ and ω, or ADER, performed best on isentropic surfaces closer to the ground, with an overall trend of better performance the further the forecast was from the initialization time. As the area of calculations decreased from 17x17 to a 7x7 grid-space each at 80km apart, errors were reduced by nearly an order of magnitude. The inclusion of the diabatic term to the isentropic vertical motion equation has been demonstrated to reveal average over-estimated errors of 2μbs^{-1}.

Chapter 1: Introduction

When studying the atmosphere, one is essentially implementing the study of geophysical fluid dynamics (Pedlosky 1992). Although operational meteorology has a relatively short history nearly 100 years old, it has made tremendous steps towards understanding the nature of the atmosphere. However, there is still much that is not understood since the atmosphere is a complex dynamically-coupled chaotic system (Lorenz 1963).

The history of numerical weather prediction (NWP) can be traced back to Cleveland Abbe (Abbe 1901), but, arguably, became popularized by Lewis Fry Richardson's first attempt at an actual numerical weather forecast (Richardson 1922; Ashford 1985; Lynch 2008). It was not until the advent of the computer and computational efficiency of such computers to allow for NWP to first occur. The Electronic Numerical Integrator and Computer (ENIAC) generated the first forecasts in 1950 (Charney et al. 1950). The computational power has increased exponentially ever since the ENIAC (Moore 1965; Mack 2011), resulting in atmospheric models that are in use today, including the Global Forecast System (GFS), Weather and Research Forecast model-North-American Mesoscale (WRF-NAM, hereafter NAM), and the recently developed flow-following finite-volume icosahedral model (FIM). The main differences between these models are their basic physical computations, cumulus parameterization schemes, and choice of coordinate system in simulating the atmosphere (Arakawa 2004; Yang 2011).

Hess (1959) described the three most applicable branches of physics pertaining to atmospheric science as hydrodynamics, thermodynamics, and radiation. These three fields of physics when applied to the atmosphere can be used to describe the general circulation, overall movement of storm systems, and upward vertical motions (UVM's). Arguably, one of the most significant forecasting parameters is UVM. This is because past the lifted condensation level (LCL),

a parcel that continues to rise will undergo diabatic processes including latent heat release (LHR). In the conventional isobaric framework, there is no direct means of measuring the amount of diabatic heating gain or loss when calculating UVM, or ω, which is simply:

$$\omega = \frac{dp}{dt} \tag{1.1}$$

where *p* is pressure and *t* is time. As noted in Moore (1993), isentropic surfaces can have slopes of 1-2 orders of magnitude greater than a corresponding pressure surface. Therefore, the adiabatic component of vertical motion in an isentropic framework is included along horizontal flow, as opposed to a separate computation in isobaric coordinates. This is more evident when observing the isentropic ω-equation:

$$\omega_\theta = (\frac{\partial P}{\partial t})_\theta + \vec{V} \cdot \nabla_\theta P + \frac{\partial P}{\partial \theta}\frac{d\theta}{dt} \tag{1.2}$$

with θ designating potential temperature, $\vec{V}$ is the total vector wind, and subscripts of θ indicate derivative operations carried out in isentropic space. The third term on the RHS of (1.2) is the diabatic contribution and can cause parcels that were once thermodynamically bound to the surface to 'jump' off to a higher (lower) isentropic level through condensation (evaporation). However, calculating numerical values for $\frac{d\theta}{dt}$ is an arduous task (Byers 1939).

It was previously assumed that the first term (the local pressure tendency) is equal and opposite to the third term, leaving the pressure advection term dominant (Saucier 1955; Uccellini 1976; Moore 1993). Uccellini (1976) stated that this assumption is most effective when winds speeds are strong and directed along the pressure gradient. However, work done by Market et al. (2000) showed that this was not always a valid assumption. As part of their analysis where only the diabatic term was omitted in (1.2), two-thirds of the total ω_θ was observed and inclusion of the local pressure tendency term with the transport term yielded better results than the transport term alone.

However, the diabatic term is not as easily calculated as the other two terms in equation 1.2. The diabatic term in (1.2) was reconstructed by Emanuel et al. (1987) from a Lagrangian to an Eulerian framework. Cammas et al. (1994) expanded upon this work, resulting in a final form of the diabatic term in (1.2) as follows:

$$\frac{d\theta}{dt} = \omega\left[\frac{\partial\theta}{\partial p} - \frac{\theta}{\theta_e}\frac{\Gamma_m}{\Gamma_d}\frac{\partial\theta_e}{\partial p}\right] \tag{1.3}$$

where θ_e is the equivalent potential temperature, and Γ_m and Γ_d are the moist and dry adiabatic lapse rates, respectively.

This thesis will substitute the diabatic term shown in (1.3) into (1.2), and calculate the total vertical motion in isentropic space. Upon doing so, the calculation of the isentropic vertical velocity in (1.2) will be available from real time data, providing an easier method of calculating ω_θ. Using the General Meteorological Package (GEMPAK) software and the GEMPAK Analysis and Rendering Package (GARP), each variable was plotted and their respective values were used to quantify the total vertical motion from NAM data imported daily at 00Z and 12Z. This will, in turn, be compared to the actual vertical motion (ω). A difference field between the total isentropic vertical motion and the isobaric form of omega will be calculated to observe how accurate eqn. (1.2) is. For this study, it is assumed that eqn. (1.1) is the accepted value, and therefore the difference field will simply be $\omega_\theta - \omega$. It was anticipated that the isentropic vertical motion will be a helpful aid to WFO's across the country through the implementation of the derived expression as a means of easily calculating the diabatic term in (1.2). The expression presented derived in Chapter 3 will be expected to perform with minimal error in comparison to ω, where $|\omega_\theta - \omega| < 3\ \mu bs^{-1}$.

Chapter 2: Literature Review

To fully understand the work built upon the isentropic framework, this section provides a literature review of several papers that either directly implements isentropic coordinates (e.g., Byers 1939; Keyser and Johnson 1984) or lays foundation for their future use (e.g., Starr 1946). Each paper analyzed will detail the main purpose of the study, how it was carried out, and how it pertains to the isentropic framework.

Some of the earliest work with isentropic charts was by Byers (1939) who stated that isentropic analysis serves not only a thermodynamic purpose that indicates adiabatic changes of the air, but also a hydrodynamic purpose by representing moisture "tongues" which serve as identifying indicators of the flow pattern; this paper analyzes the former but concludes that many hydrodynamic advantages appear as well. Byers (1939) defined the isentropic-condensation pressure as the pressure of the condensation level in an adiabatic process, while specific humidity (q) remains unchanged. This is defined as:

$$C = p\left(\frac{T_0}{T}\right)^{\frac{mC_p}{R}} \tag{2.1}$$

where m is the molecular weight of dry air, C_p is the specific heat of dry air under constant pressure, R is the universal gas constant, and T_0 is the temperature at P_0, or the initial pressure. Through the use of this equation, Byers (1939) argued that C-isobars on an isentropic chart are better than isograms of q for representing significant moisture differences at low values of specific humidity. The slope of the C-isobars are much more evident on an isentropic chart than that of q (by nearly an order of magnitude). It was also shown that isobars are isosteres and isopycnics through the following relationship:

$$\frac{1}{\alpha} = \frac{R}{m}\frac{\theta}{c}P^{k-1} \tag{2.2}$$

where $c = 1000^k$ and $k = \frac{mC_p}{R}$. Through multiple examples of these equations, Byers (1939) summarized his work with a short list of why isentropic charts are advantageous over elevation charts:

1) Better representation of significant moisture differences at low values, as well as moist tongues at low temperatures are revealed more readily.

2) Nearness to condensation can be determined by the condensation ratio, or simple C/P, which is the only expression of the nearness to saturation that is of direct thermodynamic significant in an isentropic process.

3) The weight of air in the layers between isentropic surfaces can be easily calculated.

4) Cold lows appear as regions of greater activity and warm highs as less activity than on any other type of chart.

In his final remark, Byers states there is no apparent reason why isentropic charts are not preferable for practically all uses, especially when compared to isobaric analysis.

In 1945, Starr wrote a paper detailing the hydrodynamic equations, making an initial statement that additional frames of reference aside from the Eulerian and Lagrangian should be formulated depending on the specific problem being assessed. In essence, the author asserted that geophysicists must be more cognizant to devise means to treat the problem of hydrodynamics as heterogeneous, as opposed to homogeneous. A blend of the Eulerian and Lagrangian systems were devised by Starr (1945) to render the treatment of heterogeneous fluid motion where the stratification is purely horizontal.

Beginning with a fluid in motion relative to the Cartesian coordinate system (x,y,z surfaces), at some arbitrary time later the space of fluid is occupied by a family of nonintersecting surfaces which do not depart in the horizontal. These surfaces will be denoted as c, and will be considered the continuous variable. Next, z will be the dependent variable whereas x, y, c, and t are the independent variables. An element of volume with vertical and horizontal dimensions δx and δy (respectively), bounded by the surfaces $c = c1$ and $c = c1 + \delta c$, the geometric vertical thickness will be $(\partial z/\partial c)\delta c$, Thus allowing for a conservation of mass relationship to be derived:

$$\frac{d}{dt}\left(\rho\frac{\partial z}{\partial c}\delta x\delta y\delta c\right) = 0 \tag{2.3}$$

where ρ is density. However, since δx and δy are changing due to velocity gradients along material surfaces of constant c, (2.3) becomes:

$$\frac{d}{dt}\left(\rho\frac{\partial z}{\partial c}\right) = -\rho\frac{\partial z}{\partial c}\left(\frac{\partial u}{\partial x}+\frac{\partial v}{\partial y}\right) \tag{2.4}$$

It should be noted that no assumptions as to the compressibility or homogeneity have been made, thus making (2.4) a perfectly general relationship. The independent variable c may be chosen in an arbitrary fashion, such as that for conservative flows, namely potential temperature. Further, assuming a stably stratified fluid, the medium is in hydrostatic balance, and if one assumes an initial rectangular projection at time $t = 0$, then at $t = t+\Delta t$ the projection will be that of a parallelogram. The final continuity equation in a Cartesian framework can be written as:

$$\frac{\partial p}{\partial c} = \frac{\partial p_0}{\partial c}\left(\frac{\partial x_0}{\partial x}\frac{\partial y_0}{\partial y}-\frac{\partial y_0}{\partial x}\frac{\partial x_0}{\partial y}\right) \tag{2.5}$$

A "flow function" is further defined as a streamfunction in the arbitrary x, y, and c framework, denoted by χ. Along the x and y directions, respectively, one can obtain:

$$\rho u \frac{\partial z}{\partial c} = -\frac{\partial \chi}{\partial y} (2.6) \qquad \rho v \frac{\partial z}{\partial c} = \frac{\partial \chi}{\partial x} \qquad (2.7)$$

There is no stipulation which would preclude the case where surfaces of constant c coincide with a surface of constant physical or geometric property within a given parcel, whether it is conservative or not. The equations of motion for an arbitrary *x, y, c* space will undergo simple change of variables in the corresponding Cartesian Eulerian framework. It can be shown that through geometric considerations:

$$(\frac{\partial \mu}{\partial x})_z = (\frac{\partial \mu}{\partial x})_c - (\frac{\partial \mu}{\partial x})_c \frac{(\frac{\partial \mu}{\partial c})_x}{(\frac{\partial z}{\partial c})_x} \qquad (2.8)$$

where μ is any continuous variable and the subscripts indicate that the differentiation is performed on the assumption that the designated variable is held constant. Introducing relationships of this type into the equations of motions, one will achieve:

$$\rho \frac{\partial z}{\partial c} \frac{du}{dt} = 2\Omega sin\phi \rho v \frac{\partial z}{\partial c} - 2\Omega cos\phi \rho w \frac{\partial z}{\partial c} + \frac{\partial z}{\partial x} \frac{\partial p}{\partial c} - \frac{\partial p}{\partial x} \frac{\partial z}{\partial c} \qquad (2.9)$$

$$\rho \frac{\partial z}{\partial c} \frac{dv}{dt} = -2\Omega sin\phi \rho u \frac{\partial z}{\partial c} + \frac{\partial z}{\partial y} \frac{\partial p}{\partial c} - \frac{\partial p}{\partial y} \frac{\partial z}{\partial c} \qquad (2.10)$$

$$\rho \frac{\partial z}{\partial c} \frac{dw}{dt} = -\rho g \frac{\partial z}{\partial c} + 2\Omega cos\phi \rho u \frac{\partial z}{\partial c} - \frac{\partial p}{\partial c} \qquad (2.11)$$

which are the general equations of motion in an arbitrary *x, y,* and *c* framework. In most meteorological practices, $2\Omega cos\phi$ and *dw/dt* are assumed to be negligible through scale analysis, reducing (2.9) - (2.11) to:

$$\frac{du}{dt} = 2\Omega sin\phi v - \frac{1}{\rho} \frac{\partial p}{\partial x} - g \frac{\partial z}{\partial x} \qquad (2.12)$$

$$\frac{dv}{dt} = -2\Omega sin\phi u - \frac{1}{\rho} \frac{\partial p}{\partial y} - g \frac{\partial z}{\partial y} \qquad (2.13)$$

$$\frac{\partial p}{\partial c} = -\rho g \frac{\partial z}{\partial c} \tag{2.14}$$

Through this work done by Starr (1945), authors have implemented this approach to develop atmospheric models with differing vertical coordinates, including hybrid models of sigma (surface) and isentropic surfaces (Bleck, 1978; Webster et al. 1999; Benjamin et al. 2004).

Danielsen (1961) built upon previous work by studying the actual air trajectory of an air parcel in an isentropic and isobaric framework for several different cases. Danielsen (1961) argued that more attention will be focused on isentropic trajectories rather than isobaric for their three-dimensional aspect and direct incorporation of vertical motions and velocity shears, eliminating the major sources of error in isobaric trajectories. Analyzing the vector errors between the two trajectories is advantageous to be expressed as functions of vertical velocities and diabatic rates, enabling order-of-magnitude comparisons. r' and z' are denoted as the horizontal and vertical components of the difference vectors, respectively, and are defined as:

$$r'_{p,\theta} = \iint \left[\left(W - W_{p,\theta}\right)\frac{\partial V}{\partial Z} + \left(r'\frac{\partial}{\partial r} + z'\frac{\partial}{\partial z} + \cdots \left(\frac{dV}{dt}\right)\right)\right](dt)^2 \tag{2.15}$$

$$z'_{p,\theta} = \iint \left[\left(W - W_{p,\theta}\right)\frac{\partial V}{\partial Z} + \left(r'\frac{\partial}{\partial r} + z'\frac{\partial}{\partial z} + \cdots\right)\right](dt) \tag{2.16}$$

The other terms are as follows: subscripts p and θ denote pressure and isentropic surfaces, respectively, V is the horizontal wind component, and W is the vertical velocity of the air. The horizontal acceleration, vertical wind shear, and vertical velocity at the position of the air parcel have been replaced by their Taylor expansions. As r' and z' increase, the x, y, and z components of the wind will act in the same sense due to the correlation of geostrophic departures, vertical motion, and velocity shears in a baroclinic fluid. Danielsen (1961) showed that through small and large diabatic/stability rates, isentropic trajectories remain close to the measured air parcel, i.e. the higher

ordered terms in the Taylor expansion can be neglected. All trajectories were of the subsidence type to eliminate large diabatic phase changes. Also, if diabatic rates are small, the conservation of potential vorticity, vorticity, and mixing ratio (stability) measured from a nearby radiosonde would ensure the reliability of the isentropic trajectories. Danielsen (1961) concluded that the trajectory of an isobaric parcel is drastically different from the trajectory of the air in regions of large values of *W* (Figure 2.1). The trajectories may deviate up to 1000km and the curvature may be of opposite sign. Isentropic trajectories, however, deviate only slightly from the true air parcel trajectory (with average values of stability and diabatic rates). Finally, a derivation of isentropic trajectories from the energy equation is presented as a means of reliably tracing water vapor, ozone, and radioactive materials:

$$\int \frac{\partial \Psi}{\partial t} dt = (\Psi_2 - \Psi_1) + \frac{{V_2}^2 - {V_1}^2}{2} + \overline{\frac{\partial}{\partial \theta}\left(\frac{V^2}{2}\right)} (\theta_2 - \theta_1) \tag{2.17}$$

where Ψ is the Montgomery streamfunction, and subscripts 1 and 2 denote the initial and final trajectory times, respectively. This final point, Ψ_2, will be satisfied under the following conditions:

$$\Psi_2 - \Psi_1 + \frac{{V_2}^2}{2} - \frac{{V_1}^2}{2} \approx \frac{\Delta\Psi_2 + \Delta\Psi_1 + 2\Delta\Psi_M}{4} \tag{2.18}$$

$$D \approx \frac{V_2 + V_1}{2} \Delta t \tag{2.19}$$

where *M* denotes the midpoint, Δt is the time taken for the system to travel, and *D* is the distance traveled by the system

Following Danielsen's work, Bleck (1973) published a paper investigating the conservation of potential vorticity in four case examples. The first section of his paper offered an extensive background on the initial research of isentropic coordinates, and why they were ultimately replaced by isobaric coordinates. He then discussed the concept of potential vorticity (PV), which is derived by eliminating the velocity divergence term between the continuity and vorticity equations. Bleck

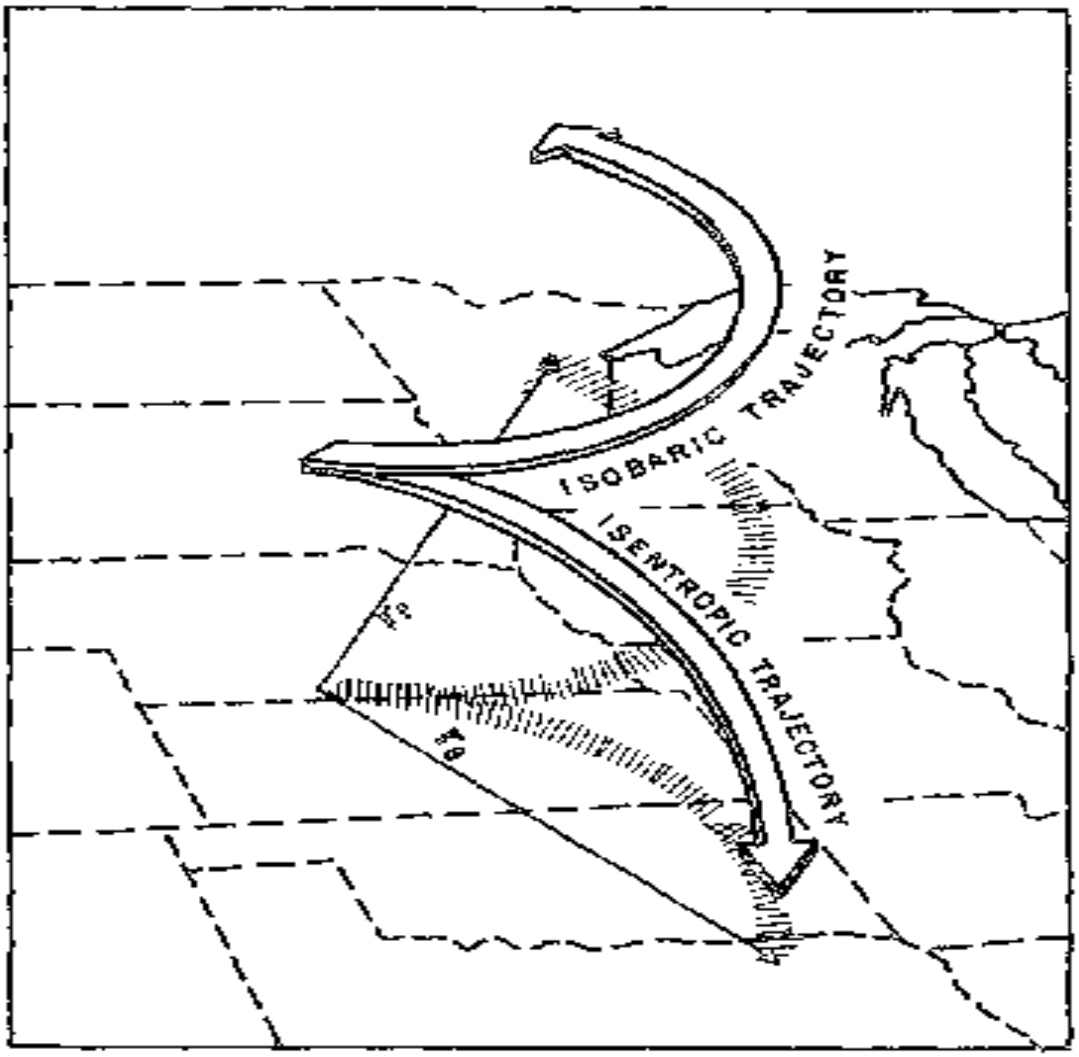

Figure 2.1: A comparison of twelve-hour isobaric and isentropic trajectories originating from 700 hPa at 0300 GCT 28 March 1956. Terminal pressure of the 290K isentropic trajectory is 880 hPa. Horizontal deviation is 1300 $\pm$ 200 km. Adapted from Danielsen 1961.

(1973) emphasized the utility of this parameter being exclusively linked to diagnostic studies rather than prognosis. The first team to fully exploit Ertel's (1942) theorem of PV was Eliassen and Kleinschmidt (1957), in which they speculated that during the cold season, the lower polar stratosphere acts as a reservoir for PV, yet the team was unable to decipher why it was along a polar front that created a cyclone. Bleck (1973) stressed that the stretching of vortex tubes is most intense whenever the air aloft experiences a depletion of isentropic surfaces beneath.

To ensure the numerical model in his study was as simple as possible, Bleck (1973) assumed a geostrophic wind field, and the actual prediction process is a repetition of the following two steps:

1) Local changes in Z (height) on theta surfaces are brought about by advecting the patterns over a suitable time interval.

2) The Ψ field is adjusted to the new Z, θ configuration by solving the PDE:

$$\Psi_{xx} + \Psi_{yy} + \left[-3.5f\left(\frac{\Psi_\theta}{c_p}\right)^{2.5}\left(\frac{Z}{c_p}\right)\right]\Psi_{\theta\theta} - \frac{\Psi_x f_x}{f} - \frac{\Psi_y f_y}{f} + f^2 = 0 \qquad (2.20)$$

where f is the Coriolis parameter. Since the above equation is slightly nonlinear in the θ direction, it was decided to solve the equation implicitly in the vertical and by employing successive over-relaxation in the horizontal. As long as the terrain is flat, integration of (2.20) will be stable. Smoothing techniques were employed by using 'potential virtual temperature' as coordinate surfaces and using Eddy's (1967) objective analysis scheme to infer grid point corrections.

The data grid was a 21x21 point subset with mesh size varying to less than 300km over the Gulf of Mexico to about 400 km near the pole. Nine theta surfaces were chosen, extending from 260K to 340K in 10K intervals, noting that the ground was allowed to go as low as 250K. The northern half of the grid space consists of the nine theta surfaces, whereas the southern half's resolution was reduced to five surfaces. Since tilting frontal zones occupy a horizontally oriented yet vertically inflated volume in isentropic space, the loss in grid resolution is insignificant to the study. The equations (only one of which is included here) were integrated to 36 hours in 30 minute time steps.

The conclusions drawn from the study included a satisfying synthesis between the development concepts of Sutcliffe (1947) and Petterssen (1956). Three explosive cyclogenesis cases

(one of which is reproduced via Figures 2.2 and 2.3) were examined as well as one non explosive case. High PV values in the upper air current drift over a southerly current near the ground, which plays a vital role in cyclogenesis. Retardation of the surface theta advection distinctly inhibited the growth of the cyclones. The reason for the lack in surface pressure response (as observed in the actual isentropic forecast: upper-left quadrant of Figure 2.3) may have been due in part by the cross-isobaric mass flow that occurs while the air seeks to retain geostrophic balance, a process that cannot occur in a geostrophic model. The exceptional over-prediction of the cyclone in the lower-left quadrant of Figure 2.3 was thought to be due to difficulties in transforming data from the National Meteorology Center (NMC) isobaric data to isentropic data, yet by implementing (2.20), the NMC geopotential and temperature data when converted to isentropic coordinates (Figure 2.3: upper-right quadrant) yielded a near similar result to the straight isentropic forecast (Figure 2.3: upper-left quadrant). Although the isentropic model over-predicted surface pressure changes, its ability to pinpoint the location of major baroclinic development invited a reevaluation of the advantages and drawbacks of not only geostrophic theory, but isentropic coordinates as a whole

. Although such detailed isentropic maps were not readily available to operational meteorologists in the 1970's, Uccellini (1976) generated simple isentropic charts from the standard surface, 850-, 700-, and 500-hPa levels (Figure 2.4). The purpose of the study was to diagnose synoptic and sub-synoptic scale flow patterns and to further illustrate the advantages of the isentropic framework, mostly in the field of moisture transport as seen by Danielsen (1961). The following are a series of features using isentropic coordinates outlined in this study:

-Two basic maps are used in isentropic analyses: one with contours of Ψ and the wind vectors, and the other with pressure fields.

-∇p is proportional to the strength of the thermal wind, Figure 2.5). Large ∇p indicates an area where the thermal wind is strong, indicating baroclinic or frontal zones.

-The analysis of the pressure difference between two isentropic surfaces details the static stability. Small Δp (tightly packed theta contours in the vertical) between two theta layers indicates near adiabatic conditions and relatively stable air.

-Horizontal and especially vertical moisture transport is more coherent in an isentropic framework than in pressure-space, as noted by Oliver and Oliver (1951).

-The pressure difference between two isentropic surfaces provides a measure of static stability. Where Δp is large, the layer is more adiabatic and thus less stable.

At the time of this study, vertical motion had to be inferred based upon temperature and vorticity advection. However, isentropic upward vertical motions (UVM's) can be solved directly via the equation:

$$\omega = \frac{dp}{dt} = \frac{\partial p}{\partial t} + \vec{V} \cdot \nabla_\theta P + \frac{d\theta}{dt}\frac{\partial p}{\partial \theta} \tag{2.21}$$

where the local pressure change, horizontal pressure transport, and diabatic heating are the first, second, and third terms on the RHS, respectively. The only difficult quantity to measure is $d\theta/dt$ due to uncertainty and the fact there was no direct means of measuring all diabatic processes. Upon constructing isentropic charts from standard pressure maps, Poisson's equation is implemented in which an isotherm on a pressure surface is an isobar on an isentropic surface. From there:

1) Isolate an area of interest on the 850-hPa surface corresponding to a unique theta surface, θ_k, where an isotherm extends through a LLJ core and through as many surface stations as possible.

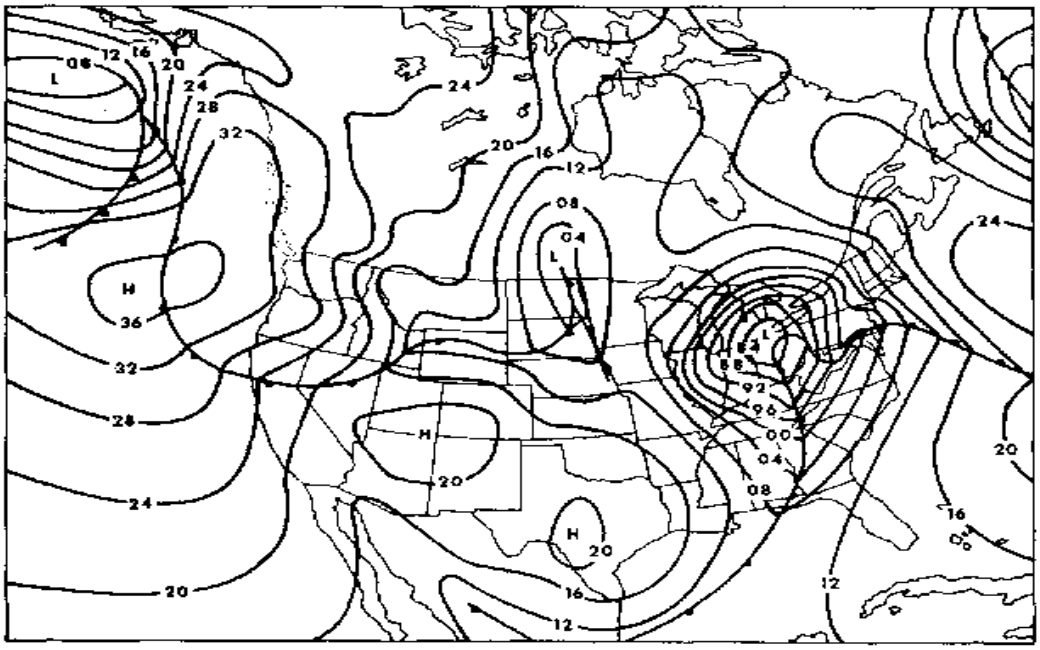

Figure 2.2: Observed surface pressure at 1200 GMT 2 April 1970: 100- and 1000- mb digits are omitted in isobar labelling. Reproduced from Bleck 1973.

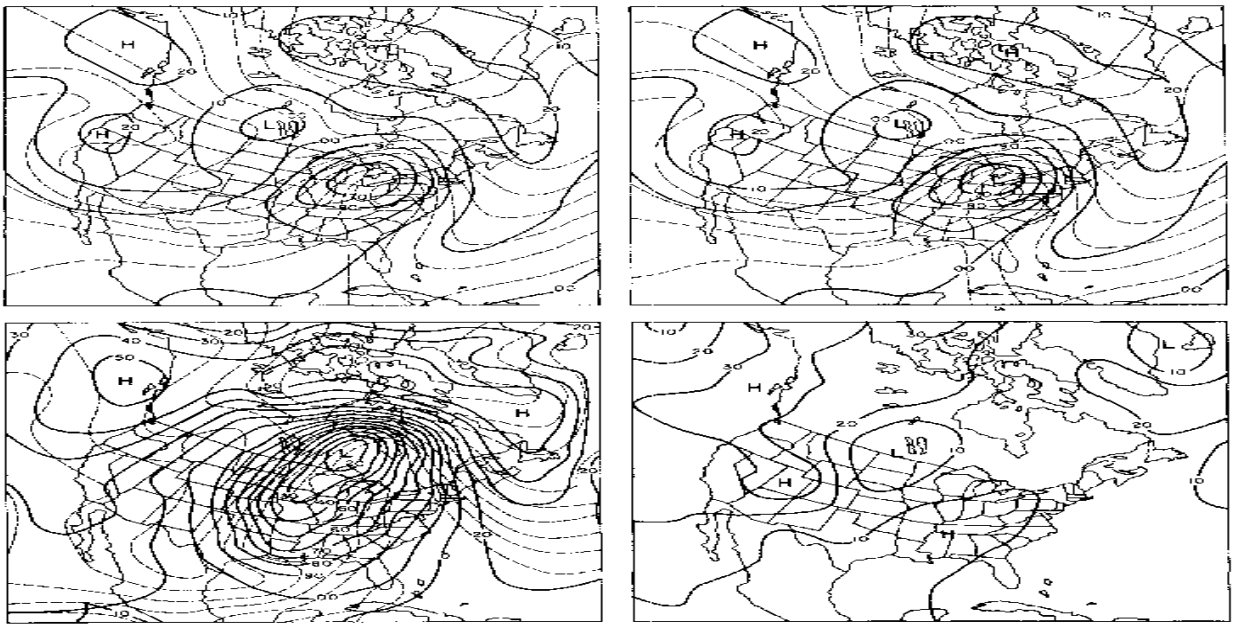

Figure 2.3: Surface pressure conditions (36 hr) for 1200 GMT 2 April 1970. Upper left: isentropic forecast from data analyzed in isentropic coordinates; upper right: isentropic forecast from isentropic data transformed back and forth between θ and p coordinates; lower left: isentropic forecast based on National Meteorology Center (NMC) analyzed geopotential and temperature fields; lower right: NMC forecast. Isolines of potential temperature (dashed) are drawn in 5K intervals; 100- and 1000-hPa digits are omitted in isobar labelling. Reproduced from Bleck 1973.

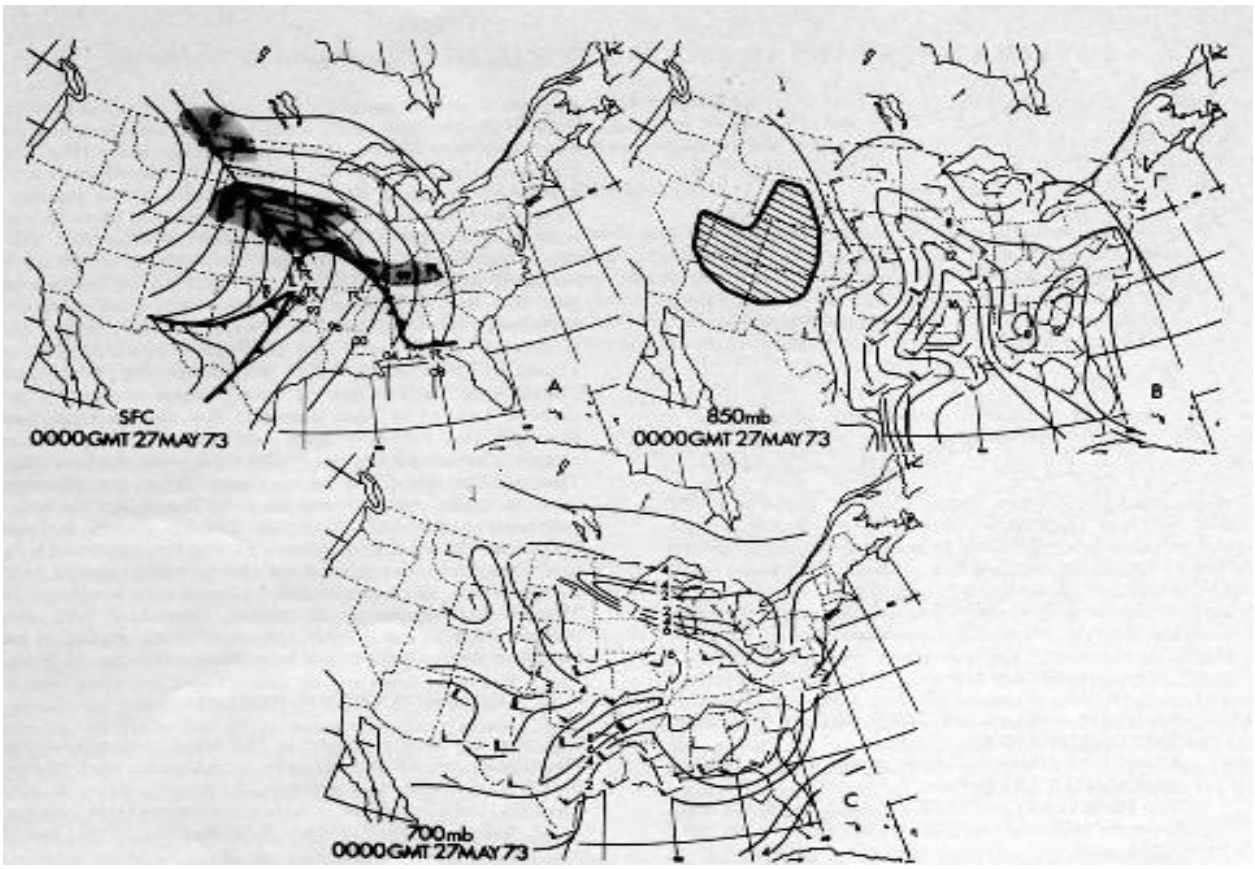

Figure 2.4: A: surface pressure and precipitation analysis; B: 850-hPa mixing ratio (g/kg) analysis; C: 7000hPa mixing ratio (g/kg) analysis for 0000 GMT 27 May 1973. Reproduced from Uccellini 1976.

---

2) Next, temperature, mixing ratio, and wind information are transferred from the 850-hPa, 700-hPa and 500-hPa levels onto the θ_k map. Three pressure levels are then planned onto one map.

However, during the summer months and especially within a barotropic domain, the vertical distance between the 850-hPa and 700-hPa could extend over 1000km, yielding little information. This technique is specialized for baroclinic regions related to cyclogenesis, frontal bands, and the jet stream (or other areas where large values of UVM exist). Four case studies (one of which is provided via Figure 2.6) were utilized with a summary as follows: using the isentropic map construction described above, moisture transport was more coherent, UVM was easy to compute,

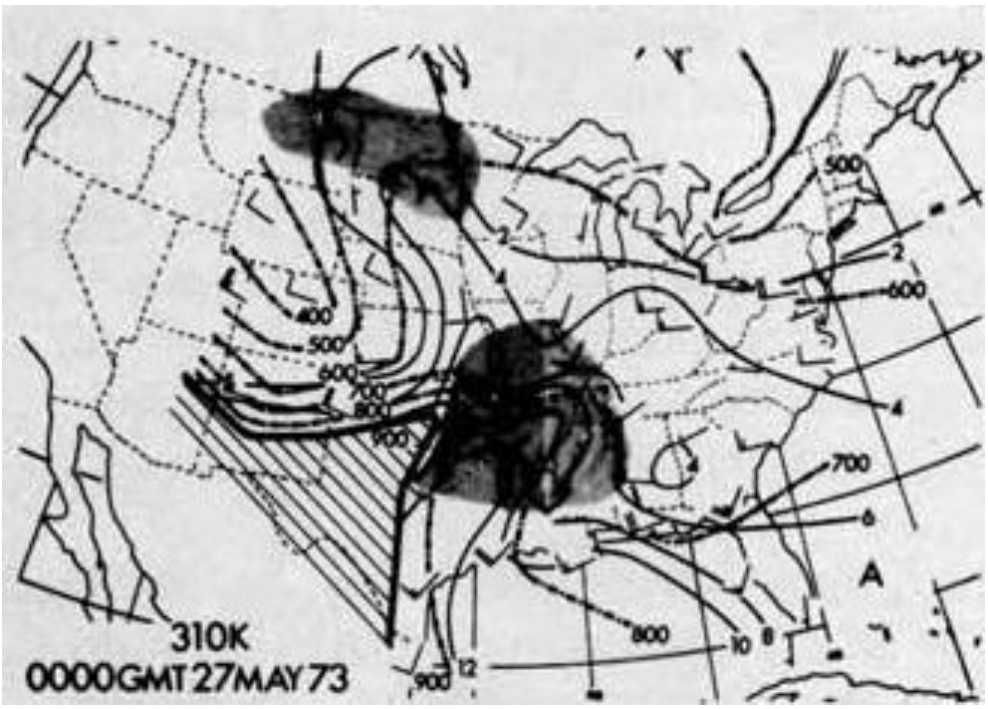

Figure 2.5: 310K isentropic surface analysis for 0000 GMT 27 May 1973 with pressure in hPa (dot dashed line) and mixing ratio (thin solid). Hatched area indicates isentropic levels beneath the surface. Wind barbs in ms^{-1}. Shaded area depicts region of upward motion as estimated from the advective term (term 2 on RHS of 2.21). Reproduced from Uccellini 1976.

and physical insight into the juxtaposition of UVM, moisture transport, and the upper tropospheric jet stream was revealed. The latter physical insight can be extended to relate the concept of vertical jet coupling (LLJ correspondence to ULJ).

Following Uccellini's synoptic-scale work, mesoscale forecasting became the new frontier when Keyser and Johnson (1984) developed a paper looking at isentropic coordinates to distinguish the process responsible for mass circulations in an upper level jet streak to that of an MCC. It had been previously seen from Ninomiya (1971) that the release of latent heat in convective systems was the primary factor in intensifying the upper-level synoptic scale flow through strengthening the horizontal temperature gradient. In an Eulerian view, the upper tropospheric jet streak entrance promoted subgeostrophic parcels to accelerate into a region of maximum winds through

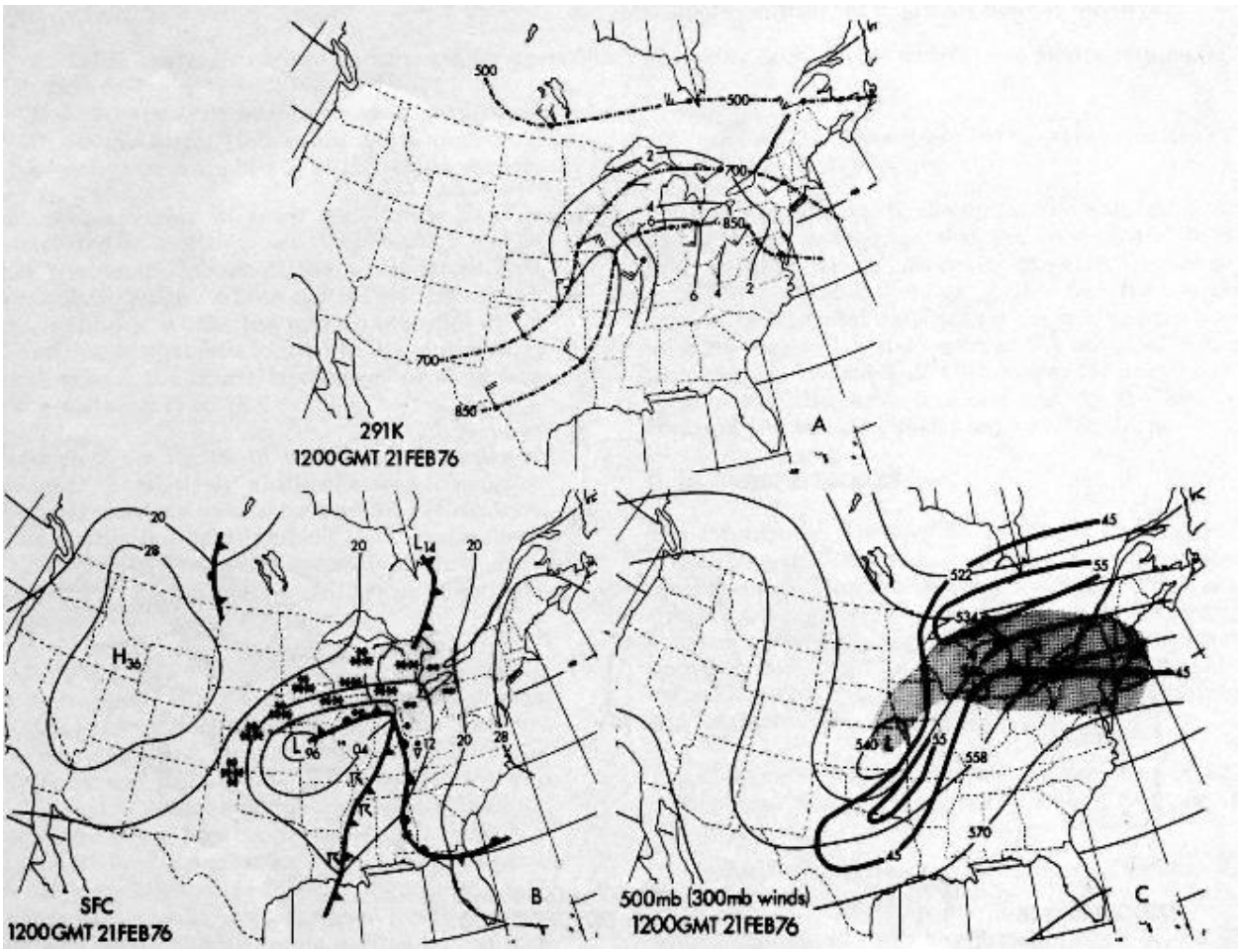

Figure 2.6: 291K isentropic analysis (upper-centered)with isobars (dot dashed), mixing ratio (g/kg, thin solid) and wind barbs in ms^{-1}; surface (lower-left quadrant) analysis with pressure in hPa, and 500-hPa height (thin solid in dkm) and 300-hPa isotachs (in ms^{-1}, lower-right quadrant) analysis for 1200 GMT 21 Feb 1976. Reproduced from Uccellini 1976.

ageostrophic motion directed towards lower pressure. After passing through this region of maximum winds, the parcel experiences supergeostrophic conditions and slows down in the exit toward higher pressure. As a result, vertical branches of ascending motion occur in the left exit and right entrance, while descending motion occurs in the other two branches. Because of this phenomenon, secondary mass circulations induce temperature changes along with frontogenetic and frontolytic fields. In the exit region, the mass adjustment leads to intensification of the baroclinicity which provides thermal support for the approaching jet streak. In the entrance region, baroclinicity

is relaxed as the jet streak propagates downstream. In a Lagrangian framework, an air parcel is frontogenetic in the entrance region since it is moved from a region of reduced to increased baroclinicity. The opposite is true in the exit region. The examination of mass circulation begins with the isentropic mass continuity equation:

$$\frac{\partial}{\partial t}(\rho J) + \nabla_\theta \cdot (\rho J U) + \frac{\partial}{\partial \theta}\left(\rho J \frac{d\theta}{dt}\right) = 0 \tag{2.22}$$

where ϱ is density and *J* is the Jacobian of transformation $\partial z/\partial \theta$. Through manipulation of the ageostrophic isallobaric motion, surface pressure tendency is defined in such a way that diabatic heating only results in the vertical redistribution of mass within an atmospheric column. Such a process does not alter the surface pressure tendency since it is determined by the net horizontal mass flux divergence throughout the entire vertical extent of the atmosphere. Also, it is important to note the inertial diabatic wind component will increase with height through convective latent heat release, which in deep convection must reach a maximum near the tropopause. The study consisted of NASA's fourth Atmospheric Variability Experiment (AVE IV) due to its high 3- and 6- hour temporal resolution, which should improve the accuracy of the analyses of mesoscale processes. Breaking the ageostrophic and geostrophic wind into its components, Keyser and Johnson (1984) were able to assess which components were influential. Through the use of isentropic coordinates, the effects of diabatic heating/cooling are better seen than on the traditional isobaric surfaces. This is because parcels will 'jump' from one theta surface to the next under copious latent heat release, and the diabatic term, $d\theta/dt$, is directly calculable in (2.21).

Maps of the total, inertial advective, isallobaric, and inertial diabatic ageostrophic wind vectors were plotted on isentropic surfaces between 310-330K. Upon integration of (2.22) will yield the mass flux divergence (Figure 2.7) of an isentropic layer. Within the right entrance region of the

upper-level jet streak yielded strong values of the vertical mass flux divergence, and a time-averaged vertical profile of the diabatic heating within the boxed area in Figure 2.7 is displayed via Figure 2.8. The heating rate (positive diabatic heating) correlates well to large values of mass-flux divergence produced by the MCC. It was noted that the direction of the ageostrophic motion agrees with the direction expected in the confluent flow field of the jet's entrance region; ageostrophic motion points in the direction of the PGF.

The inertial advective motion is an important component of the total ageostrophic wind field in the entrance region, whereas the isallobaric component was primarily responsible for driving the overall mesoscale mass circulation of the MCC (Figures 2.9 and 2.10). The diabatic forcing of inertial ageostrophic motion within the MCC at upper levels acts to intensify the thermally direct mass circulation in the entrance region of a jet streak. With strong vertical wind shears, diabatic vertical mass flux transports momentum upwards to levels of stronger geostrophic momentum. Thus, the momentum of the upward diabatic mass circulation is subgeostrophic and is accelerated to the left.

The adiabatic component, with convergence into the MCC at upper levels, is countered by the diabatic component which diverges away from the convective region. In the upper levels, the diabatic component transports mass across the entrance region from the anticyclonic to cyclonic side of the jet, while the adiabatic isallobaric wind component transports mass in the opposite direction. This dichotomy is maximized in the upper levels since the strength of the diabatic isallobaric motion is inversely proportional to pressure and increases with height where there exists heating in the vertical.

The warming of the troposphere in the region of convection increases the thermal wind to the left of the current and decreases the thermal wind to the right. The changing surface pressure

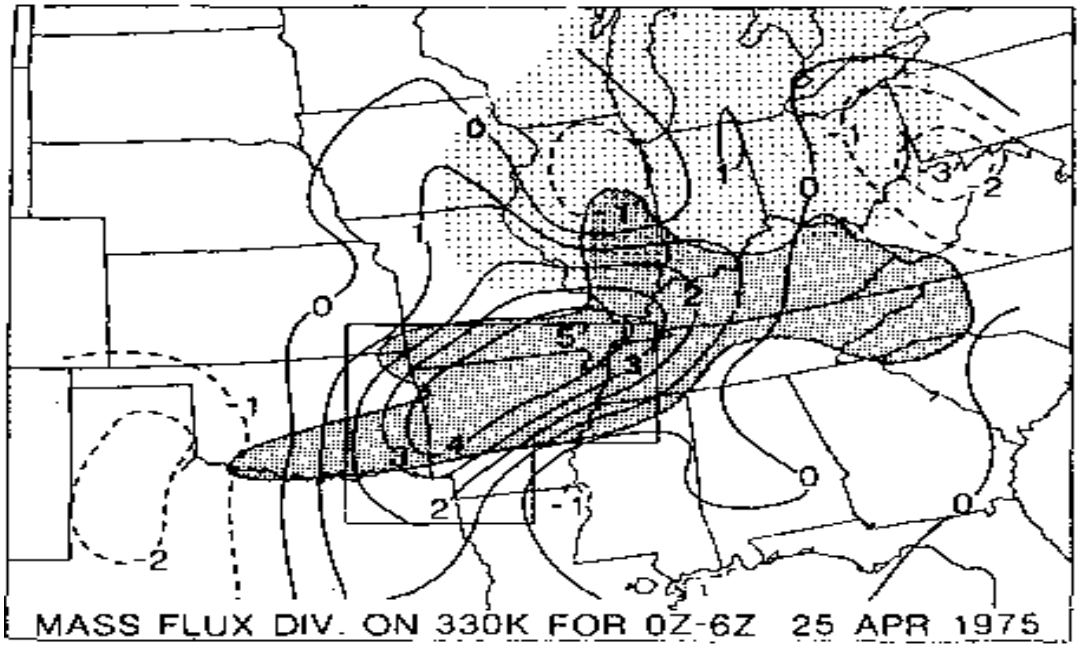

Figure 2.7: Time-averaged horizontal mass flux divergence for 330K isentropic surface (positive, solid; negative, dashed; $x10^1$ g m^{-2} s^{-1}) computed for 0000-6000 GMT 25 Apr 1975. The eighteen grid points used in areal averaging for Figure 8 are enclosed within the light outlined box. Heavily stippled region indicated the MCC under study and observed wind speeds greater than 40 ms^{-1} are lightly stippled. Reproduced from Keyser and Johnson 1984.

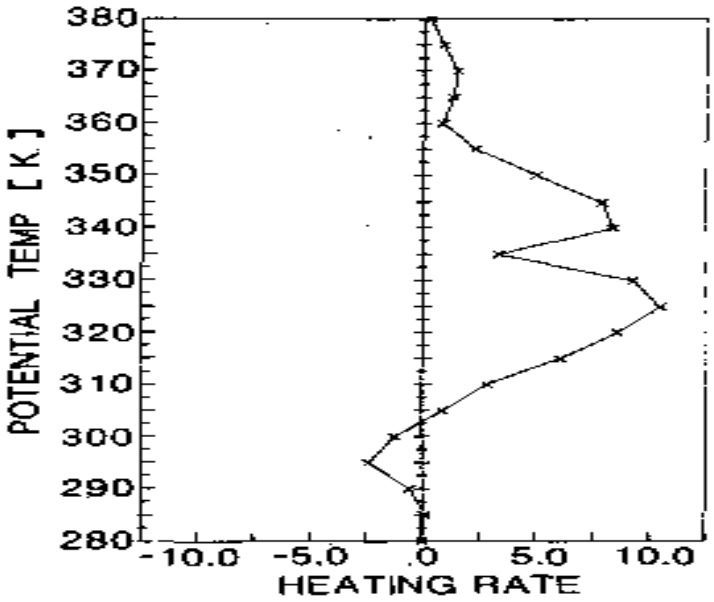

Figure 2.8: Vertical profile of areally averaged diabatic heating rate [K $(6\ hr)^{-1}$] through MCC as seen in Figure 2.7. Reproduced from Keyser and Johnson 1984.

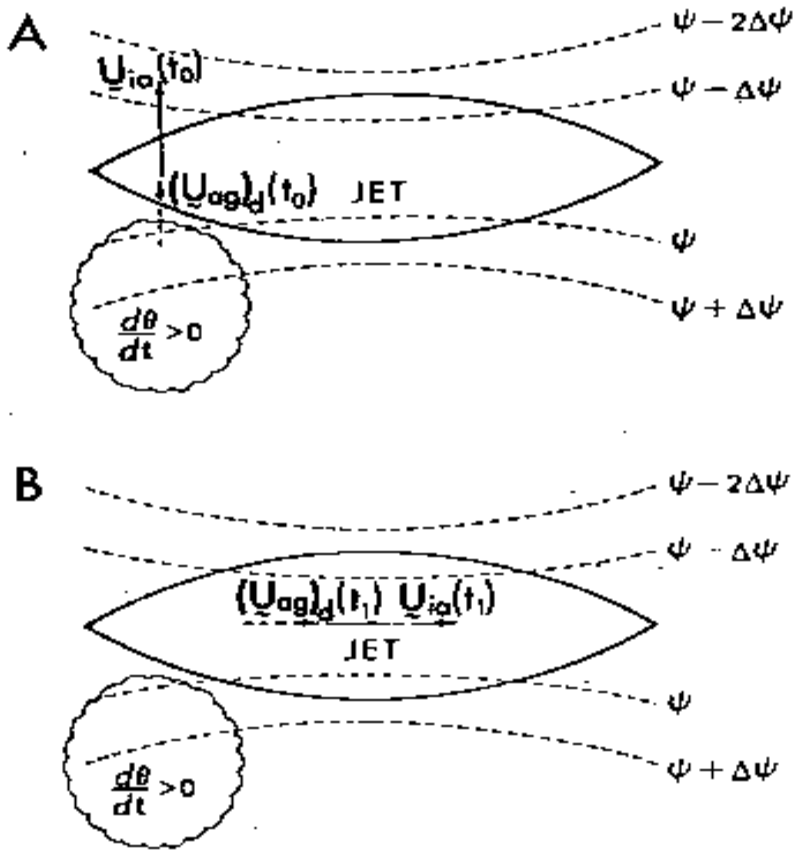

Figure 2.9: A: Schematic showing diabatically induced ageostrophic motion $(\mathbf{U}_{ag})_d$ directed in the same sense as the upper tropospheric inertial advective wing $(\mathbf{U}_{ia})$ associated with the horizontal branch of the direct circulation of the jet streak at time t_0; B: Schematic of jet streak with increased velocity due to inertial rotation of ageostrophic momentum after Lagrangian displacement downstream after time $t_1 - t_0$. Reproduced from Keyser and Johnson 1984.

field due to quasi-horizontal redistribution of mass results in an isallobaric wind at low levels converging into the MCC (Figure 2.10). This mesoscale phenomenon acts to intensify the thermally direct mass circulation in the entrance region of the jet with inertial adiabatic geostrophic motion and generates kinetic energy which accumulates downstream in the jet.

Through the increasing development of computers with higher spatial and temporal resolution, Petersen and Homan (1988) developed one of the exceptionally few nowcasting isentropic models to date. The authors introduce their paper by analyzing the improvement of the horizontal and vertical structure of small-scale meteorological phenomena beyond a 24-hour period.

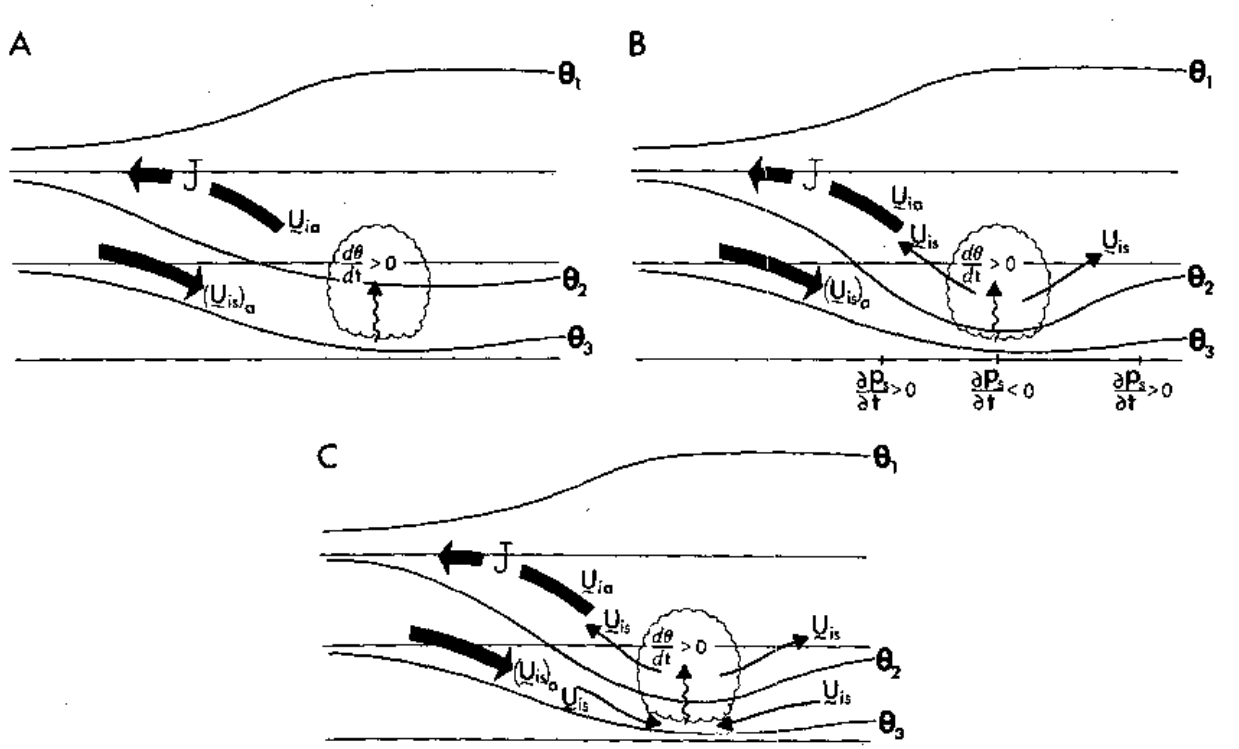

Figure 2.10: Vertical cross-section schematic normal to jet streak J showing: A: location of developing MCC in relation to the direct circulation in the entrance region; B: upper-level isallobaric wind ($\mathbf{U}_{is}$) forced by differential diabatic heating in mature MCC with resulting surface pressure tendencies ($\partial P_s/\partial t$) and C: resultant low-level isallobaric wind convergence into the MCC. Reproduced from Keyser and Johnson 1984.

Although the models were becoming increasingly complex in this time period with an increase in forecast skill, the models were still hampered by three main issues:

1) Deficiencies in the very short-term guidance when dynamical balances are forming within numerical simulations

2) Inability to access the gridded model output for more detailed diagnosis or to view the evolving forecast at frequent enough time intervals

3) Inability to enhance particular aspects of the initial analyses using additional data of local importance.

Therefore, accurate forecasts of small-scaled features and parameters were still limited to 24 hours or less. The purpose of Petersen and Homan (1988) study was to describe a numerical advection model (Figure 2.11) that could be run on a local computer in a real-time forecast environment. Also, they intended to present a series of applications of the model in predicting the preconvective environment in both spring and summertime. Isentropic coordinates were chosen due to the increased spatial and temporal ease of use in estimates of temperature, moisture, and wind changes between 12-hour rawinsonde observations.

The model used in the study generated short-range (2-12 hour) forecasts by implementing a three-dimensional, adiabatic isentropic model. All analyses were obtained using the high-resolution isentropic procedure described by Petersen (1986). Similar to the experiments in Bleck (1973), the model uses PV conservation and mass continuity as a basis for validity of the predictions. The model's PV prediction equation was combined from the PV equation, isentropic mass continuity equation, and implementation of the geostrophic vorticity approximation to yield:

$$\frac{\partial}{\partial t}\left(\zeta_{\theta_g}+f\right)=\frac{\partial p}{\partial \theta}\{-\left(\zeta_{\theta_g}+f\right)\left[\frac{\partial}{\partial t}\left(\frac{\partial \theta}{\partial p}\right)\right\}+\frac{\partial p}{\partial \theta}\{-V\cdot\nabla\left[\frac{\partial \theta}{\partial p}\left(\zeta_{\theta_g}+f\right)\right]\} \tag{2.23}$$

where ζ_{θ_g} is the geostrophic potential vorticity (GPV), and $\left(\zeta_{\theta_g}+f\right)$ is the absolute geostrophic vorticity (AGV). The forecast equation states that changes in AGV are related both to the advection of GPV and static stability. Within the model, GPV conservation is applied only at the 'foundation layer' which is positioned either near the level of maximum diabatic heating or where diabatic heating processes are assumed to be small. Isentropic mass continuity is applied to every level of the model. Wind computations were used in conjunction with the geostrophic approximation and Ψ, which is computed as:

$$\frac{\Delta\Psi}{\Delta\theta}=c_p\left(\frac{\bar{p}}{1000}\right)^k \tag{2.24}$$

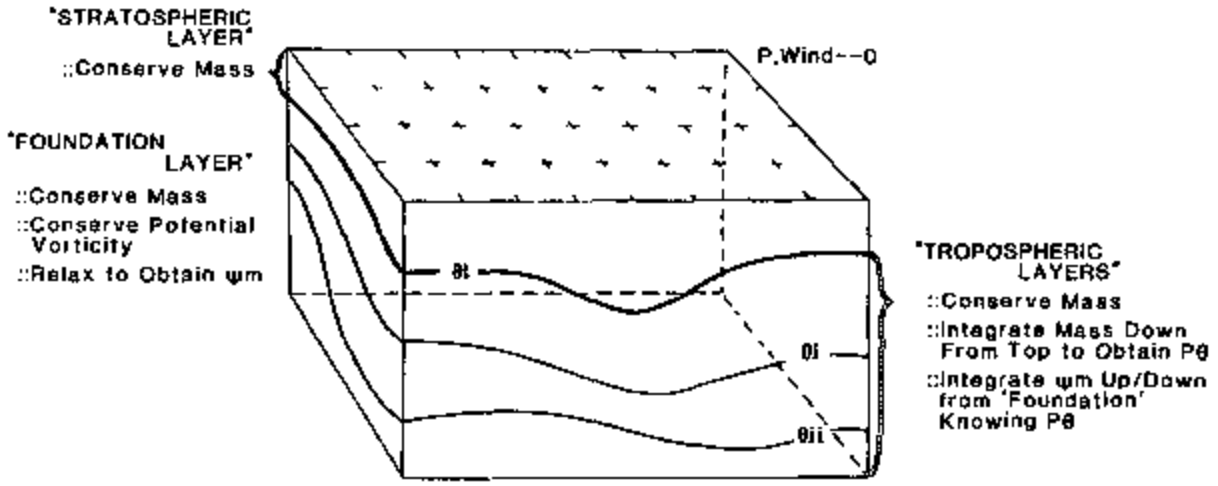

Figure 2.11: Overview of the advective model structure used. Reproduced from Petersen and Homan 1988.

---

in which $k = {R_d}/{C_p}$ where R_d is the dry gas constant, and $\bar{p}$ is the average pressure in the integration layer. Therefore, fields of Ψ are used to compute geostrophic wind components.

Applications of the isentropic short-range advection forecasts were studied in three separate categories:

1) Forecasts of midtropospheric stability patterns. The study for this example covered a 6-hr initial forecast before a severe weather outbreak in the Ohio River Valley on 23 April 1968. It is noted that changes in mass in an isentropic layer should be interpreted as inverse changes in static stability, i.e. an increase in mass between two theta surfaces is correlated to a decrease in static stability, promoting convective growth. Midtropospheric isentropic mass values greater than 230 hPa/ 10 K represent conditionally unstable lapse rates. It was observed that in precipitation-free regions, forecasted stability agreed remarkably well with the observed values. While the adiabatically forecasted stability values did not verify where precipitation occurred, the presence of precipitation

is consistent with the midtropospheric destabilization predicted in those areas. The environment downstream of a midtropospheric jet streak became conditionally unstable due to, in part, by isentropic mass convergence, supporting deep convection. Isentropic mass divergence was seen upstream of the jet.

2) The three-dimensional mass and moisture forecasts are used to isolate small areas of stability change. This example illustrates for the addition of multiple layers to include changes in low-level moisture, stability parameters, tropopause height, and buoyant energy. It was noted the model used captured differential advections normally associated with convective outbreaks. The inclusion of significant-level data and high-resolution analyses was especially important since the available moisture supply was confined below 850 hPa and undetected using many conventional stability indices.

3) Forecasted winds are used to advect low and midlevel VAS (visible and infrared spin-scan radiometer atmospheric sounder) derived moisture fields. Using high-frequency wind fields obtained from the theta-prediction scheme, VAS high-resolution water vapor images were advected for periods up to 12 hours. Although the results obtained did not explicitly capture the most extreme changes, the quality of the forecast and the accuracy of the derived convective instability fields in capturing mesoscale areas of potential convective outbreaks thrived. These two important observations, along with the overall simplicity of the scheme and project, point to potential for the model to facilitate short-term forecasts and nowcasts.

With the ever-increasing resolution of atmospheric models, smaller-scaled processes will imminently be exposed. However, since most of meteorology, especially within the mid-latitudes, is predicated on quasi-geostrophic (QG) theory, larger grid-spacing models is more idealized. This is especially true of model depictions of synoptic-scale vertical motions (where the synoptic scale is

defined as processes where the Rossby number is between 0.1 and 1.0, and the mesoscale refers to processes which lie between 1 and N/f, where N is the buoyancy frequency and f is the Coriolis parameter). Barnes et al. (1996) describes a method for extracting synoptic-scale information from mesoscale model data, and determining the filtering and smoothing requirements necessary to resolve synoptic-scale patterns of vertical motions using QG diagnostics. A 29-km grid using a 50-layer Eta model was used for the study, where the physics of such a model can be summarized via the following:

1) The model is hydrostatic and implements the Eta vertical coordinate which reduces error in the PGF term in the momentum equations.

2) Convective parameterization based upon the Betts (1986) convective adjustment scheme.

3) NCEP's version of the radiation scheme developed at the Geophysical Fluid Dynamics Laboratory (Lacis and Hansen 1974; Fels and Schwarztkopf 1975); and

4) Boundary-layer processes expressed as the Mellor-Yamada (1974) turbulent kinetic energy formulation.

Forward-backward time differencing was used for the adjustment stage (e.g., Coriolis terms), a modified Euler backward time differencing was used for the advection terms, and for model stability, an implicit backward time scheme was implemented.

The study assumed that QG-forced vertical motions can be depicted by the Hoskins et al. (1978) divergence of Q (the Q vector) by:

$$\sigma\nabla^2\omega + {f_0}^2\left(\frac{\partial^2\omega}{\partial p^2}\right) = -2\nabla \cdot Q \qquad (2.25)$$

whereσ is the static stability and f_0 is the constant Coriolis parameter. If it is assumed that horizontal variations in ω dominate over vertical variations, and the horizontal distribution of ω has harmonic structure, then (2.25) becomes:

$$\nabla \cdot Q \propto \omega \tag{2.26}$$

An important implication of this study found that if filtering data properly with a small enough mesh size, truncation errors in derivatives (especially second-ordered derivatives) are negligible, then maxima in the derivatives that determine Q should be independent of the relatively short distances. It follows that maximum $\nabla \cdot Q$ is scale dependent the same way the divergence of the wind is scale dependent. With Q being independent of scale, proportionately larger $\nabla \cdot Q$ maxima can be computed when finite differencing is invoked on a smaller grid-scale compared to a larger grid-scale (i.e. mesoscale models should produce larger values in $\nabla \cdot Q$ compared to synoptic-scale models).

Through the case study of a large gravity wave train extending over the contiguous U.S. resulting from a strengthening jet over the Pacific Northwest, a numerical filter was designed such that the gravity waves are effectively removed, yet the amplitudes of the baroclinic waves were not significantly diminished. QG diagnostics computed from the filtered data produced magnitudes of $\nabla \cdot Q$ normally associated with baroclinic waves, and the $\nabla \cdot Q$ centers were found in the expected synoptic-scale troughs produced by the amplifying jet.

Although QG theory tends to be limited to the synoptic-scale, many authors still implement its theory. Moore et al. (1998) looked at heavy precipitation associated with elevated synoptic-scale thunderstorms in an isentropic framework. Previous work by Colman (1990) had analyzed that there are two main criteria for determining the existence of an elevated thunderstorm source, of which the analysis is taken on the cold side of the front. First, nearby station's temperature,

dewpoint, and wind must be qualitatively similar to surrounding area's values. Second, the surface air on the warm side must have a higher θ_e than the cooler side. These zones generally exist in regions of strong baroclinicity, vertical wind shear, and low level warm air advection (LLWAA). Elevated thunderstorms are also generally climatologically favored in the transition seasons (spring and fall). The main focus of Moore et al. (1998) was to analyze the synoptic environment favorable to the development of these elevated thunderstorms using an isentropic perspective for a heavy rain and heavy snow event.

The heavy snow event was analyzed by taking a cross-section from International Fall, MN (INL) to Longview, TX (GGG). Analysis of a sounding from North Omaha, NE (OVN) with a separate plot of vertical θ_e showed that the atmosphere was indeed convectively unstable in the middle troposphere. Also, a diagnosis of equivalent potential vorticity (EPV) was used. The logic follows from previous studies by Bennetts and Hoskins (1979) and Moore and Lambert (1993): if EPV is negative in a convectively stable atmosphere ($\partial\theta_e/\partial z > 0$), then that area is characterized as having conditional symmetric instability (CSI). From this method, it was shown that the atmosphere was supportive of CSI.

The heavy rain event was analyzed in April 1994 with multiple parameters not commonly seen in papers. First, a plot of the vertical difference of θ_e between 500 hPa and 850 hPa was computed, with negative values indicating a convectively unstable environment. This method made it evident (along tight gradients) where isentropic upglide was occurring. Also, moisture transport vectors (MTV's), defined as the product of the vector wind (V) and the specific humidity (q), were plotted. MTV's revealed areas within the domain of the study that received a net increase or

decrease of moisture. The moisture stability flux (MSF) was used to diagnose not only the advection and convergence of moisture, but also the static stability. The formal definition takes the form:

$$\text{MSF} = -\nabla \cdot (q\Delta pV) = -V \cdot \nabla(q\Delta p) - (q\Delta p)\nabla \cdot V \tag{2.27}$$

Positive values of MSF are indicative of moisture convergence and destabilization of the atmospheric layer. Finally, a vertical cross-section of the ageostrophic secondary circulation was constructed such that the horizontal length of each vector was proportional to the tangential ageostrophic wind component while the vertical component of each vector is proportional to the vertical motion. This plot made it clear where upward vertical motions existed and where a direct thermal circulation existed.

Moore et al. (1998) concluded that θ_e was the most useful quantity in identifying convective activity due to its aid in identifying frontal slope and position, layers of convective instability, and the most unstable parcel in a sounding. Analysis of CSI is important to determine if areas of elevated convection could be triggered and/or released.

Stemming off the concept of elevated thunderstorm analysis, Rochette et al. (1999) diagnosed the difference in using CAPE versus MUCAPE (most unstable CAPE, generally within the lowest 300 hPa). MUCAPE chooses the most unstable parcel (highest θ_e value in a sounding) when calculating CAPE. Using this most unstable method, values of MUCAPE were generally much larger than CAPE in regions of elevated thunderstorms, since convection was not rooted in the atmospheric boundary layer. The large-scale lift associated with the approach of a short-wave trough and a strengthening LLJ are fundamental in lifting a convectively unstable parcel to saturation. Mesoscale lifting at or near the frontal zone due to localized moisture convergence could lift parcels to their LFC. This could then initiate strong convection over a relatively limited area.

These regions are generally expected in the exit region of a LLJ where moisture convergence is maximized. Since elevated thunderstorms require the release of convective instability via lifting at or above a frontal zone, isentropic surfaces was chosen as the best method of analysis.

Two case studies were chosen to illustrate the difference in MUCAPE and CAPE (one of which is displayed via Figures 2.12 and 2.13). For the first case, an MCS was analyzed for 6 June 1993 over mid-Western Missouri. Upon retrieving soundings from Monett, MO and Topeka, KS, CAPE and MUCAPE could be calculated. It should be noted at the time of the soundings, Monett was representative of the inflow of the MCS whereas Topeka approximated the ambient environment in the cool sector. Upon calculating MUCAPE, an 88% increase in value was found for the Monett sounding and over 300% increase for the Topeka sounding compared to normal CAPE. The second case study involved another MCS but for 27 April 1997. The same approach was taken with a sounding in Monett, MO but also included Norman, OK for this study. Lifting a mean parcel in either sounding resulted in 0 $J\ kg^{-1}$ CAPE, while the MUCAPE values were 1793 $J\ kg^{-1}$(Monett) and 2479 $J\ kg^{-1}$(Norman).

For each study, a plan-view map was constructed comparing values of CAPE and MUCAPE. In general, MUCAPE contours were more widespread, and contained a maximum roughly 1000 J Kg^{-1} higher, usually near the initiation of the storms (Figures 2.12 and 2.13). Values of CIN and MUCIN were also computed, resulting in more accurate depictions of capping inversions. The authors assert that the ideal situation would be to examine CAPE and CIN fields in plan-view and vertical profiles of θ_e to determine the convective potential for a given region. A thorough analysis of the comparison between MUCAPE and CAPE will diagnose regions of elevated convection, which is related to copious rainfall and sometimes severe weather.

From work as early as Saucier (1955), and including authors such as Uccellini (1976) and

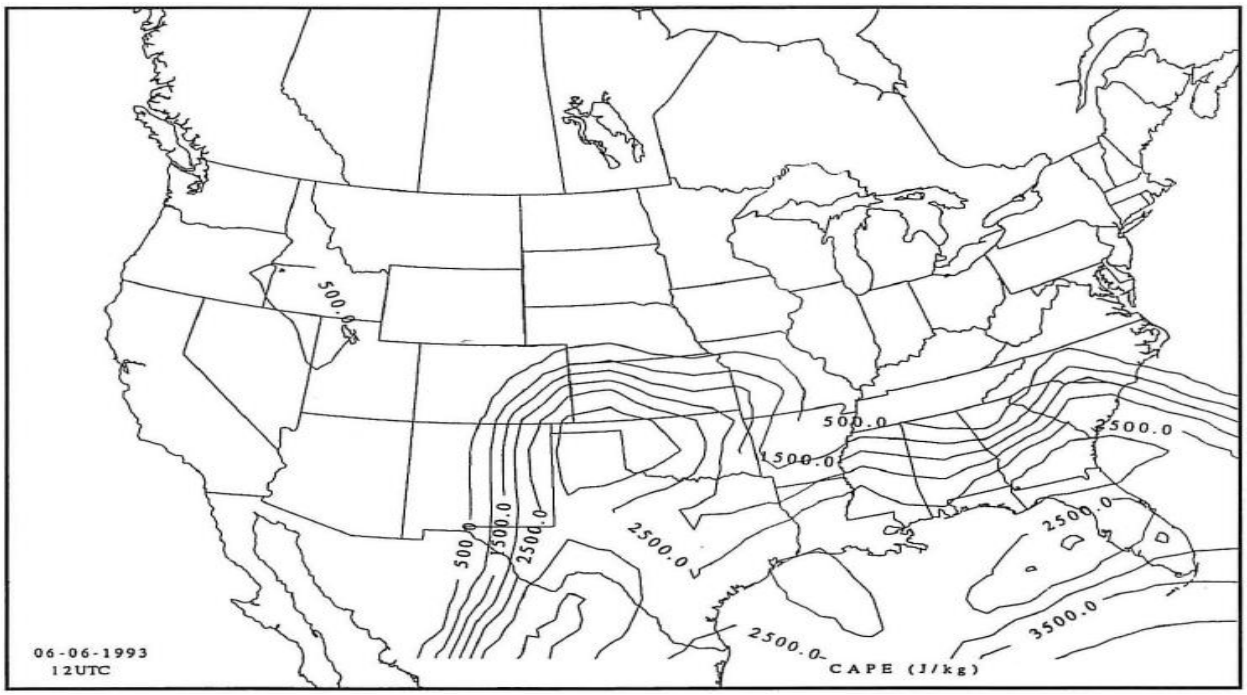

Figure 2.12: 1200 UTC 6 June 1993 objective analysis of mean-parcel CAPE ($J\ kg^{-1}$). Reproduced from Rochette et al. 1999.

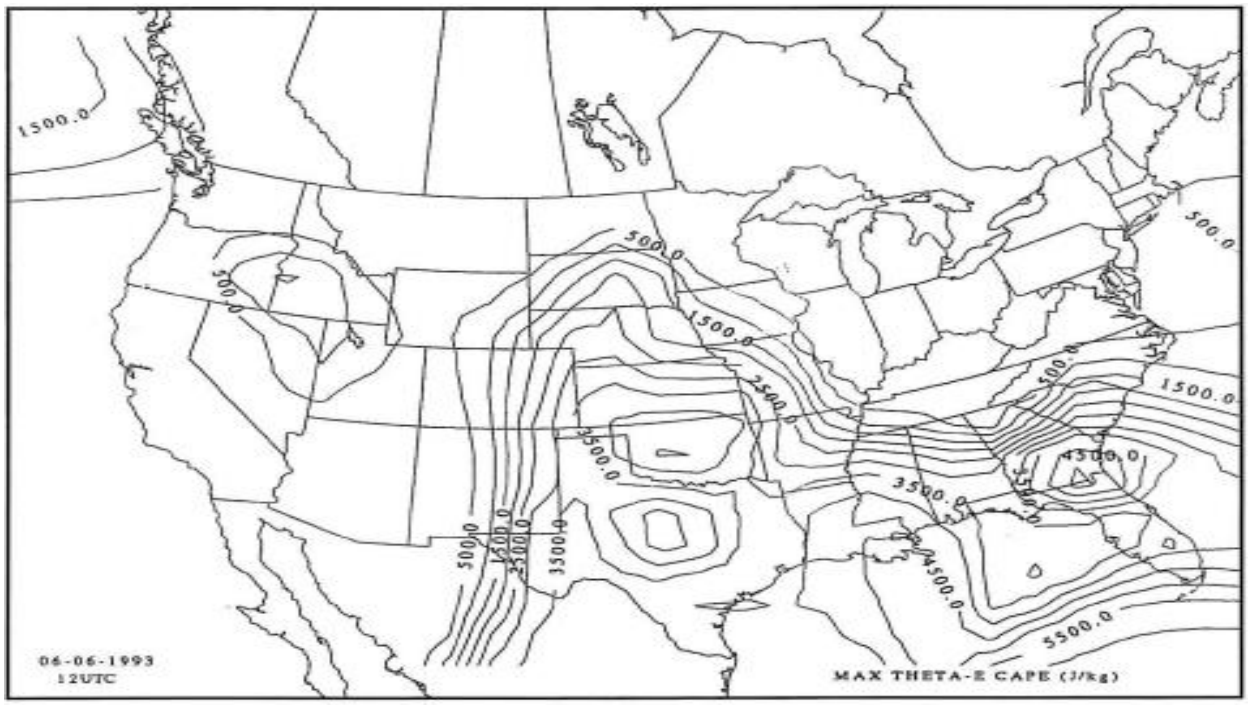

Figure 2.13: Same as Figure 2.12, except for MUCAPE ($J\ kg^{-1}$). Rproduced from Rochette et al. 1999.

Moore (1993), it has been a common practice to assume the diabatic and local pressure tendency term of the isentropic omega equation (ω_θ) would cancel each other. Therefore, the pressure transport term would be the dominant of the three terms and could accurately be calculated for a full ω_θ value, especially in regions where wind velocity was strong and directed parallel to the pressure gradient. However, work done by Market et al. (2000) examined the scope of the magnitude of each term in ω_θ through a variety of meso-α scale settings. Through calculating the first term by a 2-hour time difference centered on the time of interest and calculating the second term by a second-order centered finite difference approach, numerical values were rather easily obtained. To achieve an appreciable value for the diabatic term, the authors vertically integrated the isentropic continuity equation and through algebraic manipulation achieved:

$$\frac{\partial p}{\partial \theta}\left(\frac{d\theta}{dt}\right) = \int_{\theta}^{\theta_T} \nabla \cdot \left(\frac{\partial p}{\partial \theta}\vec{V}\right) d\theta + \left(\frac{\partial p}{\partial t}_{\theta_T} - \frac{\partial p}{\partial t}_{\theta}\right) \tag{2.28}$$

The model used in the study consisted of the Mesoscale Atmospheric Simulation System (MASS) version 5.10.1 (MESO 1993), including parameterizing the PBL and a modified Fritsch-Chappell (1980) cumulus parameterization scheme. The MASS output was then achieved using GEMPAK where low isentropic levels with RH values $\geq$ 99% and beneath which the model had generated precipitation of $\geq$0.5mm during the preceding hour of interest. Calculations of $\vec{C}$, the circulation vector, was subjectively estimated from the vorticity maximum motion on the isentropic surface of interest. Two of the case studies were taken from April 1999, one from April 1997, and one from January 1993 (Table 2.1). Their statistical analysis showed that the total mean ω_θ was of the same sign, but larger in magnitude by roughly a factor of two than the transport term alone. Neglecting only the diabatic term resulted in nearly two-thirds of the total ω_θ. Also, the storm-relative version proposed by Saucier (1955) resolved nearly three-fourths of the total ω_θ in three of

	N	$\bar{x}$	σ
$\left(\frac{\partial p}{\partial t}\right)_\theta$	80	-1.95	±1.87
$\vec{V}\bullet\nabla_\theta p$	80	-2.45	±2.50
$\frac{\partial p}{\partial \theta}\frac{d\theta}{dt}$	80	-2.76	±2.91
ω_θ		-7.16	
$(\vec{V}-\vec{C})\bullet\nabla_\theta p$	80	-3.70	±2.10

	N	$\bar{x}$	σ
$\left(\frac{\partial p}{\partial t}\right)_\theta$	51	-0.53	±1.19
$\vec{V}\bullet\nabla_\theta p$	51	-1.59	±1.55
$\frac{\partial p}{\partial \theta}\frac{d\theta}{dt}$	51	-2.24	±2.49
ω_θ		-4.36	
$(\vec{V}-\vec{C})\bullet\nabla_\theta p$	51	-3.1	±1.3

	N	$\bar{x}$	σ
$\left(\frac{\partial p}{\partial t}\right)_\theta$	87	-0.4	±3.5
$\vec{V}\bullet\nabla_\theta p$	87	-3.3	±3.9
$\frac{\partial p}{\partial \theta}\frac{d\theta}{dt}$	87	-2.9	±4.0
ω_θ		-6.6	
$(\vec{V}-\vec{C})\bullet\nabla_\theta p$	87	-4.7	±5.1

	N	$\bar{x}$	σ
$\left(\frac{\partial p}{\partial t}\right)_\theta$	116	-0.9	±2.4
$\vec{V}\bullet\nabla_\theta p$	116	-2.0	±3.2
$\frac{\partial p}{\partial \theta}\frac{d\theta}{dt}$	116	-0.4	±2.3
ω_θ		-3.3	
$(\vec{V}-\vec{C})\bullet\nabla_\theta p$	116	-2.9	±4.5

Table 2.1: Statistical analysis of the terms in ω_θ. N is the sample size, $\bar{x}$ is the sample mean, and σ is the sample standard deviation. Values for $\bar{x}$ and σ are in μb s^{-1}. The value for ω_θ in the $\bar{x}$ column is the summation of the three mean component terms. Tables are as follows: upper-left quadrant: 292K at 2100 UTC 16 January 1994; upper-right quadrant: 304K at 1500 UTC 10 April 1997; lower-left quadrant: 302K at 0000 UTC 06 April 1999; lower-right quadrant: 290K at 2100 UTC 15 April 1999. Reproduced from Market et al. 2000.

the 4 cases. This work done by Market et al. (2000), especially along with forecasters at the Springfield (SGF) Weather Forecasting Office (WFO) spurred the development of this paper.

One of the most important parameters of isentropic coordinates is Ψ. Market et al. (2012) examined the history behind the use of Ψ. It has generally been frowned upon to compute Ψ from

the traditional equation: $\Psi = C_p T + gz$. Instead, an integrated approach by Danielsen (1959) has been the standard:

$$\Psi_2 = \Psi_1 + C_p \bar{T} \ln(\frac{\theta_2}{\theta_1}) \tag{2.29}$$

where the subscripts 1 and 2 denote the lower and upper level of Ψ, respectively. It is evident to see this is an iterative approach and in a sense, is the hypsometric equation in isentropic space. However, it is argued in the paper that through the advancement in the accuracy of radiosonde measurements, especially with the GPS-verified height data, that calculations of Ψ can be made accurately. Six separate radiosonde measurements were taken and compared between the traditional equation and the iterative equation. The difference between these two equations was calculated as:

$$Difference = \left(1 - \frac{\Psi}{\Psi_2}\right) x\ 100 \tag{2.30}$$

It was observed from the six comparisons that the difference was roughly 0.2%. Therefore, the quality of radiosonde observations has improved to the point that the standard equation for calculating Ψ can be used with no little error introduced.

Chapter 3: Derivation of the Isentropic Omega Equation

This section provides an overview of the derivation of the continuity equation, θ, an expression for the diabatic heating, and the equation used in this study.

Part I: The Continuity Equation

To begin, the Lagrangian differential in Cartesian coordinates is defined:

$$\frac{d\xi}{dt} = \frac{\partial \xi}{\partial t} + \frac{dx}{dt}\frac{\partial \xi}{\partial t} + \frac{dy}{dt}\frac{\partial \xi}{\partial t} + \frac{dz}{dt}\frac{\partial \xi}{\partial t} \tag{3.1}$$

where ξ is a conservative property. Next, define $dx/dt = u$, $dy/dt = v$, and $dz/dt = w$. Thus, (3.1) can be rewritten as:

$$\frac{d\xi}{dt} = \frac{\partial \xi}{\partial t} + u\frac{\partial \xi}{\partial t} + v\frac{\partial \xi}{\partial t} + w\frac{\partial \xi}{\partial t} = 0 \tag{3.2}$$

(3.2) can be further condensed to vector notation:

$$\frac{\partial \xi}{\partial t} + \nabla \cdot \left(\rho \vec{\xi}_3\right) = 0 \tag{3.3}$$

In which ϱ is density, and $\vec{\xi}_3$ is the 3-D ξ vector. Now, if $\frac{\partial \xi}{\partial t}$ is neglected, then (3.3) states that the 3-dimensional ξ vector multiplied by density is non-divergent. The expression within the parenthesis of (3.3) can be expanded to yield:

$$\frac{\partial}{\partial x}(\rho\xi)\hat{\imath} + \frac{\partial}{\partial y}(\rho\xi)\hat{\jmath} + \frac{\partial}{\partial z}(\rho\xi)\hat{k} = 0 \tag{3.4}$$

Moving the last expression on the left hand side (LHS) to the right hand side (RHS) will reveal:

$$\nabla \cdot \left(\rho \vec{\xi}_h\right) = -\frac{\partial}{\partial z}(\rho\xi)\hat{k} \tag{3.5}$$

Where $\vec{\xi}_h$is the horizontal components of the ξ vector. In the atmosphere, density cannot be assumed to be constant, thus the hydrostatic approximation must be invoked:

$$\delta z = -\frac{\delta p}{\rho g} \tag{3.6}$$

where *p* is pressure and *g* is gravity. The hydrostatic approximation, of course, states that the atmosphere is essentially statically stable (pressure decreases with increasing altitude, *z*). Now, given a sample volume *V*:

$$\delta V = \delta x \delta y \delta z \tag{3.7}$$

Using the definition from (3.6), and multiplying through by density, (3.7) becomes:

$$\delta V \rho = -\delta x \delta y \frac{\partial p}{g} \tag{3.8}$$

Note that on the LHS, volume times density is simply the mass, so $\delta V \rho = \delta m$. Further assuming that the Law of Conservation of Mass holds and invoking finite differencing techniques, (3.8) will become:

$$\frac{d}{dt}(\delta m) = -\delta x \delta y \frac{\partial p}{g} \tag{3.9}$$

which can be further manipulated to yield:

$$\frac{1}{\delta m} = \left(-\delta x \delta y \frac{\partial p}{g}\right)^{-1} \tag{3.10}$$

Taking the product solutions of (3.9) and (3.10) will reveal that gravity cancels from both equations. Upon setting both equal to 0 and factoring will yield:

$$\frac{1}{\delta x \delta y \delta p}\left[\frac{d(\delta x)}{dt}\delta y \delta p + \frac{d(\delta y)}{dt}\delta x \delta p + \frac{d(\delta p)}{dt}\delta x \delta y\right] = 0 \tag{3.11}$$

To simplify, the chain rule is invoked:

$$\frac{1}{\delta x}\delta\left(\frac{dx}{dt}\right) + \frac{1}{\delta y}\delta\left(\frac{dy}{dt}\right) + \frac{1}{\delta p}\delta\left(\frac{dp}{dt}\right) = 0 \tag{3.12}$$

From here, it is noted that dx/dt, dy/dt, and dz/dt = u, v, and w, respectively from (3.2). Also, dp/dt is simply ω, or upward vertical motion in Cartesian coordinates. Finally, letting $\delta \rightarrow \partial$, (3.12) becomes:

$$\frac{\partial u}{\partial x} + \frac{\partial v}{\partial y} + \frac{\partial \omega}{\partial p} = 0 \tag{3.13}$$

Condensing will yield:

$$\nabla \cdot \vec{V}_h = -\frac{\partial \omega}{\partial p} \tag{3.14}$$

which is the continuity equation in isobaric coordinates. This is of fundamental importance as it states that horizontal convergence (divergence) is related to upward (downward) changes in vertical motion. The derivation of (3.14) is essentially another way of explaining Dine's Compensation Principle; lower (upper) level convergence is compensated by upper (lower) level divergence, resulting in UVM (DVM). Plugging (3.14) into (3.2) yields:

$$\frac{d\xi}{dt} = \frac{\partial \xi}{\partial t} + \nabla \cdot \vec{\xi}_h + \omega\frac{\partial \xi}{\partial p} = 0 \tag{3.15}$$

(3.15) states that for any conservative property, ξ, its Lagrangian rate of change is simply the sum of its Eulerian rate of change, and the sum of the 3D $\vec{\xi}$ vector. Note how the advection terms are time negligible.

Part II: Derivation of θ

From experimental data, the First Law of Thermodynamics (FLOT) can be written as:

$$dQ = c_v dT + P d\alpha \tag{3.16}$$

where Q is the amount of heat absorbed/released, T is temperature, c_v is the specific heat of air under constant volume, and α is specific density. Invoking the equation of state to rewrite the second term on the RHS and through some algebraic manipulation, (3.16) becomes:

$$dQ = c_v dT + (-\alpha dP + R_d dT) \tag{3.17}$$

where R_d is the dry gas constant. Combining the dT terms to define $R_d + c_v = c_p$, or the specific heat of air under constant pressure, the 'perfect' form of the FLOT is derived:

$$dQ = c_p dT - \alpha dP \tag{3.18}$$

(3.18) is coined the 'perfect' form because it is generally more useful than (3.16). From here, we assume an adiabatic process, such that dQ = 0, and invoking the equation of state once more and dividing both sides of the equation by $R_d T$ will yield:

$$\frac{c_p}{R_d}\frac{dT}{T} = \frac{dP}{P} \tag{3.19}$$

Upon integration and invoking basic logarithm rules, one arrives at:

$$T = T_0\left(\frac{P}{P_0}\right)^{\frac{R_d}{c_p}} \tag{3.20}$$

where the subscripts *0* denote initial values. (3.20) is known as Poisson's equation, stating that T is the temperature a parcel of air would have if brought dry adiabatically to some reference level P,

characteristically taken to be 1000 hPa. (3.20) is more readily viewed as:

$$\theta = T_0\left(\frac{1000}{P_0}\right)^{\frac{R_d}{c_p}} \tag{3.21}$$

Therefore, by definition, θ is a conservative property. Next, the natural logarithm of (3.21) is invoked and the result is multiplied through by c_p:

$$c_p \frac{d\theta}{\theta} = c_p \frac{dT}{T} - R_d \frac{dP}{P} \tag{3.22}$$

Next, if (3.18) is divided by T and the equation of state is implemented, then (3.22) will become:

$$\phi = \frac{dQ}{T} = c_p \frac{d\theta}{\theta} \tag{3.23}$$

in which ϕ has been defined as the specific entropy. Integrating (3.23) will ultimately yield:

$$\phi = c_p \ln(\theta) + C \tag{3.24}$$

whereby if θ is constant, then the entropy is constant. This is termed an isentropic process.

From the continuity equation derived in (3.15), it has been stated that θ can be treated as a conservative property. Thus, ξ can be replaced by θ in (3.15):

$$\frac{d\theta}{dt} = \frac{\partial\theta}{\partial t} + \mathrm{V}\cdot\nabla\theta + \omega\frac{\partial\theta}{\partial p} = 0 \tag{3.25}$$

Or, more realistically, we can define θ_e to include not only the measure of the heat of a parcel, but its moisture content as well, (3.25) becomes the equation of moist continuity (or moist entropy):

$$\frac{d\theta_e}{dt} = \left(\frac{\partial\theta_e}{\partial t} + \mathrm{V}\cdot\nabla\theta_e\right)_p + \omega\frac{\partial\theta_e}{\partial p} = 0 \tag{3.26}$$

Part III: Redefining the Diabatic Heating Term

Following the notation from Emanuel et al. (1987), s = $c_p \ln(\theta)$ and s* = $c_p \ln(\theta_e)$. From this new definition, because *s** is a state variable, if the atmosphere is saturated (100% relative humidity), it can be rewritten in terms of two other variables, namely *s* and *p*, such that:

$$(ds*)_p = \left(\frac{\partial s*}{\partial s}\right)_p ds \tag{3.27}$$

From this new definition of d*s**, anytime *s** is acted upon during an isobaric process, *s** will become *s*. Thus, the continuity equation for *s** can be written as:

$$\frac{ds*}{dt} = \left(\frac{\partial s*}{\partial s}\right)_p \left(\frac{\partial s}{\partial t} + \mathrm{V} \cdot \nabla s\right) + \omega \frac{\partial s*}{\partial p} = 0 \tag{3.28}$$

Multiplying further by (3.27) and invoking the new notation for d*s**, d*s*/d*t* may be rewritten as:

$$\frac{ds}{dt} = -\omega \left(\frac{\partial s}{\partial s*}\right)_p \left(\frac{\partial s*}{\partial p}\right) + \omega \frac{\partial s}{\partial p} = 0 \tag{3.29}$$

or, more readily as:

$$\frac{ds}{dt} = \omega\left[\frac{\partial s}{\partial p} - \left(\frac{\partial s}{\partial s*}\right)_p \left(\frac{\partial s*}{\partial p}\right)\right] \tag{3.30}$$

Now, $\left(\frac{\partial s}{\partial s*}\right)_p$ can be rewritten such that if s is a function of *p* and α,

$$\left(\frac{\partial s}{\partial s*}\right)_p = \left(\frac{\partial s}{\partial \alpha}\right)_p \frac{\partial \alpha}{\partial s*} \tag{3.31}$$

The two terms on the RHS of (3.31) can be expanded to yield more intuitively appealing expressions. Starting with the first term on the RHS of (3.31), the definition for s is invoked to show that:

$$\left(\frac{\partial s}{\partial \alpha}\right)_p = \left(\frac{\partial c_p \ln(\theta)}{\partial \alpha}\right)_p \tag{3.32}$$

Through the ideal gas law, the RHS of (3.32) can be shown to equal

$$\left(\frac{\partial c_p \ln(\theta)}{\partial \alpha}\right)_p = \frac{pc_p}{R}\frac{\partial ln\theta}{\partial T}\Big|_p \tag{3.33}$$

where the subscript *p* indicates the differential is operated on a constant pressure surface. Carrying out the differential yields

$$\left(\frac{\partial c_p \ln(\theta)}{\partial \alpha}\right)_p = \frac{pc_p}{R\theta}\frac{\partial \theta}{\partial T} \tag{3.34}$$

The second term on the RHS is a form of Poisson's equation (3.21), which cancels with the θ in the denominator in the first term on the RHS. This results in:

$$\frac{pc_p}{R\theta}\frac{\partial \theta}{\partial T} = \frac{pc_p}{RT} \tag{3.35}$$

Which, invoking the ideal gas law once more will reveal:

$$\frac{pc_p}{RT} = \frac{c_p}{\alpha} \tag{3.36}$$

which is the desired result in (3.31)

Next, Emanuel (1985) showed how the second term on the RHS of (3.31) can be redefined. Starting with the FLOT including moisture:

$$\text{Tds}^* = c_v dT + Pd\alpha - Lq \tag{3.37}$$

where *L* is the latent heat of vaporization, and *q* is the mixing ratio. Next, defining *h**:

$$\text{h}^* = c_v dT + P\alpha - Lq \tag{3.38}$$

which is the saturation enthalpy and taking the derivative of (3.38):

$$dh* = d(c_v dT) + Pd\alpha + \alpha dP - Lq \tag{3.39}$$

The first two terms on the RHS of (3.39) = (3.37). Thus, (3.39) can be reduced to:

$$dh^* = Tds^* + \alpha dP \tag{3.40}$$

From here, it can be deduced that:

$$\left(\frac{\partial h*}{\partial p}\right)_{s*} = \alpha \quad \text{and} \quad \left(\frac{\partial h*}{\partial s*}\right)_p = T \tag{3.41}$$

As stated earlier, because *h** is a state variable:

$$\left(\frac{\partial}{\partial s*}\right)_p \left(\frac{\partial h*}{\partial p}\right)_{s*} = \left(\frac{\partial}{\partial p}\right)_{s*} \frac{\partial h*}{\partial s*_p} \tag{3.42}$$

Which, invoking the definitions from (3.45), (3.42) will be reduced to:

$$\left(\frac{\partial \alpha}{\partial s*}\right)_p = \left(\frac{\partial T}{\partial p}\right)_{s*} \frac{1}{\theta_e} \tag{3.43}$$

by implementing the same process as in (3.32) – (3.36) to achieve the $\frac{1}{\theta_e}$ term. Next, realizing that $\left(\frac{\partial T}{\partial p}\right)_{s*}$ is essentially the moist adiabatic lapse rate, Γ_m, and that $\frac{c_p}{\alpha}$ is the inverse of the dry adiabatic lapse rate, Γ_d, it can be shown that:

$$\left(\frac{\partial s}{\partial s*}\right)_p = \frac{\theta}{\theta_e}\frac{\Gamma_m}{\Gamma_d} \tag{3.44}$$

which, when plugged back into (3.30), and changing $s \rightarrow \theta$ and $s^* \rightarrow \theta_e$, the end result is reached:

$$\frac{d\theta}{dt} = \omega\left[\frac{\partial \theta}{\partial p} - \frac{\theta}{\theta_e}\frac{\Gamma_m}{\Gamma_d}\frac{\partial \theta_e}{\partial p}\right] \tag{3.45}$$

Part IV: The Final Equation

Beginning with (3.45), it can be noticed the LHS of the term in brackets is the adiabatic component for a rising parcel, and the RHS of the term in brackets is the diabatic change. This can be qualitatively stated such that for a parcel beginning ascent in the lower troposphere, the rate of ascent will be equal to that of the dry adiabatic lapse rate ($\sim 10K\ km^{-1}$) since the parcel is not saturated. The level where the dry adiabatic lapse rate intersects the nearest mixing ratio value on a thermodynamic diagram (such as the skew-t) indicates the level where the parcel will become saturated: the LCL. Since the parcel is saturated, any ascent will cause a diabatic change due to the parcel condensing moisture, releasing latent heat, adding a diabatic contribution to the overall term. Therefore, as seen from (1.3), if the diabatic term (hereafter, Dia) is larger than the adiabatic term (hereafter, Adia), the overall expression will be negative on the RHS; thus upward (downward) vertical motion is associated with diabatic heating (cooling). This should make intuitive sense, as long as a rising parcel is warmer than the ambient atmosphere; it should be buoyant and rise. Upon realizing that (1.3) is only one-half of the 3rd term in (1.2), multiplying through by the dry static stability and assuming the background vertical motion is approximated by the adiabatic vertical motion (first and second terms in (1.2)) will yield:

$$\frac{\partial p}{\partial \theta}\frac{d\theta}{dt} = \omega_{adia}\frac{\partial p}{\partial \theta}\left[\frac{\partial \theta}{\partial p} - \frac{\theta}{\theta_e}\frac{\Gamma_m}{\Gamma_d}\frac{\partial \theta_e}{\partial p}\right] \tag{3.46}$$

The logic behind substituting the adiabatic vertical motion for the total vertical motion is as follows. In the synoptic scale environment (scales ranging from 2,000-10,000km, Orlanski, 1975), layered clouds and stratiform precipitation form due to isentropic upglide since the parcel becomes saturated. A parcel must reach its LCL (adiabatic changes within the parcel) before any diabatic processes can occur within it. Therefore, within the lowest 1.5-3 km of the surface, large-scale adiabatic processes should be the primary forcing for an ascending parcel of air. In other words, the

diabatic contribution cannot engage without the broader, synoptic (first ordered adiabatic) forcing present first for lifting to saturation.

Next, through algebraic manipulation, (3.46) becomes:

$$\frac{\partial p}{\partial \theta}\frac{d\theta}{dt} = \omega_{adia} - \omega_{adia}\left[\frac{\Gamma_m}{\Gamma_d}\frac{\theta}{\theta_e}\frac{\partial \theta_e}{\partial p}\frac{\partial p}{\partial \theta}\right] \tag{3.47}$$

which is the full expression necessary for estimating the 3rd term in (1.2). As noted previously, the broader synoptic scale isentropic upglide must occur, which will be estimated through the adiabatic contribution of lift, given by the two terms on the RHS of (1.2). Thus, (1.2) becomes:

$$\omega_\theta = \omega_{adia} + \omega_{adia} - \omega_{adia}\left[\frac{\partial \theta}{\partial p} - \frac{\Gamma_m}{\Gamma_d}\frac{\theta}{\theta_e}\frac{\partial \theta_e}{\partial p}\right] \tag{3.48}$$

where

$$\omega_{adia} = \left(\frac{\partial P}{\partial t}\right)_\theta + \vec{V}\cdot\nabla_\theta P \tag{3.49}$$

Much like how the moist adiabatic lapse rate is simply the dry adiabatic lapse rate with a moist adjustment, (3.48) assumes the isentropic vertical motion is simply an adiabatic process (3.49) with a diabatic adjustment, given by (3.47). Notice in (3.48), every term is readily calculable, which will be undertaken by a script to calculate each term using GEMPAK. The procedure of such a script will be described in the following section.

Chapter 4: Data and Methodology

The GEMPAK software was used for the data manipulation for this study. Calculations of $\frac{d\theta}{dt}$ have been thoroughly described as being a rather arduous task (Uccellini 1976), but through the implementation of Emanuel et al.'s (1987) work, later redefined by Cammas et al. (1994), (3.48) can be directly substituted into (2.21) for calculations that are readily available from grid fields on a daily basis. Before the calculations can be made, careful considerations of the dependent variables must take place to ensure the data are representative of the study. Questions pertaining to these variables before the data can be gathered include:

- Time. At what forecast time in the model will the data be calculated, and how far of a forecast should be implemented from the initialization time?
- Which atmospheric model should be used?
- Which isentropic surface should be used?
- Will there be a geographic restriction?

This section answers these questions which are pertinent before a script can be developed, and will also address how the script will be implemented through GEMPAK functions that will calculate the necessary information.

Radiosondes are launched from WFO's daily at 00Z and 12Z, thus, 00Z and 12Z (6am and 6pm CST) were the initialization times used. In other words, any values of ω will be taken as the "truth" in the isobaric framework, while each term in (3.48) will be calculated separately. Since this thesis attempts to test whether model ω and calculated ω_θ are equal, forecasts will be made based on the 00Z and 12Z initialization data to ensure continuity. Nowcasting tends to be utilized best with atmospheric models that have the shortest temporal resolution (i.e., the NCEP-RAP (National Center for Environmental Prediction - Rapid Refresh, or simply RAP). However, the RAP also has

a small horizontal resolution which would not be representative of the synoptic-assumption made earlier (Barnes et al. 1996); short termed forecasts should be omitted. From a dynamical chaos (Lorenz, 1963) point of view, a long termed forecast should not be made as well. This idea stems from the fact that even the initialization times are incapable of producing infinitely precise data; i.e. there is already inherent error within the data. If two datasets started from only very slightly different initial conditions, their two time evolutions should eventually diverge (Wilks 2011). This would occur from the interpolations process explained below (due to rounding errors). Therefore an 18 hr forward forecast from the initialized 00Z and 12Z times will be implemented up to 48 hours at 6-hour intervals (i.e., F018, F024… F048). The 18-48 hours should encapsulate the capability of statistical representativeness, and the 6-hour intervals are based upon the model chosen (described below).

For this study, the NAM model was used opposed to the RAP and the GFS. The reasons for not implementing the RAP are attributable to the spatial resolution of the model: the RAP resolves data at a horizontal grid-point spacing of 13-km, which, according to Orlanski's (1975) classification scheme is well below the synoptic-scale (Figure 4.1). In theory, the RAP could be used, however, its spatial resolution does not comply with the adiabatic vertical motion assumption. Also, the models forecasted times only extend to 12-hrs, limiting the capability of this study to determine whether (3.48) is suitable for WFO's to adopt in their daily analysis. The choice of neglecting the GFS over the NAM was arbitrary; i.e. either model could have been used for this study. For example, ω and ω_θ are being treated as if they are the same value, which is the ultimate goal. Therefore, theoretically, successive forecasts should reveal that these two values should also remain the same. In other words, it would not matter which synoptic-scale model was used, as it should be calculating the same values through successive forecasts. Due to the different cumulus parameterization schemes used for each model, there should be a difference in the values of ω and

ω_θ between the NAM and GFS, but would stay internally consistent if using only one specific synoptic-scale model throughout. Future study of the comparisons between ω and ω_θ with the NAM and the GFS should be examined, but doing so is outside of the focus for the current work. The NAM has been selected and systematically "thinned" from its original 13-km horizontal resolution to 80-km (NAM-211). This allows for calculations on the upper-end of the mesoscale, and lower-end of the synoptic-scale (Figure 4.1), which should not produce noise at this resolution (Barnes 1996) and allow for the most accurate data calculations.

Due to the synoptic-assumption made in (3.48), isentropic surfaces that should be below the LCL are used. The final script was written at the end of 2013 October, so data would be analyzed for the late fall and most of winter (November through February) on a daily basis. Since these surfaces shift vertically depending on the season (i.e. colder temperatures correlate to colder isentropic surfaces near the surface), colder surfaces are used than if the study were to be carried out in the summer. For this study, 292K and 300K are appropriate as they reside between the surface and roughly 700 hPa for most of the winter. These surfaces tend not to intersect the ground nor rise above the normal level of the LCL, which is roughly 750 hPa for most circumstances. However, as one moves west towards the Rocky Mountains, these surfaces may no longer exist due to the high surface elevation. Therefore, the only geographic restriction of this study is roughly west of the CO border.

With the following information, the script was developed and run based on the variables described above:

- 00Z and 12Z initialization times.
- F018 – F048 forecasts in 6-hour intervals; F018, F024, F030, F036, F042, and F048.
- NAM thinned to an 80-km grid
- Primarily cool season study

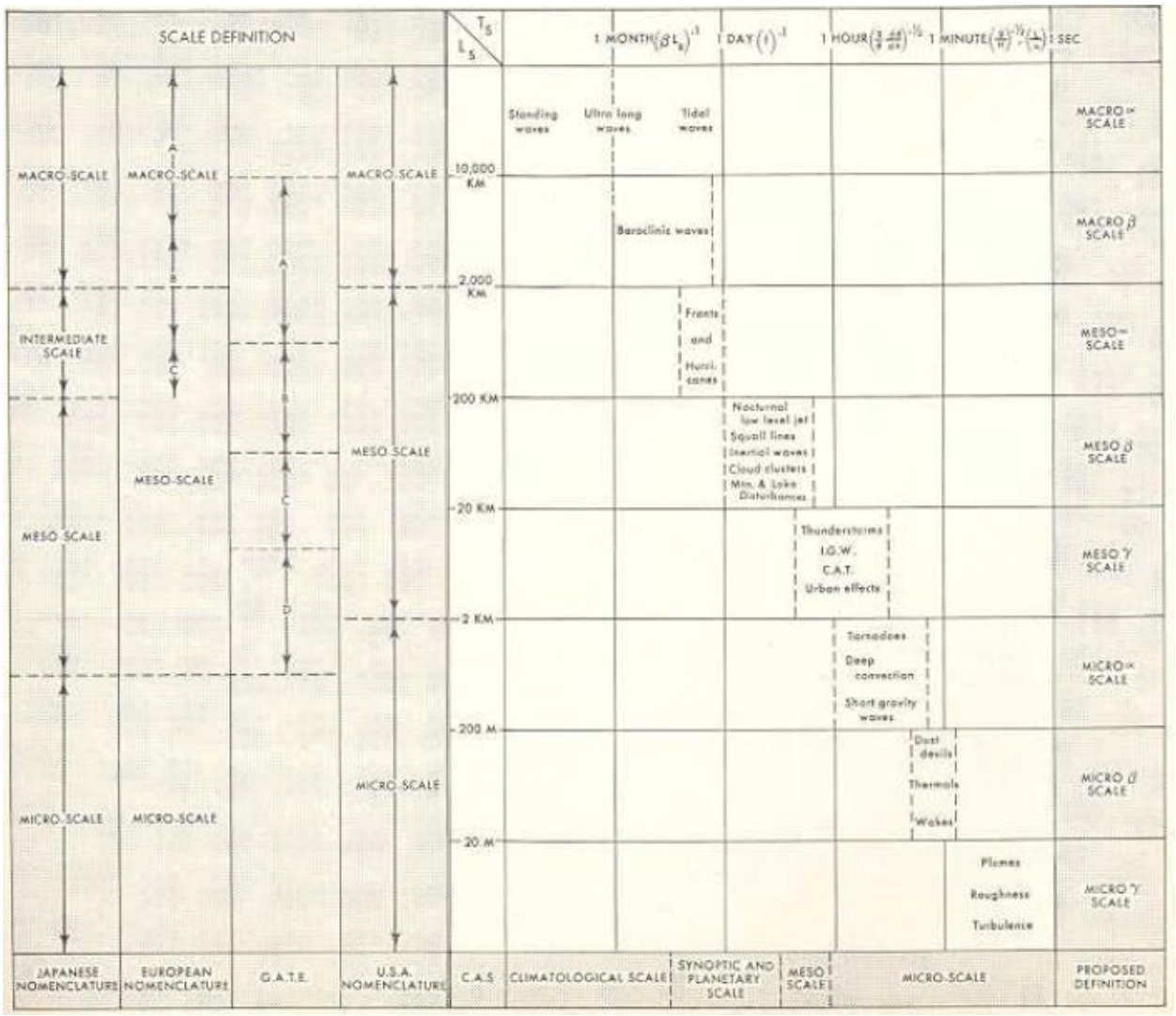

Figure 4.1: Scale definitions and different processes with characteristic time and horizontal scales. Reproduced from Orlanski 1975.

- 292K and 300K isentropic surfaces
- East of the Rockies

The first step of the script is to ensure the data are in isentropic coordinates. The atmospheric model output that is originally produced by NCEP which is eventually delivered to the University of Missouri is in isobaric coordinates; a conversion to isentropic space must occur. GEMPAK's *gddelt* (grid delete) program is used to clear a copy of the original NAM files of its isobaric data. Next, the isentropic data is interpolated through the *gdvint* program (vertically

interpolate data to a different vertical coordinate (i.e., pressure to isentropic)) permitting the parameters in (3.48) to be calculated. For the script, where there exists a temporal derivative, a 6-hour backwards difference approach was invoked ensuring computational stability. Each term in (3.43) is calculated to acquire a quantitative value of ω_θ through the *gddiag* (creates and computes derived quantities into a grid file) program. Because each calculation through *gddiag* requires a unique function output name, ω_θ has been labeled as ADOE (Adiabatic Omega Equation), ω is simply OMEG, and the computed field $\omega_\theta - \omega$ is ADER (ADiabaticERror).

Before the script can be run, a specific geographic region must be considered. Since ADOE is attempting to compute the diabatic component correctly, it would logically follow that areas where diabatic processes are occurring should be analyzed. Although diabatic process include solar heating and latent heating, the latter is easier to analyze. This is true since if the local relative humidity (RH) along an isentropic surface is greater than 80%, one could assume that diabatic processes are occurring, such as condensation. However, condensation does not always initiate at 80%, so only local regions where the RH $\geq$ 95% were analyzed to ensure a more realistic assumption of latent heating processes actually occurring. Therefore, *gdcntr* (grid contour) was invoked to contour regions where ADOE were non-zero and were contained with an area overlaid with stippled regions where RH $\geq$95%. Images were created with this criterion to view areas that would be suitable for analysis, and regions outside of this criterion were masked out. Once these regions have been identified, the nearest meteorological station with an International Civil Aviation Organization (ICAO) code was recorded, and for the specific isentropic surface, initialization/forecasted times, *gdlist* (lists the data at each successive data point) was run to get an output for OMEG, ADOE, and ADER. Each location that was suitable for analysis consisted of a 17x17 grid-scale (17x17 points, all of which had 80-km horizontal grid spacing) with the ICAO station centered. The 17x17 grid-scale was arbitrarily chosen, but is justified as nearly every image generated with a stippled RH region seldom expanded

beyond 1,000 km in either the zonal or meridional direction, thus ensuring as much data collection as possible. The dates used for this study spanned from October 30 2013 to January 25 2013. The final acquisition of data would be collected and grouped as follows:

00Z	→292K	→F018, F024, F030, F036, F042, F048
	→300K	→F018, F024, F030, F036, F042, F048
12Z	→292K	→F018, F024, F030, F036, F042, F048
	→300K	→F018, F024, F030, F036, F042, F048

Within the ensuing chapters, the following notation will be used:

30 Dec 2013 00F048 292K

This indicates that the isentropic surface used was 292K, with an initialized time of 00Z forecasted 48-hr into the future, with the finalization period being 30 Dec 2013 at 00Z. Thus, the time the actual forecast was made would be 28 Dec 2013 at 00Z. Another example would be:

01 Jan 2014 12F036 300K

where the initial forecast was made 36-hr prior to 12Z on Jan 01 2014, or 31 Dec 2013 at 00Z.

Chapter 5: Statistical Analysis

As described in Chapter 4, each individual grid-point was calculated for values of OMEG, ADOE, and ADER (collectively hereafter referred to as OAA). Each individual day that met the criterion of an area where RH values exceeded 95% were calculated through a script, whereas the unsaturated regions were filtered out. To obtain numerical values, *gdlist* was run to quantitatively represent each value that was calculated by the GEMPAK script. The initial data that was calculated included OAA over several regions of the CONUS while remaining east of the Rockies and north (south) of Canada (Mexico). The 17x17 grid-scale calculated a possible 289 points, each 80km apart in the horizontal centered over the region of interest. After obtaining data from each script run, there was a noticeable discrepancy between the number of data points analyzed, which can be observed via Tables 1-4. For instance, the average number of points analyzed for all forecasted runs for 00Z 292K was 1250, but the range consisted of 900 points for the F042 run up to 1507 points for the F036. Since so many data-points were calculated, this did not affect the overall statistical analysis. In Table 5.1, a trend exists such that the statistics perform better the further the forecasted time is run; i.e. F018 tended to perform the worst. The average ADER for the F018 run was ~ 3.1μbs^{-1}, which does not reflect the actual average ADER value. There were 28 days that were calculated for F018 with a sum of 1414 data points, where OAA values were computed on a daily basis, but averaged overall in Table 5.1. On a daily basis, there was no pattern in any of the statistical parameters. For example, November 24 was analyzed at Lubbock Preston Smith International Airport (KLBB) and consisted of an average ADER of -2.22 μbs^{-1}, standard deviation of 1.32 μbs^{-1}, and 85 data points were used. In contrast to the November 26 run at Pittsburgh International Airport (KPIT), the same values were 3.45 μbs^{-1}, 11.38 μbs^{-1}, and 83, respectively, indicating a large spread for ADOE. Roughly the same number of data points was calculated, yet

Table 5.1: 00Z initialization time on the 292K surface for all forward times. All parameters along the left-most column are as follows: Average: average ADER for each forward time run; Skew: average skew of ADER; StDev: average standard deviation of ADER; Correl: average correlation between ADOE and OMEG; Count: the sum of the number of data points used for each forward run; MSE: mean square error between ADOE and OMEG; and RMSE: root-mean-square-error between ADOE and OMEG. All Average and StDev values are in μbs^{-1}. The right-most column calculates the overall average for all forward times.

00Z 292K	F018	F024	F030	F036	F042	F048	Overall Average
Average	3.05105	2.12788	0.58845	0.22936	1.57954	2.03973	1.60267
Skew	-0.0944	-0.1631	-0.0845	-0.1526	-0.0461	0.20823	-0.0554
StDev	3.45767	3.8655	3.76261	3.62913	2.74678	2.88447	3.39103
Correl	0.17036	0.19676	0.32619	0.28821	0.32927	0.27081	0.2636
Count	1414	1356	1507	1384	900	937	1249.67
MSE	73.4018	93.4745	40.2281	55.3099	16.8979	26.5771	50.9816
RMSE	7.42215	8.1355	5.92297	6.20217	3.51276	3.86277	5.84305

ADER was of opposite sign. Contrary to what would be assumed with a negative ADER (OMEG > ADER), on the 24th (26th), the correlation was positive (negative), implying ADER generally overestimated (underestimated), but there was a modest positive (negative) correlation of the data. Many of the data points featured a negative value for OMEG yet ADOE calculated a positive value, which was a recurrent trend for all 00Z 292K runs, where the number of daily points analyzed ranged from 9 to 107. In spite of the fact that appreciable statistical analysis is generally ran for over 30 data points (Wilks 2011), the days with small number of points were kept. This lies with the assumption that ADOE should be within range of values of OMEG, overall minimizing the value of ADER. The maximum ADER value was ~3.05 μbs^{-1}, and a minimum value was the F036 with an average difference of ~0.230 μbs^{-1}, the overall ADER average was calculated to be ~1.603 μbs^{-1} with a modest positive correlation of the data. What is most revealing is the overall average negative skew of the data. Although not a strong value for each run, the daily analysis saw a strong trend towards relatively high ADOE values while OMEG remained relatively negative, resulting in a large

Table 5.2: 00Z initialization time on the 300K surface for all forward times. All parameters along the left and right-most columns are the same as in Table 5.1.

00Z 300K	F018	F024	F030	F036	F042	F048	Overall Average
Average	7.75752	5.7726	4.15422	2.32319	0.80945	1.2009	3.66965
Skew	-0.0206	-0.5606	0.32176	0.25236	0.36808	0.17042	0.08857
StDev	4.03938	5.83846	3.63508	3.48793	2.8534	2.73842	3.76544
Correl	0.1373	-0.0229	0.24255	0.33105	0.25198	0.28828	0.20471
Count	1373	1321	1415	1252	1452	1249	1343.67
MSE	163.813	140.098	78.0145	37.1988	16.4328	13.2663	74.8039
RMSE	10.915	9.6263	7.04302	5.33869	3.56275	3.23168	6.61958

ADER (leading to the overall negative skew). The negative skew for most of the runs (F018 – F042) averaged overall to a negative value, yet the modest positively skewed data for F048 implies a large frequency of small ADER values. This also is indicative of a large but infrequent number of large outliers in the positive direction (ADER > OMEG).

Table 5.2 reveals the same information as Table 5.1, but for the 00Z 300K data. Much like the 292K surface, the 300K surface tends to perform most poorly at the F018 run. However, there is an apparent decreasing trend in the forecast runs for the average ADER, standard deviation, and MSE/RMSE. The average ADER minimum occurs at F042 rather than F048 (the furthest forecasted time), yet there is a decreasing linear trend as forecast times increased from the initialization time. Unlike the data for the 00Z 292K runs, Table 5.2 displays that the number of data points analyzed were the highest, not the lowest for the F042 run, which could possibly help to explain why the correlation was relatively weak compared to the 00Z 292K data. Opposite to what was observed at 292K, the overall Skew is positive, with F018 and F024 remaining negative. However, the student t-test for significance was above the 99% confidence level.

Table 5.3: 12Z initialization time on the 292K surface for all forward times. All parameters along the left and right-most columns are the same as in Table 5.1.

12Z 292K	F018	F024	F030	F036	F042	F048	Overall Average
Average	3.60626	1.88498	2.91613	2.66137	0.06114	0.58623	1.95269
Skew	0.07121	-0.0895	0.09617	0.06707	0.11544	0.03041	0.04846
StDev	3.31162	3.52059	3.71036	3.17458	2.31659	1.93339	2.99452
Correl	0.16103	0.28187	0.11133	0.12895	0.40844	0.30023	0.23197
Count	1574	1475	1136	1357	1506	1531	1429.83
MSE	111.316	84.3	69.8863	37.5684	12.3236	6.72993	53.6873
RMSE	8.98846	8.21542	7.27993	5.2674	3.07056	2.25723	5.8465

The overall trend of decreasing error in the average ADER data is further represented through Table 5.3, showing the 12Z 292K data. Although the correlation is best seen through the MSE/RMSE, it can be seen for the average ADER and standard deviation, especially the last 3 forward times. The F036, F042, and F048 runs all have the smallest standard deviations and MSE/RMSE values, and the overall best values for average ADER with the exception of the F024 run. Nonetheless, the F018 data are noticeably worse than F048 for every parameter (e.g., 3.6 (0.59) for F018 and F048 Average, respectively), with the possible exception of the number of data points analyzed, albeit there were only 43 less points for the F048 run. The student t-test of significance revealed that, again, correlation resulted in above 99% confidence for the 12Z 292K data.

The last run for all of the data segregated by forward times was 12Z 300K. Although there should be little-to-no correlation between the initialization times used, the different isentropic surfaces tend to produce similar results. For instance, Table 5.4 has a clear depiction of the negative relationship between forecast time and average ADER, standard deviation, and MSE/RMSE. Although the relationship is weak for the average of all times, the data still lies within the 99% confidence level. There also is a directly positive correlation between forecast time and correlation with the minor exception of the F024 and F030 data.

Table 5.4: 12Z initialization time on the 300K surface for all forward times. All parameters along the left and right-most columns are the same as in Table 5.1.

12Z 300K	F018	F024	F030	F036	F042	F048	Overall Average
Average	7.33455	4.67238	4.74219	2.06633	1.21541	0.97111	3.50033
Skew	0.19293	0.17954	0.07373	0.36779	0.39852	0.16843	0.23016
StDev	4.34135	4.24312	3.73134	3.18073	2.47909	2.67864	3.44238
Correl	0.04528	0.04518	0.15883	0.13309	0.22698	0.38782	0.1662
Count	1307	1366	1271	1293	1111	1240	1264.67
MSE	135.509	93.5933	103.133	31.6597	12.6219	13.7234	65.0401
RMSE	10.028	8.41884	8.20682	4.81552	3.1522	3.16756	6.29816

With the four separate isentropic levels and initialization times analyzed for each forecasted run, the overall averages are shown via Table 5.5. First, it should be noted that the overall average ADER is ~3.04 μbs^{-1}. Although the daily analysis revealed little-to-no information about how well (3.43) performed, the broad view of all data being evaluated shows a clear picture. The variability in the ADER values of the everyday runs ranged from -11.617 μbs^{-1} to 28.286 μbs^{-1}, nearly a 40 μbs^{-1} difference. It is also clear that the 292K surfaces outperformed the 300K data in nearly every field. Although the initialization times should not matter overall, they were implemented for the sake of adequate data collection. The average ADER values for the 292K surface were 2 μbs^{-1} less than for the 300K data. Although this is not a major difference, it could be the difference between overestimation or underestimation for a forecasted model's precipitation values. Due to the underlying physics of each scheme (e.g. Janjic 2000; Kain 2004; Han and Pan 2011), the overall values of specific parameters (such as moisture and vertical motion) can be the difference between the scheme being turned on or turned off. For instance, if the background vertical motion is -3.0 μbs^{-1}, the scheme may be turned off as the parcel in such a hypothetical atmosphere does not have enough momentum to reach its LCL or the Level of Free Convection (LFC). However, a value of

Table 5.5: Overall averages for every forward time step on each initialization time and isentropic level. Parameters along the left-most column are the same as in Table 5.1. The right-most column is the overall average for each initialization time and isentropic level consisting of each forward time step.

	00Z 292K	12Z 292K	00Z 300K	12Z 300K	Overall Average
Average	1.602668	1.9526859	3.6696464	3.5003281	3.04089
Skew	-0.055402	0.0484602	0.088571	0.2301565	0.1224
StDev	3.3910253	2.9945224	3.765444	3.442377	3.40078
Correl	0.2636004	0.2319739	0.2047101	0.1661974	0.20096
Count	1249.6667	1429.8333	1343.6667	1264.6667	1346.06
MSE	50.981556	53.687319	74.803851	65.040072	64.5104
RMSE	5.8430542	5.8465028	6.6195771	6.2981636	6.25475

-3.1 μbs^{-1} might be enough for the parameterization scheme to be turned on, adding an inch of precipitation to a forecast in some extreme cases. Therefore, even small differences in initialized data can account for large errors in forecasting. Table 5.5 displays an average ADER ~3.04 μbs^{-1} summed over every day for each of the four groups of data. Therefore, over a near 3-month period, ADOE performed well compared to OMEG. On a daily-basis, however, the averages ranged substantially, as noted above. Due to ADER, on average, being positive, it is implicit that ADOE overestimated when compared to OMEG (since ADER = $\omega_\theta - \omega$).

The correlation, although small on average, was still better for the 292K isentropic surface. As mentioned previously, one of the major issues observed on a daily basis was the dichotomy between the sign of OMEG and ADOE. Averages over the entire 3-month period of the study revealed that there was agreement on a positive correlation; whenever OMEG values were large, so were ADER values. However, a large positive OMEG was often observed with a large negative ADER, contributing to the vast variability in the ADER values on a daily basis. There was no sufficient correlation between when this would occur, but was, on average, more common for

the 300K isentropic surface. Values of MSE/RMSE also revealed better values for the 292K isentropic surface in comparison to 300K, while the skew and standard deviation tend to be minimized for 292K, implying the data was not as spread compared to 300K.

With all of the data segregated among the two separate isentropic levels and initialization times, it was seen there was an apparent trend towards ADOE being closer in value to OMEG the further the forecast was ran from the initialization time. Table 5.6 displays this, where the negative relationship of forecast time to ADER is apparent. However, there appears to be a cusp in the minimum ADER values at F042, rather than at the ending F048 time. Future studies should address further forecasted times to test if F042 is the overall minimum for ADER, with possible shorter termed forecasts to examine if larger errors in ADOE occur. Not only does the data level off at F042 for ADER, but for MSE/RMSE as well. This indicates that the short-termed forecasts are prone to error opposed to longer-scaled forecasts, which is opposite to what would be intuitive of the standard of a model forecast. This intuition derives itself from the mathematics of a dynamically coupled first-order linear differential equation, explained by the concept of chaos (Lorenz 1963). Figure 5.1 helps to illustrate the information conveyed in Table 5.6 graphically, helping in the visual aid of the overall trend of the forward time steps and their impact on ADER, skew, standard deviation, and RMSE.

With an average ADER for all isentropic levels of ~3.041 μbs^{-1} and an average ADER for all forward times of ~2.681 μbs^{-1}, it would appear safe to assume that ADOE performed well. However, this 17x17 grid has horizontal dimensions of 1360 km, nearly half of the CONUS. Figure 5.2 depicts the 00Z 300KF048 run on Dec 20 2013 (forecast for Dec 21 2013 at 18Z). The centered region for this specific event was Indianapolis, Indiana (KIND). However, extending 1360 km in the x and y directions protrudes the data calculated through central Oklahoma. Mostly negative values of ADOE exist through the RH region in central AR and through the upper Ohio valley

Table 5.6: All forecasted time for each initialization run and isentropic surface. All parameters along the left-most column are the same as in Table 5.1. The right-most column is the overall average for each initialization time and isentropic level for the forecasted time along the abscissa.

	F018	F024	F030	F036	F042	F048	Overall Average
ADER	5.437345	3.6144629	3.1002476	1.8200605	0.91638	1.19949	2.68133
Skew	0.037283	-0.158414	0.1017948	0.1336491	0.209	0.14437	0.07795
StDev	3.787503	4.3669201	3.7098476	3.3680914	2.59896	2.55873	3.39834
Correl	0.128491	0.1252271	0.2097242	0.2203269	0.30417	0.31179	0.21662
Count	1417	1379.5	1332.25	1321.5	1242.25	1239.25	1321.96
MSE	121.0098	102.86645	72.815543	40.434193	14.569	15.0742	61.1282
RMSE	9.338421	8.5990156	7.1131854	5.4059457	3.32457	3.12981	6.15182

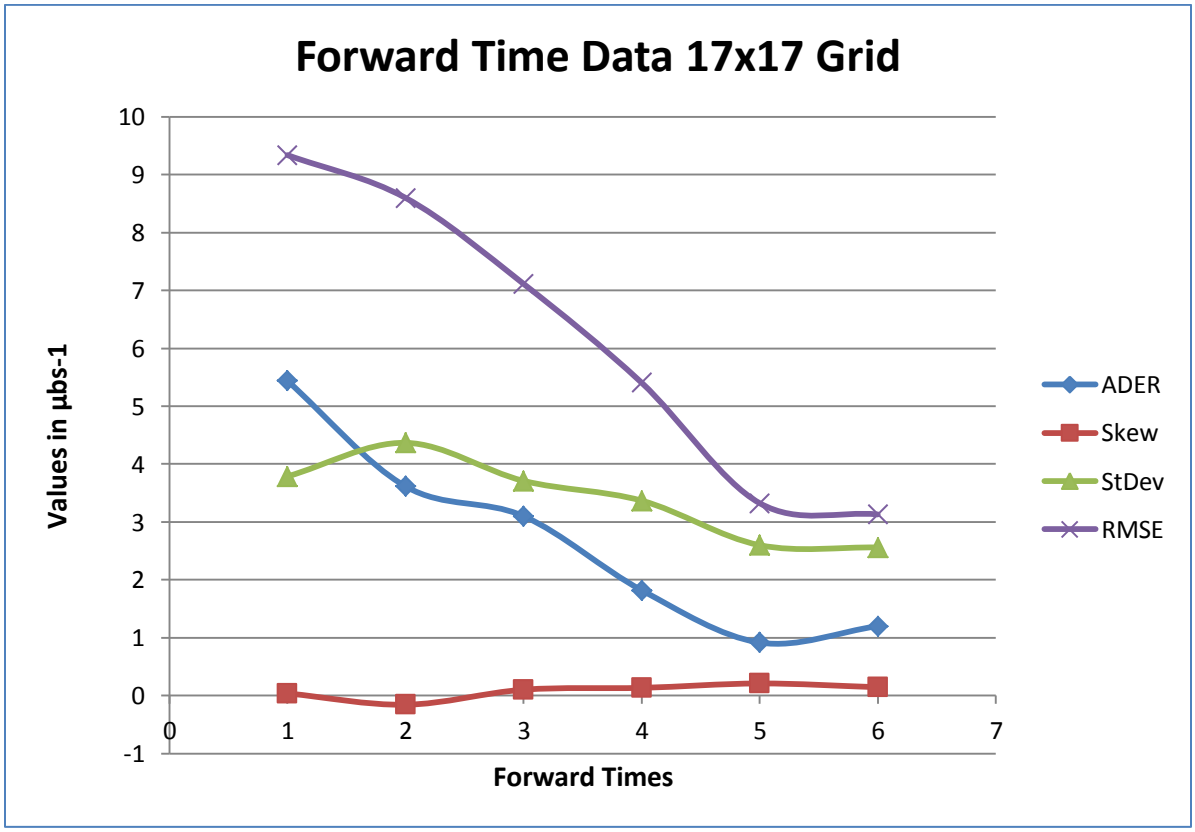

Figure 5.1: Graphical display of data from Table 5.6. X-values along the positive x-direction along the abscissa represent F018, F024, F036, F042, and F048 for 1-6 respectively. Values along the ordinate represent calculated statistical values.

region, yet a distinctive separate air mass is present along the Oklahoma/Arkansas border, outlined in Figure 5.3 which shows METARS for the forecasted time (1810Z on Dec 21). Northerly flow dominates the northern and westerns portions of the map, with a sharp change in wind direction just north and west of Norman, Oklahoma. With warmer temperatures to the east and cooler, drier air to the north and west coupled with the change in wind direction, a front is certain to exist outlined in the RH field within Figure 5.2 and the cold front given by Figure 5.3. Therefore, the data analyzed for this event was capturing two separate air masses. Along the cold front, dense cool air lifts the ambient warm air until saturation is reached and clouds form through condensation. This is directly correlated to the upward motions (negative ADOE values) along the eastern portion of the RH region in Figure 5.2, which perfectly outlines the region of the cold front. Although the forecast is nearly in agreement to what was observed via Figure 5.3, downward motion is forecasted for the southern portions of Oklahoma indicated in Figure 5.2. Thus, ADOE is averaging negative and positive values from two separate regions, which for this specific case ADER was calculated as ~-2.41 μbs^{-1}. Ideally, ADER should be 0, yet to test the actual validity of eqn. (3.45), single air masses should also be assessed to ensure consistency of all signs and the magnitude of ADOE are appreciable compared to OMEG. Therefore, a second test was run for the same regions on the same days, but for a 7x7 grid.

The script and data were all calculated the same, yet the centered station was reduced to 7 points in the x and y directions, rather 17, for calculation centered over the same spot. Therefore, the number of data points calculated decreases, yet a smaller area implemented for analysis appeals to forecast offices, especially when analyzing county warning areas (CWA's). Table 5.7 is comparable to Table 5.5 from calculating all forward times upon each isentropic surface and initialization time used in the study. Immediately noticeable are the average ADER values which are roughly an order of magnitude lower than the 17x17 ADER grid calculations. In comparison to the

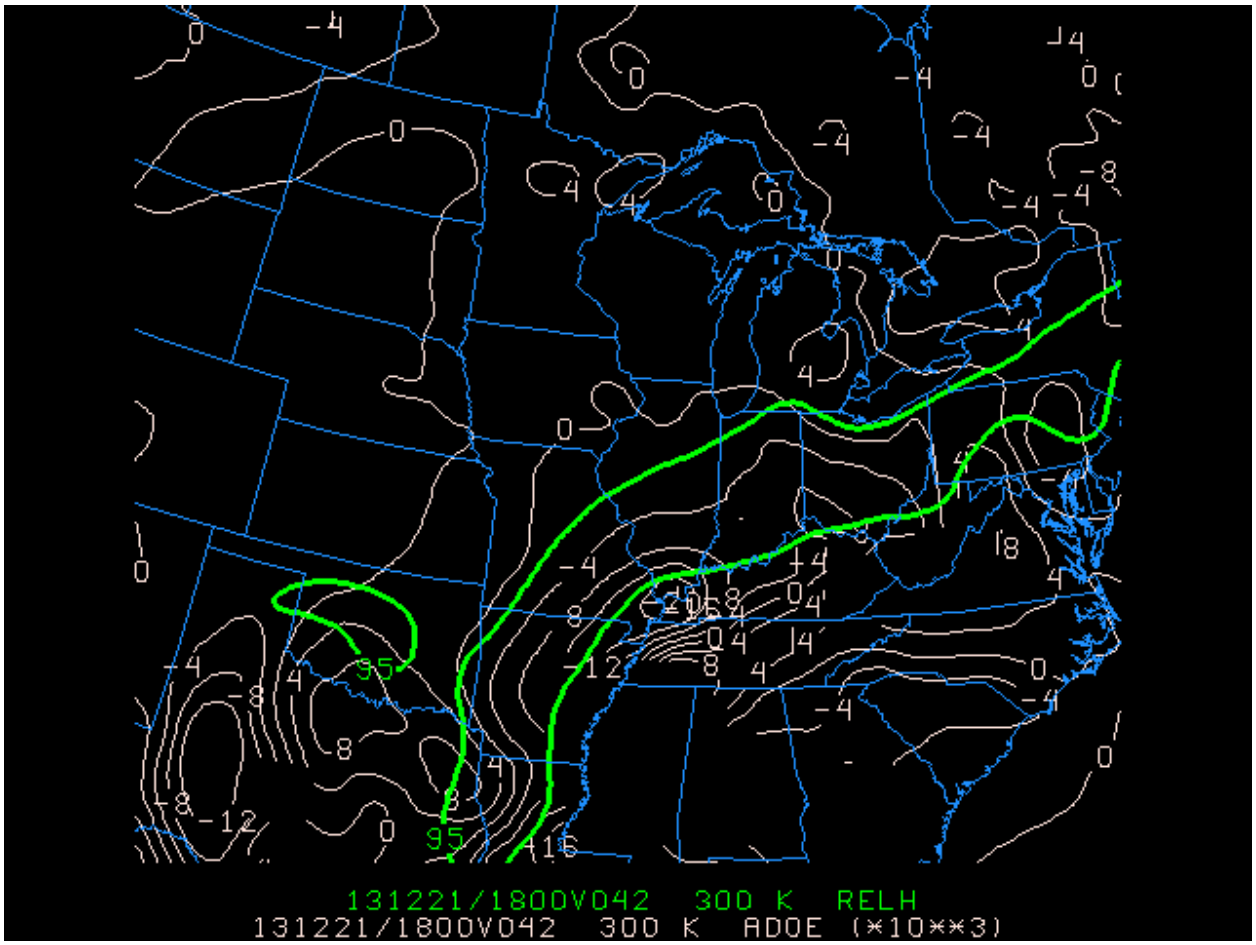

Figure 5.2: ADOE field (μbs^{-1}) for 00Z 300KF042 on Dec 20 2013. Solid white contours are ADOE (10^{-3} contoured every 2 μbs^{-1}) and the green contour represent regions where RH $\geq$ 95%.

example given through Figure 5.2, the 7x7 grid computed an average ADER of -0.377 μbs^{-1}. This trend was observed for all of the separate forecast times upon each initialization time and isentropic level, but has been omitted since the main statistics can be observed through Table 5.7. Much like Table 5.5 for the 17x17 grid, both of the 292K isentropic surfaces outperformed the 300K surfaces. Also, the standard deviation for the 7x7 data is halved for what was observed for the 17x17 grid. This is primarily due to the fact that the data is more concentrated to the central station of interest. What is of interest, however, are the correlation values. Table 5.7 shows that the overall correlation is hardly changed from the larger grid data, and was actually outperformed for the 12Z 292K data. With less data calculated (nearly 1/3rd of the number of points calculated from the 17x17 grid), the

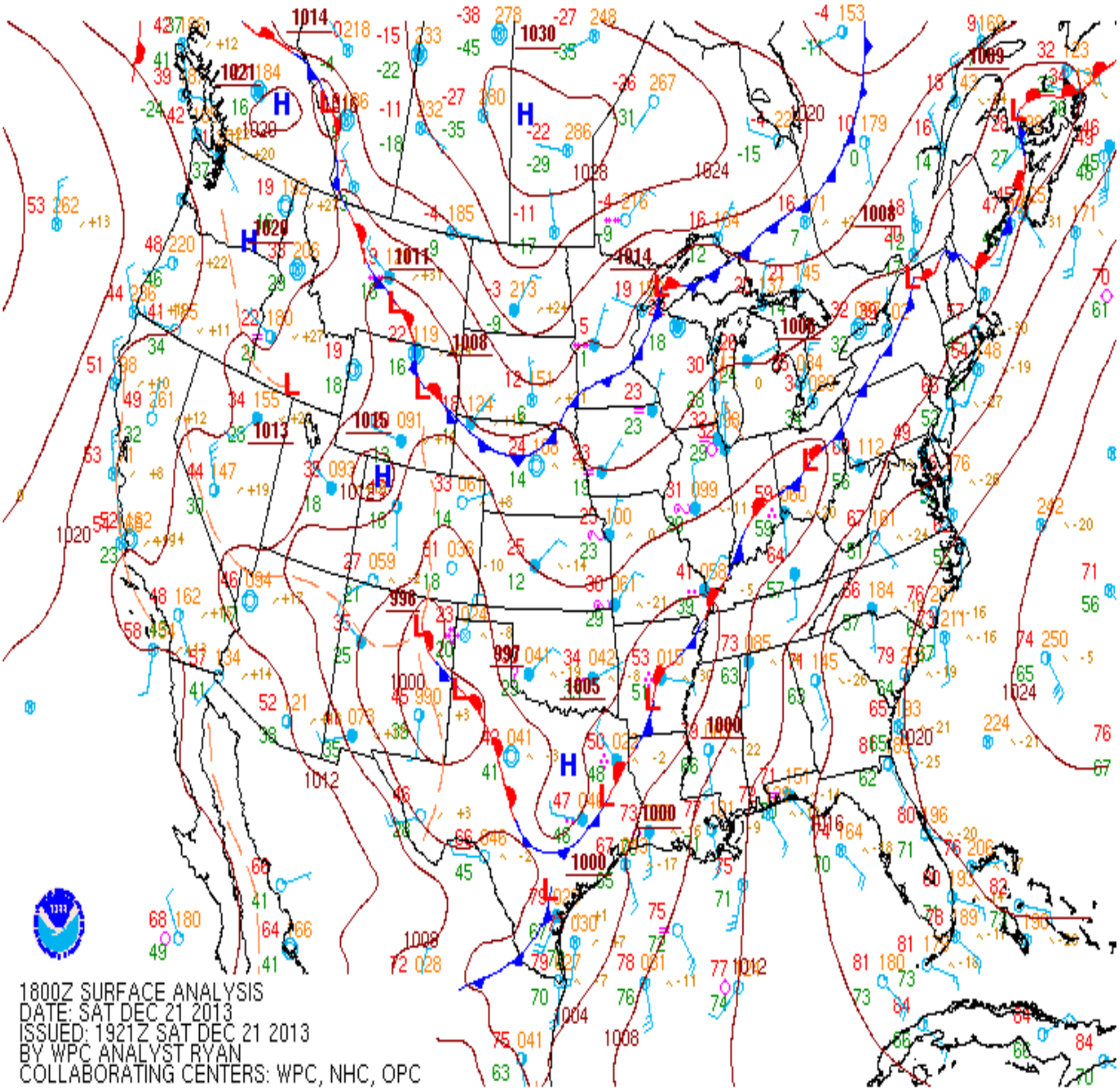

Figure 5.3: Surface METAR analysis for 1800Z on 21 Dec 2013. Standard Meteorological symbols are used. Taken from http://www.hpc.ncep.noaa.gov/

correlation should be expected to increase. However, this was not the case. The RMSE values have all significantly been reduced to less than 3 μbs^{-1}, with the lower isentropic level again proving to be more accurate than the 300K surface. For this data, the absolute error (AbsError in Table 5.7 and

Table 5.7: Same as Table 5.5 but for the 7x7 grid and the addition of the variable "AbsError" which calculates the absolute error of ADER.

	00Z 292K	12Z 292K	00Z 300K	12Z 300K	Overall Average
Average	0.232428	0.2087287	0.5155754	0.5195669	0.36907
Skew	-0.160801	-0.083877	0.5813421	0.4903326	0.20675
StDev	1.207077	1.097673	1.6898546	1.6110995	1.40143
Correl	0.372216	0.2238106	0.2422612	0.1951955	0.25837
Count	416.3981	356.97551	527	496.66667	449.26
MSE	5.595169	4.907633	13.290716	12.165168	8.98967
RMSE	2.039958	1.8997271	3.0417928	2.8989164	2.4701
AbsError	1.697218	1.57675	2.580386	2.4223063	2.06917

hereafter) was calculated to observe the trend of the actual magnitude of ADER. Much like what was observed via Figure 5.2, AbsError attempts to filter out the possibility of positive and negative values averaging to a near-zero value of ADER. When the difference of ADER and OMEG are calculated, the absolute value of ADER is then computed. Although this masks out the possibility of underestimation of ADOE, it can still be capture the overall average of ADER. Therefore, AbsError quantitatively characterizes the general magnitude of ADER, while the average takes into account the effects of the underestimation of ADER. From Table 5.7, the AbsError is ~2 μbs^{-1} larger than the average ADER, indicating that there were multiple events where OMEG > ADOE. Table 5.8 and Figure 5.4 display the same kind of data as Table 5.6 and Figure 5.1, respectively, except for the 7x7 grid as opposed to the 17x17 grid data. Unlike the 17x17 grid, the RMSE and Average tend to level-off by F030 rather F042. In fact, there is a minor increase in these values for F042 in the 7x7 grid. Yet, the overall values of the variables in Tables 5.8 and 5.9 are significantly less than for the 17x17 grid, as indicated by the change in the ordinate to compensate such a decrease in values. The overall decreasing trend in RMSE and average ADER seen in the 17x17 is much more pronounced than for the 7x7 grid.

Table 5.8: Same as Table 5.6 on the 7x7 grid and the inclusion of the variable "AbsError" which calculates the absolute error of ADER.

	F018	F024	F030	F036	F042	F048	Overall Average
Average	0.477798	0.430971	0.2970361	0.2558791	0.40339	0.34938	0.36907
Skew	0.355377	0.3393347	0.2201591	-0.004872	0.0142	0.31629	0.20675
StDev	1.542684	1.4240447	1.3284209	1.3277074	1.37653	1.40917	1.40143
Correl	0.247752	0.2373809	0.3061605	0.2514199	0.29529	0.21222	0.25837
Count	559.25	504.25	521.5	463	478.75	488.25	502.5
MSE	13.45269	8.7460345	7.4960763	8.1348539	8.60373	7.50464	8.98967
RMSE	2.902579	2.5277427	2.292494	2.329527	2.42618	2.34207	2.4701
AbsError	2.442133	2.1404983	1.929101	1.9604968	2.00609	1.93667	2.06917

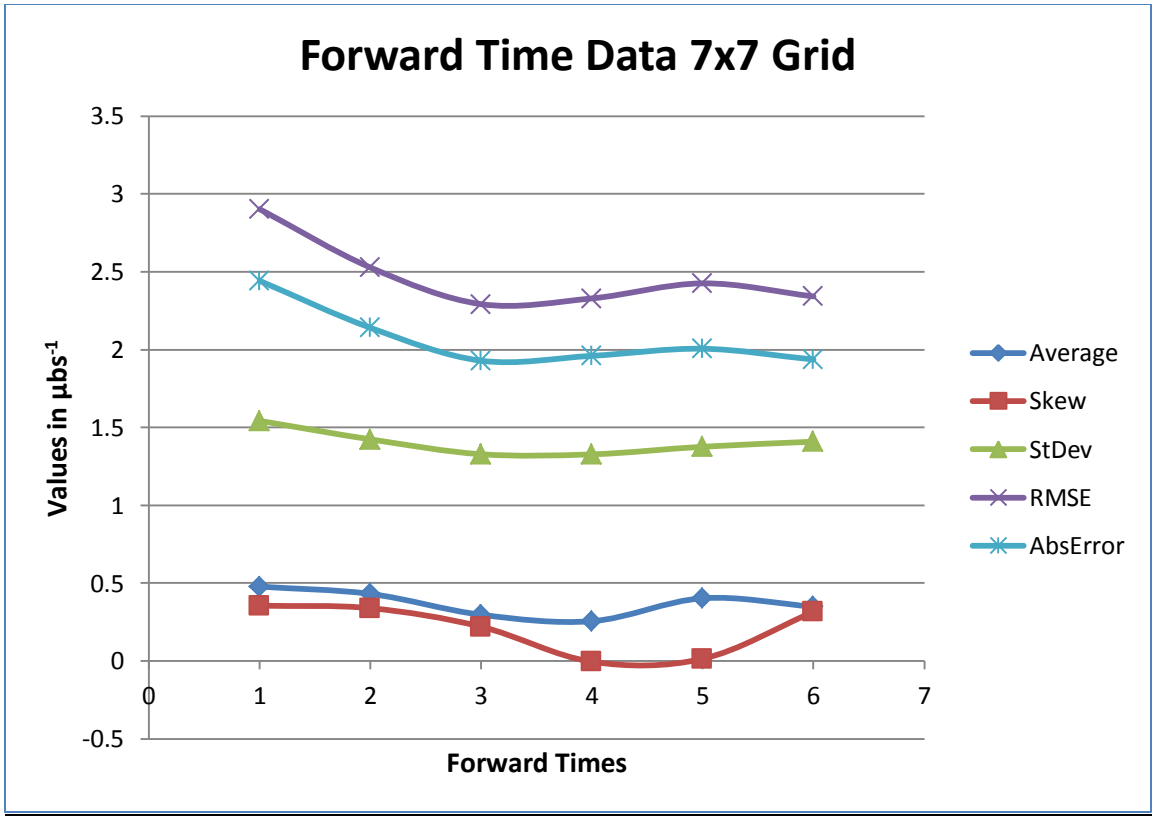

Figure 5.4: Same as Figure 2.15, with the inclusion of the variable "AbsError" which calculates the absolute error of ADER.

Table 5.9: Same as Table 5.7, but for ADIA data.

	00Z 292K	12Z 292K	00Z 300K	12Z 300K	Overall Average
Average	0.458392	0.4415726	1.0125638	0.926962	0.70987
Skew	0.328062	0.4082463	0.8508315	0.8863998	0.61838
StDev	1.160696	1.1061691	1.7697111	1.6784676	1.42876
Correl	0.377864	0.2485665	0.2394398	0.1813397	0.2618
Count	579.1667	582	605.16667	580.5	586.708
MSE	4.938703	4.4337646	13.545546	11.997999	8.729
RMSE	1.87201	1.8102284	3.0902878	2.9219619	2.42362
AbsError	1.580292	1.5004987	2.6319187	2.4496656	2.04059

With the smaller 7x7 grid outperforming the larger 17x17 grid substantially, it can be safe to assume eqn. (3.45) should be implemented as a sub-synoptic scale calculation, rather a planetary scale. Although the data appears to be within the range of ω, there is no precise way of deciphering whether the manipulation of the adiabatic vertical motion eqn. (1.2) is validated by the new eqn. (3.45). Thus, ADOE must be recalculated without the diabatic term eqn. (3.44) to ensure its internal consistency. This will also reveal whether there is a true bias of the diabatic contribution of the isentropic omega equation to over, or underestimate in comparison to OMEG. Since the 7x7 grid computations were smoother and produced better results, eqn. (3.44), hereafter ADIA, will be run on the smaller grid for calculations with the same days and times as the previous two calculations. Table 5.9 displays the data calculated for 7x7 ADIA, which is quantitatively very similar to Table 5.8 and the 7x7 data. The most noticeable exception is the Average ADER (which for the ADIA case would simply be $\omega_{adia} - \omega$) between both cases. The diabatic contribution is nearly halved when compared to ADIA, with the rest of the averages almost identical in numerical value. The only exception would be the skew, which is larger for ADIA, indicating there are less outliers within the calculated data. Although the intent of this study is the development of a real-time estimation of the

isentropic vertical motion equation with the inclusion of the diabatic term, Table 5.9 infers that the inclusion of the diabatic term is essentially negligible. The RMSE and AbsError are both exceptionally close to one-another, with ADIA slightly outperforming ADOE. A further evaluation of the data is seen through Table 5.10, where the forward times are listed, much like Tables 5.6 and 5.8. Since the data and patterns are essentially the same for the 7x7 ADER and 7x7 ADIA, separating each statistical variable among these two parameters reveals more information. Figure 2.19 has a manipulated ordinate to account for the minor differences between ADER and ADIA. From this graph, it is apparent that the inclusion of the diabatic term performs better than without it. The overall decreasing trend from F018 to F030 is represented for ADIA, yet ADER continues decreasing until F036. A slight increase in difference from OMEG occurs at F042 for both parameters, and another decrease for the F048 data. What is striking to note is that this is exactly the opposite from what is seen for the 17x17 grid via Figure 5.1. Even more surprising is the overall behavior of the correlation values for all three runs (Figure 5.6). There is an apparent cyclical pattern of the correlation for ADOE and ADIA, both of which follow the same pattern. The diabatic contribution outperforms the non-diabatic equation for F018, and less noticeably for F042.

However, the 17x17 grid has an overall increasing correlation trend, and even outperforms both of the smaller grids for F048. The absolute error is observed via Figure 5.7 between ADOE and ADIA, with an appreciable correlation between the two. However, ADIA outperforms the 7x7 ADOE for every forward time step.

From the data analyzed, it is seen that the 17x17 diabatic grid was outperformed by the two smaller grids, yet showed more statistical trends in the analysis than the two. Yet, between ADOE and ADIA, there was a negligible difference between the two equations with ADIA generally outperforming ADOE.

A final run was computed to test the actual day-to-day comparison of the diabatic versus the

Table 5.10: Same as Table 5.8, but for ADIA.

	F018	F024	F030	F036	F042	F048	Overall Average
Average	0.771328	0.7542587	0.6215425	0.6507931	0.74069	0.72063	0.70987
Skew	0.619775	0.7223308	0.6346757	0.5537359	0.41882	0.76097	0.61838
StDev	1.51385	1.4601438	1.3754368	1.401402	1.38599	1.43574	1.42876
Correl	0.211172	0.2398858	0.3371721	0.253798	0.29275	0.23604	0.2618
Count	640	593	601	551.5	562	572.75	586.708
MSE	11.76696	8.8756321	7.4541531	7.7829033	8.35138	8.14299	8.729
RMSE	2.740385	2.5024108	2.27887	2.3149855	2.34817	2.35691	2.42362
AbsError	2.330157	2.1319416	1.9066762	1.9483519	1.97562	1.95081	2.04059

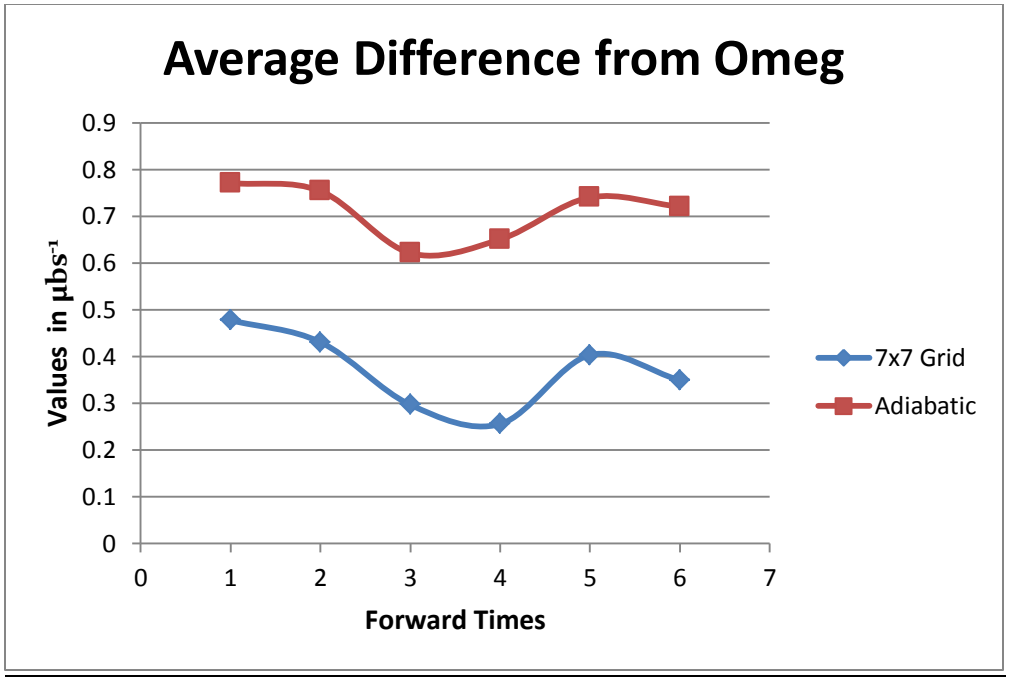

Figure 5.5: Average difference from OMEG between the 7x7 gridded data for ADOE and ADIA. Abscissa is the same as Figure 5.1

adiabatic isentropic vertical velocity equation. Instead of taking the actual quantitative values from each run, a binary system was implemented, where a "1" ("0") would indicate a day where inclusion of the diabatic term outperformed (was outperformed by) the adiabatic isentropic omega equation.

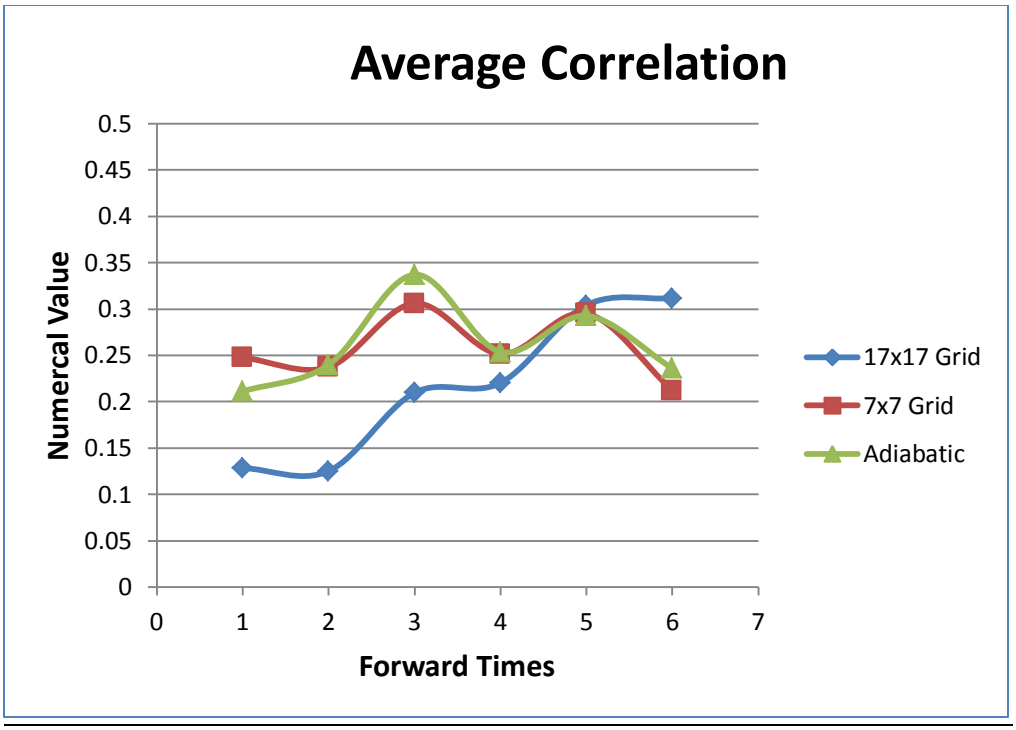

Figure 5.6: Same as Figure 5.5, but for average Correlation with the inclusion of the 17x17 grid-size data.

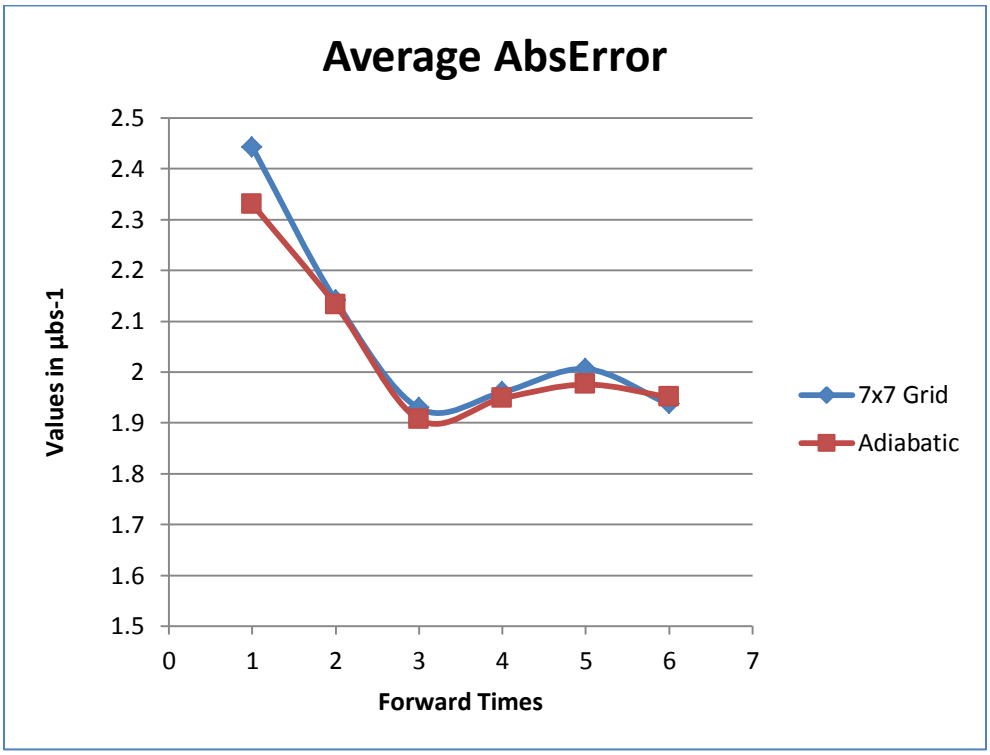

Figure 5.7: Same as Figure 5.5, but for average AbsError between ADOE and ADIA.

The number of days for each run is the first row for Tables 5.11 and 5.12. For example, the average number of days for the entire F018 run in Table 5.11 was 27.5 days, whereby the next row (Dia vs. Adia) indicates that out of these 27.5 days, eqn. (3.48) outperformed eqn. (3.49) 19.25 days. In other words, with the inclusion of the diabatic term, the error from the isentropic diabatic omega was closer to zero than for the adiabatic isentropic omega equation 70% of the time (for the F018 runs). The last row of calculated data, Avg Dif, calculated the daily difference between the diabatic (ω_d) and adiabatic (ω_a) isentropic vertical velocity equation:

$$Avg\ Dif = \omega_d - \omega_a \tag{5.1}$$

Therefore, wherever $\omega_d < \omega_a$, the diabatic term is rendering a more realistic value of ω. From the overall analysis on the daily runs as indicated by Table 5.11, the inclusion of the diabatic term quantifies a more realistic value to ω as opposed to the adiabatic omega roughly 70% of the time. Additionally, the average for Avg Dif displays the adiabatic omega equation overestimated. Although there was no apparent trend in the data for the forward times, there was a trend in Table 5.12 that the 00Z initialization times yielded better results for ω_d. From this analysis, this shows that, on average, ω_d outperforms ω_a nearly three-quarters of the time for a daily run. Although the quantitative analysis put a numerical value on the differences between ω_d and ω_a, the differences between the two were so miniscule that a day-by-day analysis helped to reveal that the inclusion of the diabatic term did, in fact, yield a better result for estimating ω than without it 70% of the time.

To gain further insight into why this might be the case, three case studies will be provided to expand upon bias towards any geographic regions, synoptic-scale weather patterns, or any specific days in general. This will reveal whether the equation specifically performs poorly in certain regions, whereby the issues can be addressed and possible conclusions can be drawn from any geographical biases.

Table 5.11: Day-to-day comparison of the diabatic versus the adiabatic isentropic vertical velocity equation. Down the left-hand side, the terms are: # Days: The numbers of days for each forward run was used in the computations; Dia vs. Adia: the number of days where the diabatic omega equation outperformed the adiabatic omega equation; Percent: the percentage of days where the diabatic omega equation outperformed the adiabatic omega equation; Avg Dif: average daily difference between the diabatic and adiabatic isentropic vertical velocity equation (in μbs^{-1}).

	F018	F024	F030	F036	F042	F048	Overall Average
# Days	27.5	23.75	24.75	21.75	22.5	22.5	23.792
DIA vs. Adia	19.25	16.75	18	15.75	15.75	15.25	16.792
Percent	70.06	70.62	72.659	72.899	71.138	69.253	71.105
Avg Dif	-0.0289	-0.319	-0.32	-0.382	-0.326	-0.375	-0.335

Table 5.12: Same as Table 5.11 but for initialization times and isentropic surfaces. Variables down the left-most column are same as in Table 5.11

	00Z 292K	12Z 292K	00Z 300K	12Z 300K	Overall Average
# Days	22.5	24.333	24.833	23.5	23.792
Dia vs. Adia	16.167	16.133	18.167	16.5	16.792
Percent	72.981	67.451	73.593	70.394	71.105
Avg Dif	-0.225	-0.224	-0.491	-0.492	-0.358

Chapter 6: Analysis: Case Studies

Case I: Springfield, Illinois: 12 Dec 2013 12ZF048 292K

The first case study is the 12 Dec 2013 12ZF048 292K run. The region of interest is the central-southeastern United States, centered over Springfield, Illinois (KSPI), and the forecast is valid for 14 Dec 2013 12Z. Figure 6.1 (A) is the GEMPAK generated ADOE image initialized at 12 Dec 2013 12Z, forecasted out 48 hours (valid on 14 Dec 2013 12Z). Since it is a forecast, it is not expected to be exactly accurate to the surface conditions that actually occurred. From the image generated, a bulls-eye of ADOE exists over Atlanta, Georgia, outside of the region of interest since it lies within a region where RH < 95%. Therefore, the main region of interest stems from central Illinois southward through Mississippi, with a northern protrusion eastward toward Norfolk, Virginia and a southern protrusion outlining the southern coast up through South Carolina. Without the southern protrusion, this would be a rather ideal setup for a mid-latitude cyclone; the low is centered roughly over Illinois, with the cold front extending down through Mississippi and the warm front protruding eastward through Virginia. A closer look at the GEMPAK generated OMEG image (Figure 6.1 (B)) for the same time shows a bulls-eye in upward motion through, roughly, Jackson Mississippi extending northward to Evansville, Indiana. This generates an ADER seen in (C) of Figure 6.1. Although the region of initial interest is KSPI, both of the small and larger grids will still be encompassed within most of the RH region, but the 17x17 grid will extend through the southern protrusion along the coast. Positive values are seen through western Tennessee and Virginia, while negative values extend along the southern protrusion. This indicates that ADOE estimated a larger than observed OMEG for the southern coast, and underestimated for western Tennessee and Virginia (since, as a reminder, ADER = $\omega_\theta - \omega$). To examine what causes this phenomenon to occur, a surface analysis image is displayed via Figure 6.2 for 14 Dec 2013 12Z.

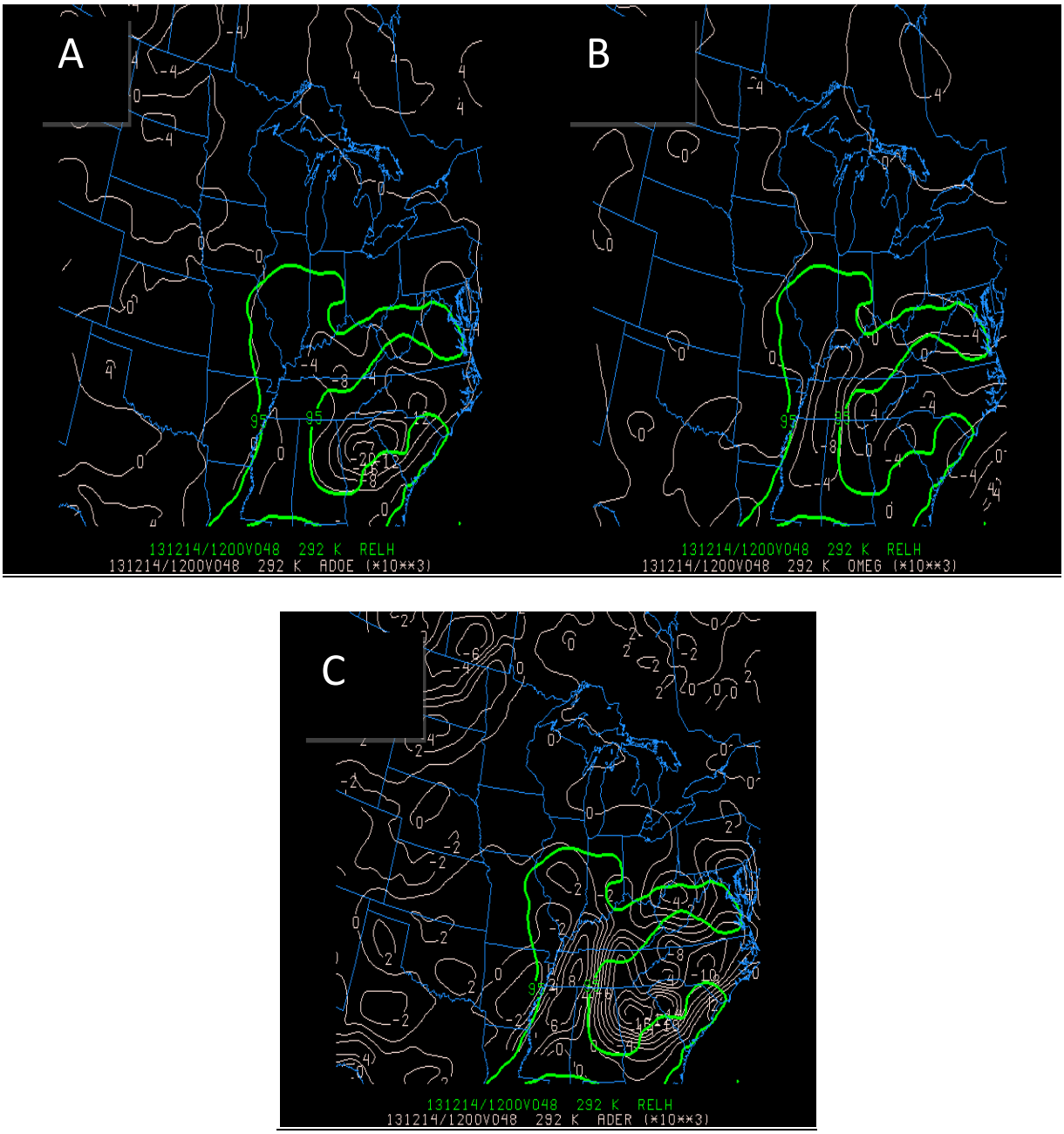

Figure 6.1: GEMPAK generated images for 12 Dec 2013 12ZF048 292K, valid for 14 Dec 2013 12Z. Contours and values are same as in Figure 5.2. Figures are as follows: A: ADOE, B: OMEG, C: ADER.

The outline of the moisture field from Figure 6.1 displays a coherent mid-latitude structure, although rather northerly displaced as seen from the surface map. The forecasted images depicted KSPI to lie just north of a surface low, with the cold front and warm front exhibiting most of the moisture,

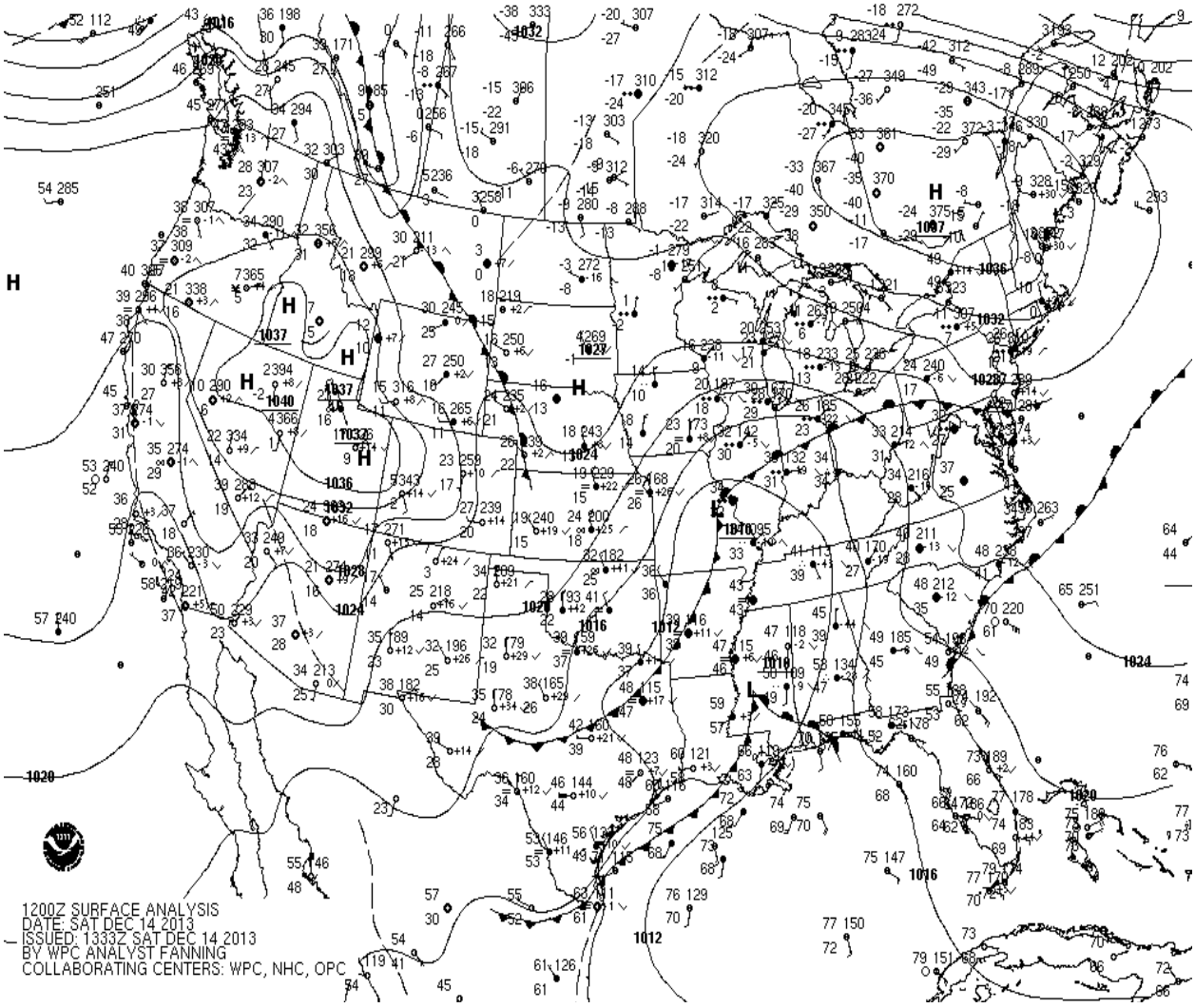

Figure 6.2: Surface analysis for 14 Dec 2013 12Z. Normal meteorological symbols are plotted. Generated from http://www.hpc.noaa.gov

consistent with the Norwegian Cyclone Model. Along the cold front is where ADOE underestimated (since upward motions are negative and downward motions are positive) the strength of OMEG. The cyclone over central MS eventually dies out over the next 4 hours, as the cyclolysis stage terminates the cyclone. The model over-predicts when and where this cyclone will die, resulting in an overestimate of vertical motion ahead of the warm front depicted in Figure 6.2. Although the exact specifications as to why this overestimation occurs is unknown, it is apparent

through this example that ADOE underestimates along the cold front, and overestimates within the warm sector. Due to the large extent of oscillatory positive and negative values, the 17x17 grid actually outperformed both of the 7x7 grids within this scenario. The average error values from OMEG were 0.348, 0.455, and 0.545 for the 17x17, 7x7 ADOE, and 7x7 ADIA, respectively. The RMSE values revealed that this averaging over the positive and negative values is the primary cause for the 17x17's grid to excel in this scenario as the values were 3.392 μbs^{-1}, 1.423 μbs^{-1}, and 1.483 μbs^{-1}, respectively.

Case II: Albert J Ellis Airport, North Carolina: 02 Jan 2014 00ZF024 300K

With the case of 12 Dec 2013 lying in the middle of Illinois, this next case examines how ADOE performs off the eastern coast (Figures 6.3 and 6.4). It could be argued that the moisture lying off of the Mid-Atlantic States could affect how ADOE performs. This logic stems from the fact that third term on the RHS of ADOE:

$$\omega_\theta = \omega_{adia} + \omega_{adia} - \omega_{adia}\left[\frac{\partial\theta}{\partial p} - \frac{\Gamma_m}{\Gamma_d}\frac{\theta}{\theta_e}\frac{\partial\theta_e}{\partial p}\right] \tag{6.1}$$

contains θ_e, which can be defined by the AMS glossary as:

"The equivalent potential temperature is the temperature a parcel at a specific pressure level and temperature would have if it were raised to 0 mb, condensing all moisture from the parcel, and then lowered to 1000 mb."

The quantitative equation for θ_e can be expressed as:

$$\theta_e = T_K\left(\frac{1000}{P}\right)^{0.2854(1-0.28\times10^{-3}r)} \times \exp\left[\left(\frac{3.376}{T_L} - 0.00254\right) \times r(1 + 0.81 \times 10^{-3}r\right] \tag{6.2}$$

where T_K is the absolute temperature, p is pressure, r is mixing ratio, and T_L is the temperature at the

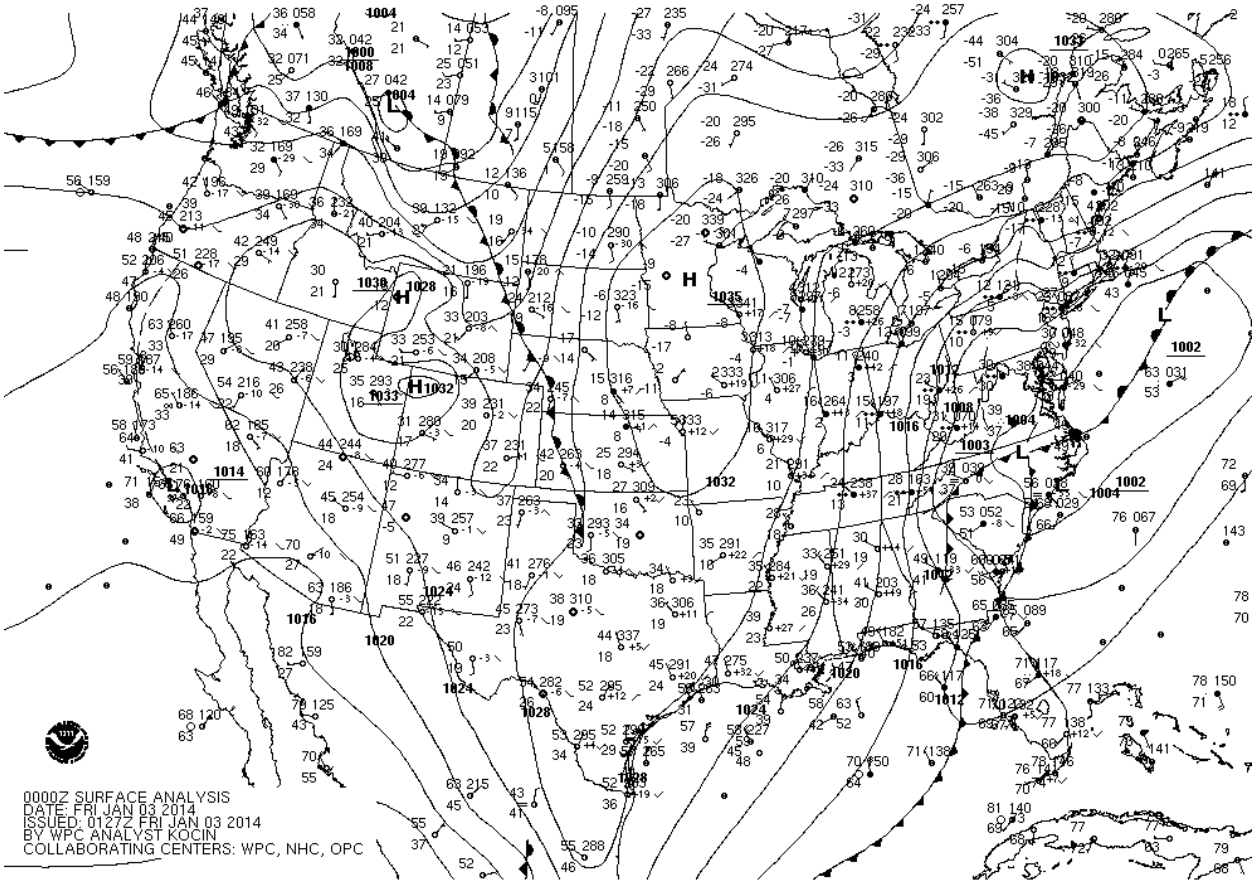

Figure 6.3: Surface analysis for 03 Jan 2014 00Z. Normal meteorological symbols are plotted. Generated from http://www.hpc.noaa.gov

LCL (Bolton 1980). Rossby (1932) devised the first equivalent potential temperature equation through neglecting the entropy of water vapor, equivalent to setting the specific heat of water to zero. One of the most accurate methods for calculating θ_e stems from Bolton (1980) yet has three adjustable parameters and is hard to interpret physically (Davies-Jones 2009) which is how GEMPAK calculates θ_e. Closer proximity to a permanent source of moisture and calculation of points within the Atlantic could introduce a misinterpreted ADOE.

Off the coast of North Carolina, Albert J Ellis airport (KOAJ) experienced an occluded front entering its decaying stages. The airport lies just south of the low, as seen in Figure 6.3.

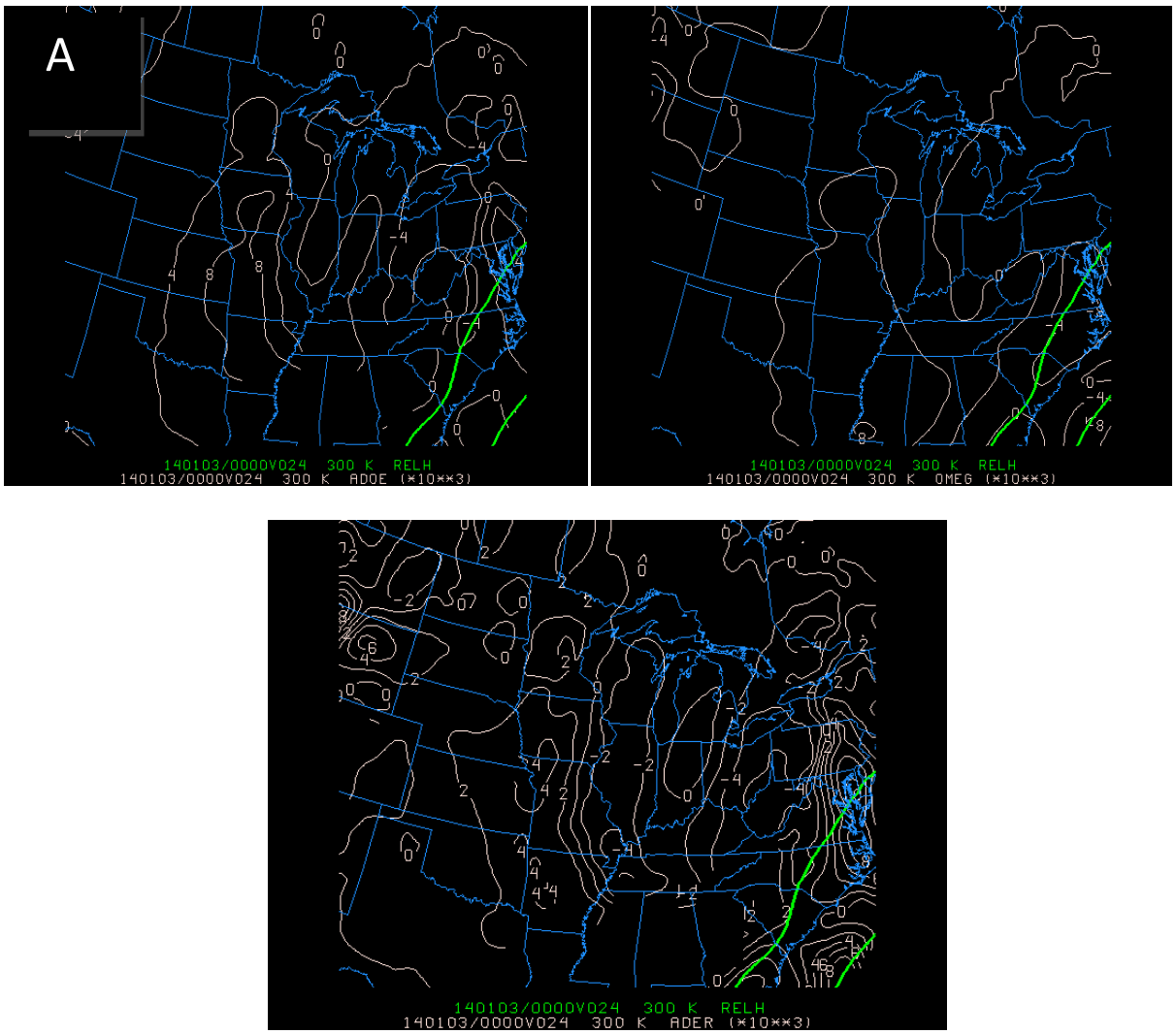

Figure 6.4: Same as Figure 6.1, but for 02 Jan 2014 00F024 300K.

Two separate cold fronts are plotted on the surface chart extending off the eastern coast through Charleston, South Carolina and into the Gulf of Mexico, while the other back-trails through Asheville, North Carolina. Although the front that extends south through the Gulf appears to be modest, the trailing cold front through North Carolina is more evident through the METAR shift in the wind field and drop in surface temperatures. The mid-latitude cyclone structure of the moisture field is not as evident as the previous case, especially due to the warm front extending off of the map. However, the same pattern as 12 December 2013 is seen through Figure 6.4: ADOE tends to

underestimate along the cold frontal boundary. ADOE values indicate there should be modest upward motion, but not nearly the magnitude that OMEG depicts. Observing the calculated field for ADOE shows that all values off the Atlantic coast are overestimated, whereas inland the calculations are of the correct sign with values of ADER approaching 0. This is revealed through the negative correlation field, whereas ADOE decreases near the coast as OMEG increase, resulting in an overall negative correlation since most of the data points lie over the Atlantic. The values of the 17x17, 7x7 diabatic, and 7x7 adiabatic grid were 9.548 μbs^{-1}, 1.692 μbs^{-1}, and 2.452 μbs^{-1}, respectively. A possible explanation for this trend in ADOE could be due to the influence of the moisture of the ocean on the equivalent potential temperature. An increase in the latent heat of vaporization increases the value of the exponential term, ultimately increasing the value of θ_e, which will, in turn, decreases the overall value of ω_θ.

Case III: Lubbock Preston Smith International Airport, Texas: 23 Nov 2013 00ZF036 292K

From the previous two cases, it was observed that within the vicinity of an approaching low pressure system, the error for all three grid-fields would perform poorly. This case is centered in Lubbock Texas, where high pressure dominates over the eastern central plains (Figure 6.5). A rather impressive 1044-hPa high is centered near Quincy, Illinois, with frigid temperatures encompassing most of the contiguous US. The Lubbock, Texas METAR indicates graupel is present with a northeasterly flow. Haze, mist, and light precipitation are present in the surrounding area, indicating that latent heat release from precipitation is nearly imminent. The images in Figure 6.6 indicate the forecasted RH field lies in near-comparison with what was actually observed. As a result of the high pressure dominating most of the US, there is near perfect agreement between OMEG and ADOE, yet the ADER field reveals minor error outside of the RH field in OK and southern KS. Since this area lies outside of the RH region, they have not been calculated. The error values for the 17x17,

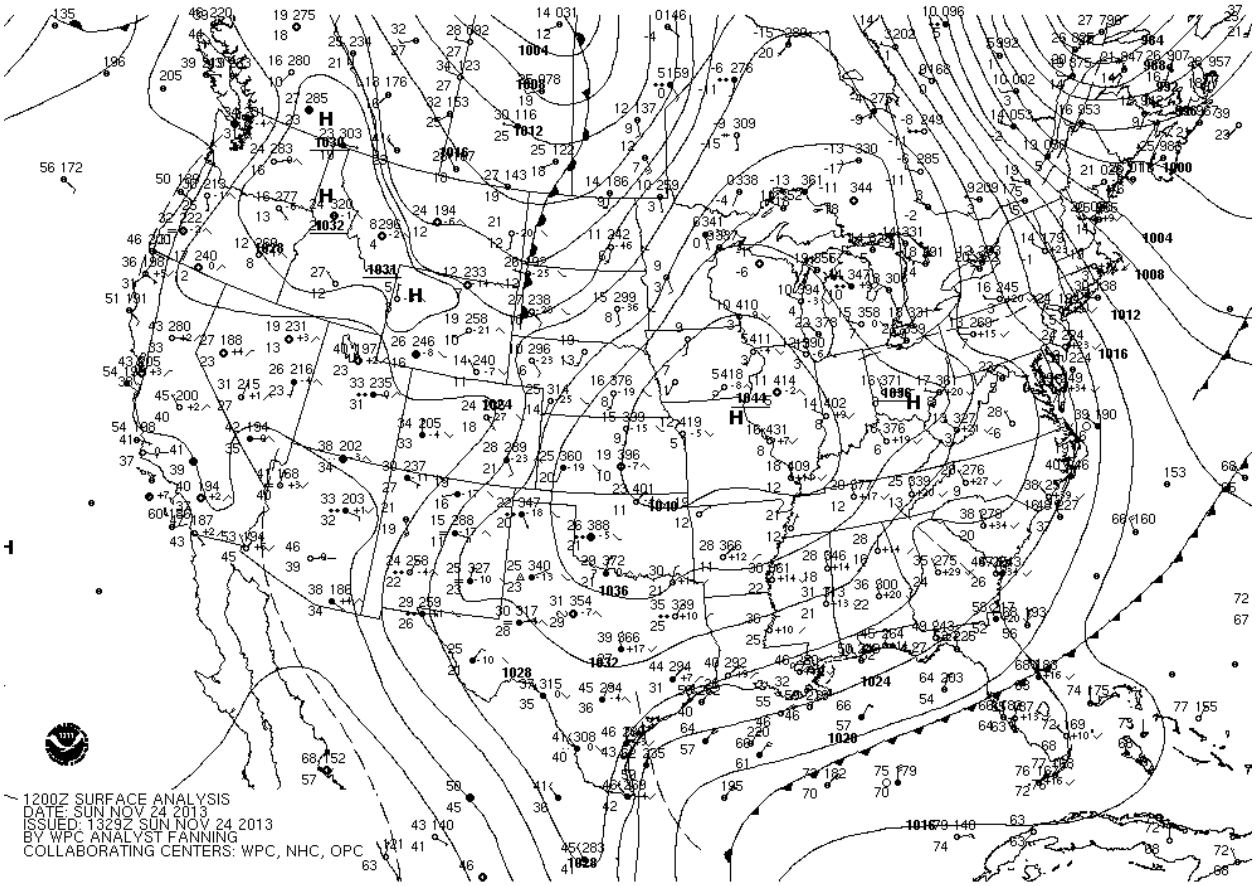

Figure 6.5: Surface analysis for 24 Nov 2013 12Z. Normal meteorological symbols are plotted. Generated from http://www.hpc.noaa.gov

7x7 diabatic, and 7x7 adiabatic fields were 0.322, 0.089, and 0.127, respectively. Also, of important note is that this day, in particular, had the overall best correlation values for all three fields. All correlations were above 0.70, coupled with standard deviations below 0.50, and RMSE values below 1.0.

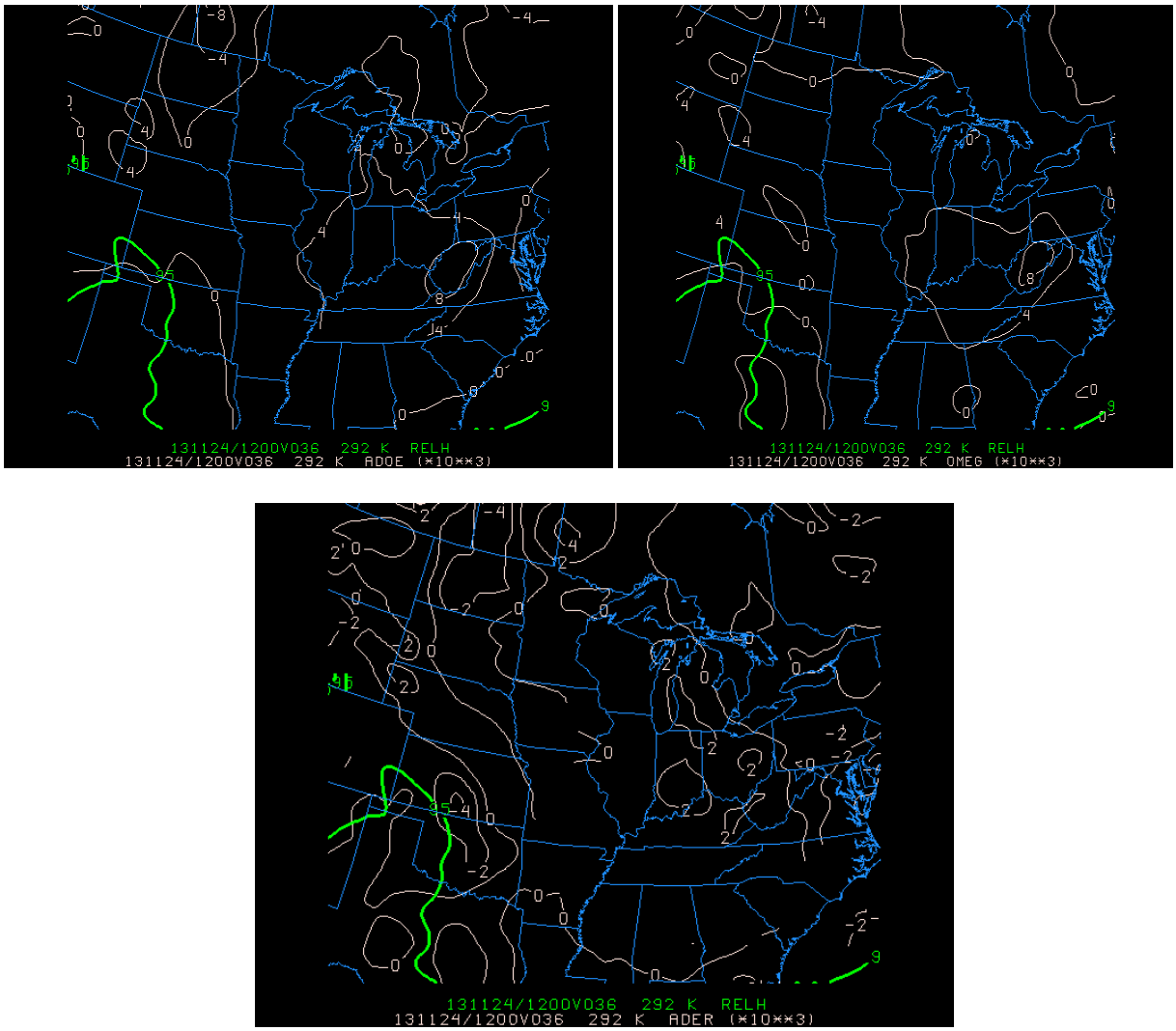

Figure 6.6: Same as Figure 6.1, but for 23 Nov 2013 00ZF036 292K

Chapter 7: Discussion

From the data presented, it has been shown that the inclusion of a quantitative diabatic term:

$$\frac{\partial p}{\partial \theta}\frac{d\theta}{dt} = \omega_{adia} - \omega_{adia}\left[1 - \frac{\Gamma_m}{\Gamma_d}\frac{\theta}{\theta_e}\frac{\partial \theta_e}{\partial p}\frac{\partial p}{\partial \theta}\right] \tag{7.1}$$

to the entire isentropic vertical motion equation:

$$\omega = \frac{dp}{dt} = \frac{\partial p}{\partial t} + \vec{V}\cdot\nabla_\theta P + \frac{d\theta}{dt}\frac{\partial p}{\partial \theta} \tag{7.2}$$

yielded a redefined version of calculating vertical motion in isentropic coordinates:

$$\omega_\theta = \omega_{adia} + \omega_{adia} - \omega_{adia}\left[\frac{\partial \theta}{\partial p} - \frac{\Gamma_m}{\Gamma_d}\frac{\theta}{\theta_e}\frac{\partial \theta_e}{\partial p}\right] \tag{7.3}$$

where ω_{adia} is equal to the sum of the first two terms on the RHS of (7.2). There were a few major assumptions into the development of the expression that are worth noting.

The first has been mentioned previously concerning the adiabatic component and the LCL. Since the exact level of the LCL was not calculated for this experiment, there was no precise calculation of the vertical height of the 292K and 300K isentropic surfaces. One of the major disadvantages of isentropic surfaces is the exact calculation of the Lagrangian change of potential temperature of time as it disrupts the continuity of the isentropic surfaces. The closer to the planetary boundary layer the isentropic surfaces exist will subject them to greater diurnal cycles of solar/terrestrial heating/cooling, causing the surfaces to move up/down within consecutive radiosonde launches, ultimately disrupting their continuity. Assuming the background vertical motion is entirely adiabatic has its limitations, especially within the boundary layer. Further research into calculating the actual thermodynamic effects impinged upon the isentropic surfaces by diabatic effects such as latent and solar heating could further benefit the accuracy of (7.3). This would allow for the background vertical motion to calculate diabatic heating which should, in theory, decrease the overall values of ADER.

The second assumption is the moist and dry adiabatic lapse rates within (7.3). For this experiment, it was noted that Γ_m and Γ_d were both fixed at 6.5 K km^{-1} and 10 K km^{-1}, respectively. However, in the atmosphere, Γ_m is not fixed but variable; its value changes drastically within the planetary boundary layer. For example, Figure 7.1 is a normal blank skew-t diagram for plotting atmospheric sounding data. The lime-green lines sloping from the top-left of the diagram towards the bottom right are dry adiabats, fixed at ~10 K km^{-1}. The dry adiabatic lapse is termed so simply because the air is unsaturated; i.e. a parcel is not at 100% RH. The adiabatic portion implied dQ = 0 into or out of the parcel of air. When the parcel is ascending vertically in the atmosphere, pressure decreases causing the parcel to expand, causing work on the ambient atmosphere. Since the parcel gains no heat with its surroundings, its internal energy decreases, ultimately decreasing its temperature at a rate of ~10 K km^{-1}. Contours of the moist adiabatic lapse rate in Figure 7.1 are denoted by the dashed aqua-colored lines existing vertically from the abscissa and eventually flowing parallel to Γ_d as elevation increases. For the moist adiabatic lapse rate, latent heating is accounted for which accounts for the main difference between the two lapse rate's values. As water condenses, heat is released within a parcel of air which will ultimately decrease the dT as the parcel ascends vertically in the atmosphere. With aid from the Clausius-Clapeyron equation:

$$\mathrm{e_s(T)} = 6.1094 \exp\left(\frac{17.625\mathrm{T}}{\mathrm{T}+243.04}\right) \tag{7.4}$$

where $\mathrm{e_s(T)}$ is the saturation vapor pressure at a given temperature, T, it can be seen that warmer air can hold an exponentially larger amount of water vapor than colder air. Since the largest pressures occur near the surface, warmer air is generally found in the planetary boundary layer, which would follow that there is ultimately more moisture in the lower levels of the atmosphere. Therefore, the moist adiabatic lapse rate is actually non-constant with height, due to the dependence of saturation on temperature is exponential via (7.4). Thus, 6.5 K Km^{-1} for a fixed value is physically

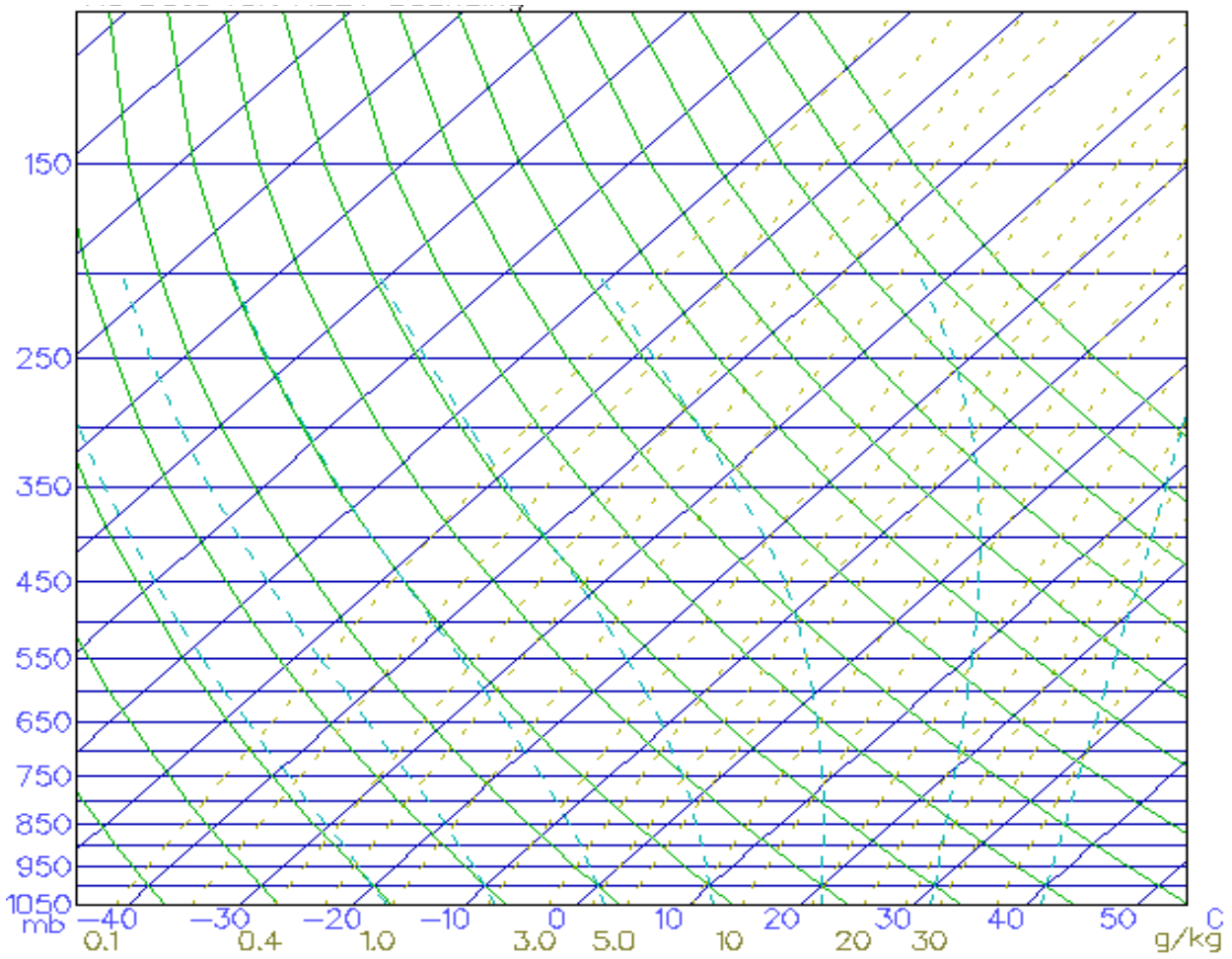

Figure 7.1: Sample blank skew-t diagram. Adapted from http://weather.unisys.com/

unrealistic, but a decent approximation. Further research should be taken to account for the actual value of Γ_m along a specific isentropic surface to aid more realistic results and decreasing the value of ADER.

The third assumption has been mentioned in Chapter 6 concerning θ_e. GEMPAK calculates the equivalent potential temperature through the equation provided by Bolton (1980). However, as outlined in Davies-Jones (2009), θ_e can be calculated through several different equations, one of which he shows to be more accurate than eqn. (6.2). A similar study accounting

for different methods of calculating θ_e could prove a useful analytical tool to further the improvement of the equation derived in this work.

This study was conducted during the cool season of 2013/2014, where convection is generally suppressed more-so than the summer months. It could be argued that the developed expression (7.3) performed appreciably well, and should be taken to events where extreme convection occurs. A possible term-by-term analysis could also provide useful insight into whether any certain terms perform better or worse under specific atmospheric conditions.

Upon closer observation to the actual fields of ADER revealed something interesting. There was an apparent dipole within the fields of ADER that would randomly occur (e.g., Figures 7.2, 7.3, and 7.4). Figure 7.2 was taken from the 02 Nov 2013 00F030 300K run, where several dipoles can be observed. Although the shape of these dipoles are not exactly the same, they are strikingly similar. For instance, the closed-contours of 6 μbs^{-1} and -6 μbs^{-1} over Cincinnati and Pittsburgh, respectively, have a pattern very similar to the same values contours over southeastern Nebraska and central Iowa, respectively. These dipole moments would appear to have a zonal pattern, but a meridional pattern is observed near Nashville, Tennessee and central Indiana. One more could be argued to exist over southwestern Minnesota and eastern North Dakota. Figure 7.3 displays one of these areas over eastern Kansas and northern Missouri, whereas an extreme example is observed in Figure 7.4 over southwestern Iowa and the Illinois-Indiana border. Note, all of these images were taken from separate isentropic levels, forecasted times, dates, and initialization times. No apparent pattern can be detected amongst sea-level patterns, height fields, or synoptic-scale occurrences that would cause these moments. Distance between the dipoles and preferential direction as either meridional or zonal appears random as well.

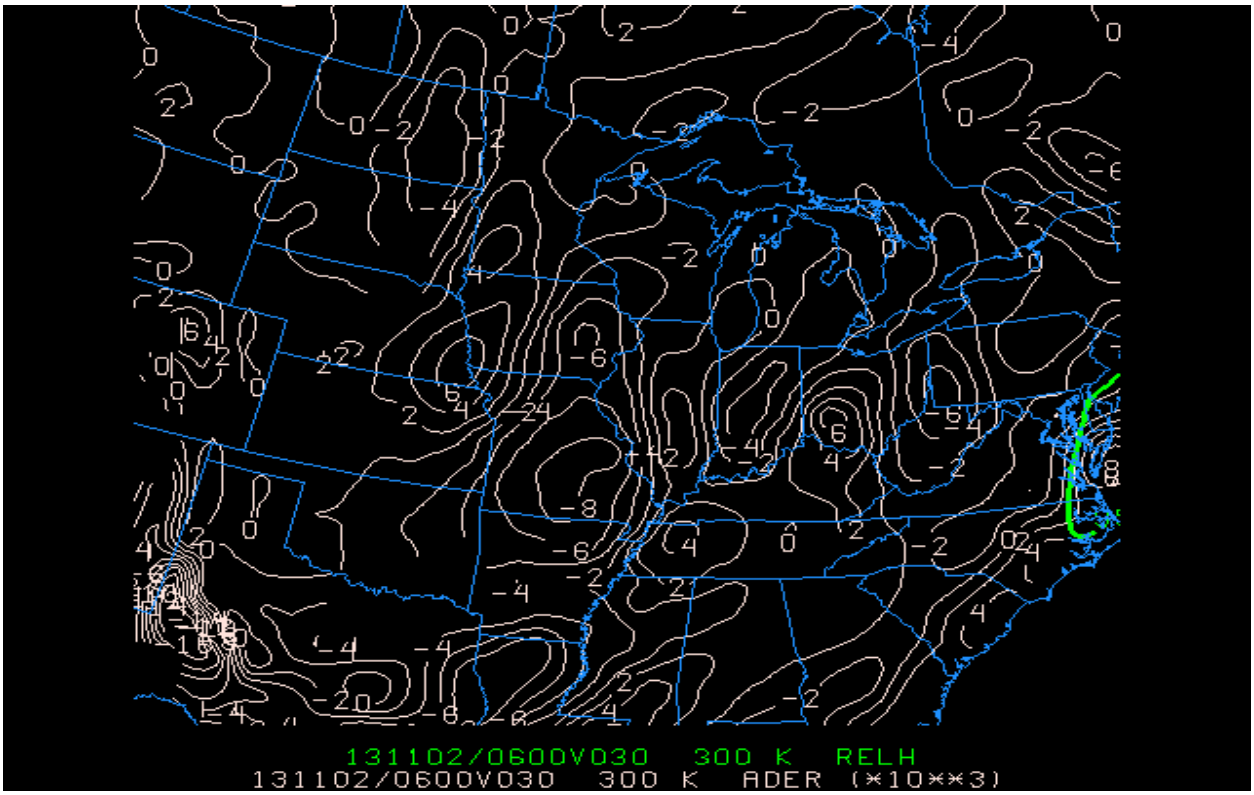

Figure 7.2: GEMPAK generated image from the 02 Nov 2013 00F030 300K run showing several dipole moments over the CONUS.

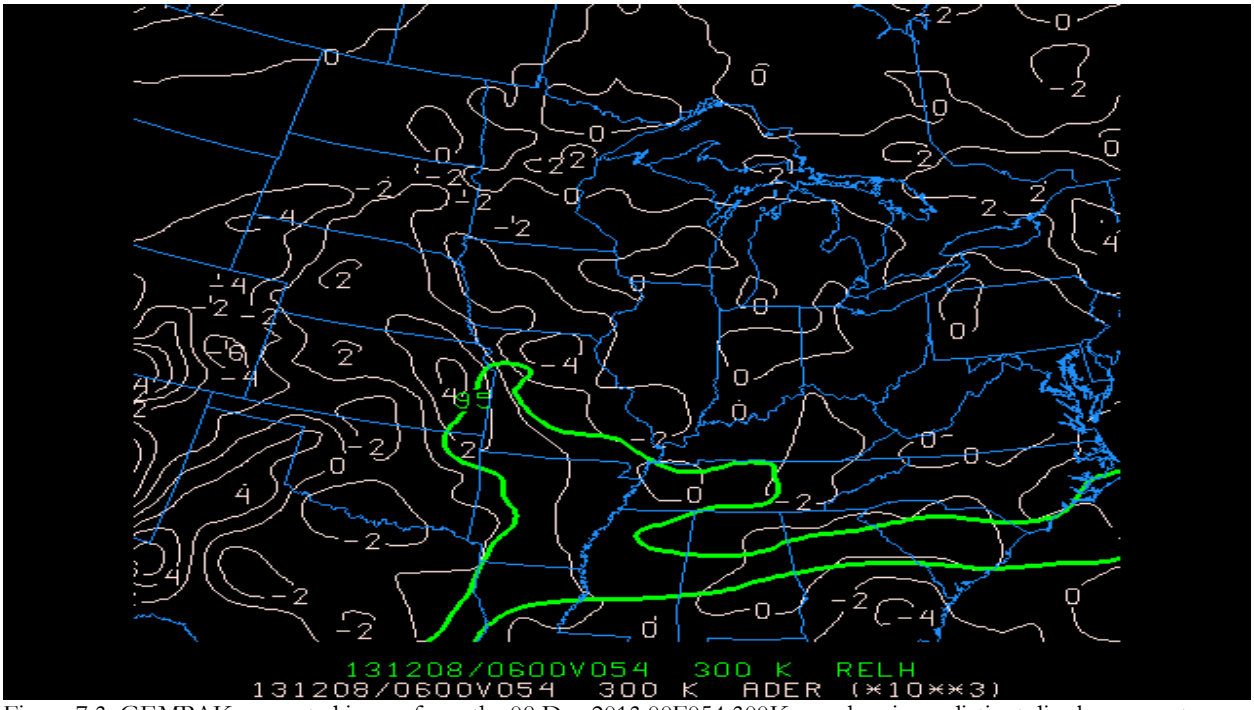

Figure 7.3: GEMPAK generated image from the 08 Dec 2013 00F054 300K run showing a distinct dipole moment over eastern Kansas and northern Missouri.

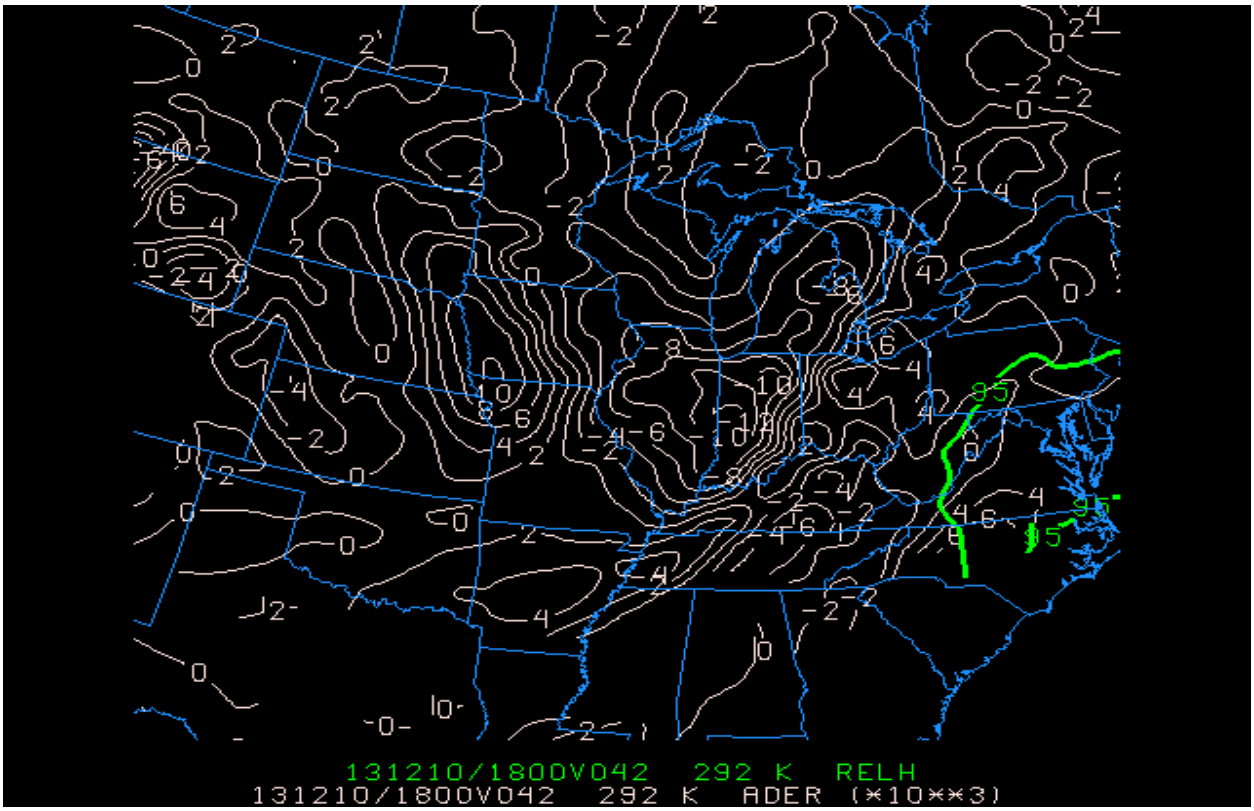

Figure 7.4: GEMPAK generate image for the 10 Dec 2013 12F042 300K run showing an extreme case of a dipole moment over southwestern Iowa and the Illinois-Indiana border.

Chapter 8: Conclusion and Final Remarks

For this study, the development of a new method of calculating isentropic vertical motion was implemented for the cool season of 2013/2014. Through the data analyzed, several important aspects of the developed expression came to fruition:

1) ADOE on the 17x17 grid performed nearly an order of magnitude worse than the ADOE 7x7 grid. This was primarily due to the fact that 17 grid points horizontally spaced 80km apart encompassed most of the CONUS.
2) The 7x7 ADOE performed nearly identically to the 7x7 ADIA field, yet was generally outperformed by a marginal amount. The overall average ADER was half of the ADIA error.
3) There was little to no average correlation for the 7x7 fields. The 17x17 field, however, displayed a coherent increase in the correlation of ADOE to OMEG as the forecasted times increased from the initialization times. In fact, the 17x17 F048 average correlation was the only time the 17x17 grid for any parameter outperformed either of the 7x7 grids.
4) There was a general decreasing trend in error from OMEG as the forecasted times increased from the initialization time, with the 17x17 grid detailing a more prominent trend.
5) The 12Z (292K) data generally performed better than 00Z (300K). The lower isentropic surface was expected to perform better primarily due to a lack of solar radiation effects. Also, the fact that more moisture should exist in the lower levels of the atmosphere should aid in the calculation of ADOE.

6) A day-by-day analysis of comparing the diabatic to the adiabatic isentropic vertical velocity equation revealed that 70% of the time, inclusion of the diabatic term outperformed the adiabatic equation.
7) ADOE appeared to display a bias for specific meteorological events. It performed poorly in regions where:
    a. A strong cold front existed
    b. Cyclogenesis was occurring
    c. Merging of two cyclones
    d. Proximity to a large body of water
    e. Warm sector of a mid-latitude cyclone

ADOE seemed to perform exceptionally well in regions where convection was not intense, or in areas where the static stability generally remained the same. Therefore, along a cold frontal boundary, which is primarily characterized as a strong region of static stability, would disrupt the calculations of ADOE; strong static stability gradients disrupt the calculations of ADOE. Certain other meteorological parameters, such as the LCL should be obtained to help aid in the calculation of the adiabatic portion of ADOE.

Overall, the experiment proved that the derived equation performed well on a daily basis, and exceptionally well when averaged over the cool season of 2013/2014. This new method of calculating vertical motion in isentropic space should be appealing to WFO's east of the Rockies (or well west where isentropic surfaces of 292K and 300K tend not to intersect the ground at such high elevations), as it provides a simpler means of estimating the diabatic term in the isentropic vertical velocity.

References

Abbe, C., 1901: The physical basis of long-range weather forecasts. *Mon. Wea. Rev.,* **29**, 551-561.

Ashford, O.M., 1985: *Prophet or professor? The life and work of Lewis Fry Richardson*. Adam Hilger Ltd, Bristol. 304 pp.

Arakawa, A., 2004: The Cumulus Parameterization Problem: Past, Present, and Future. *J. Climate*, **17**, 2493–2525.

Barnes, S.L., F. Caracena, and A. Marroquin, 1996: Extracting synoptic-scale diagnostic information from mesoscale models: The Eta model, gravity waves, and quasigeostrophic diagnostics. *Bull. Amer. Met. Soc.*, **77**, 519-528.

Benjamin, S.G., G.A. Grell, J.M. Brown, and T.G. Smirnova, 2004: Mesoscale weather prediction with the RUC hybrid isentropic-terrain-following coordinate model. *Mon. Wea. Rev.*, **132**, 473-493.

Bennetts, D.A. and B.J. Hoskins, 1979: Conditional symmetric instability – a possible explanation for frontal rain-bands. *Q. J. R. Meteor. Soc.,* **105**, 945-62.

Bleck, R., 1973: Numerical forecasting experiments based on the conservation of potential vorticity on isentropic surfaces.*J. Appl. Meteor.,* **12**, 737-752.

_____, 1978: On the use of hybrid vertical coordinates in numerical weather prediction models. *Mon. Wea. Rev.*, **106**, 1233-1243.

Bolton, D., 1980: The computation of equivalent potential temperature. *Mon. Wea. Rev.*, **108**, 1046–1053.

Byers, H.R., 1938: On the thermodynamic interpretation of isentropic charts. *Mon. Wea. Rev.,***66**, 63-68.

Cammas, J.P., D. Keyser , G.M. Lackmann, and J. Molinari, 1994: Diabatic redistribution of potential vorticity accompanying the development of an outflow jet within a strong extratropical cyclone. Preprints, *Int. Symp. on the Life Cycles of Extratropical Cyclones,* Vol. II, Bergen, Norway, Geophysical Institute, University of Bergen, 403–409.

Charney, J.G., R. Fjȍrtoft, and J. Neumann, 1950: Numerical integration of the barotropic equation. *Tellus*, **2**, 237-253.

Colman, B.R., 1990: Thunderstorms above frontal surfaces in environments without positive CAPE. Part II: Organization and instability mechanisms. *Mon. Wea. Rev.,* **118**, 1103-1121.

Danielsen, E.F., 1961: Trajectories: Isobaric, isentropic and actual. *J. Meteor., **18**,* 479-486.

Davies-Jones, R., 2009: On formulas for equivalent potential temperature. *Mon. Wea. Rev.*, **137**, 3137-3148.

Eddy, A., 1967: Statistical objective analysis of scalar data fields. *J. Appl. Meteor.,* **6**, 597-609.

Eliassen, A. and E. Kleinschmidt, 1957: Dynamic Meteorology. *Handbuch der Physik,* **48**, Berlin, Springer-Verlag, 1-154.

Emanuel, K.A., 1985: Frontal circulations in the presence of small moist symmetric stability. *J. Atmos. Sci.*, **42**, 1062-1071.

_____, M. Fantini, and A.J. Thorpe, 1987: Baroclinic instability in an environment of small stability to slantwise moist convection. Part I: Two-dimensional models. *J. Atmos. Sci.,* **44**, 1559-1573.

Ertel, H., 1942: Ein neuer hydrodynamischer Erhaltungssatz. *Naturwiss.,* **30,** 543–544.

Han, J. and H. Pan, 2011: Revision of convection and vertical diffusion schemes in the NCEP Global Forecast System. *Wea. Forecasting*, **26**, 520–533.

Hess, S. L., 1959: *Introduction to Theoretical Meteorology.* Holt, Rinehart, and Winston, New York. 362 pp.

Janjic, Z. I., 2000: Comments on "Development and evaluation of a convection scheme for use in climate models". *J. Atmos. Sci.*, **57**, 3686.

Kain J. S., 2004: The Kain–Fritsch convective parameterization: An update. *J. Appl. Met.,* **43**, 170–181.

Keyser, D.A., and D.R. Johnson, 1984: Effects of diabatic heating on the ageostrophic circulation of an upper tropospheric jet streak. *Mon. Wea. Rev.*, **112**, 1709-1723.

Lorenz, E.N., 1963: Deterministic nonperiodic flow. *J. Atmos. Sci.,* **20**, 130–141.

Lynch, P., 2008: The Origins of computer weather prediction and climate modeling. *Jour. Comp. Phys.*, **227**, 3431-3443.

Mack, C.A., 2011: Fifty years of Moore's Law. *IEEE Trans. Semiconduct. Manufact,* **24**, 202-207.

Market, P.S., J.T. Moore, and S.M. Rochette, 2000: On calculating vertical motions in isentropic space. *Natl. Wea. Dig.*, **24**, 31-37.

_____, S.M. Rochette, and A.R. Lupo, 2012: A comparison of modern and historical methods for calculating Montgomery streamfunction. *Atm. Sci. Letts.,* **14**, 41-43.

Mellor, G.L., and T. Yamada, 1974: A hierarchy of turbulence closure models for planetary boundary layers. *J. Atmos. Sci.*, **31**, 1791-1806.

Moore, G. E., 1965: Cramming more components onto integrated circuits. *Electronics*, **38**, 114-117.

Moore, J.T., 1993: *Isentropic analysis and interpretation: Operational applications to synoptic and mesoscale forecast problems.* National Weather Service Training Center, Kansas City, MO, 99 pp.

_____, and T.E. Lambert, 1993: The use of equivalent potential vorticity to diagnose regions of conditional symmetric instability. *Wea. Forecasting*, **8**, 301-308.

_____, A.C. Czarnetzki, and P.S. Market, 1998: Heavy precipitation associated with elevated thunderstorms formed in a convectively unstable layer aloft. *Meteorol. Appl.,* **5**, 373-383.

Ninomiya, K., 1971: Mesoscale modification of synoptic situations from thunderstorm development as revealed by ATS III and aerological data. *J. Appl. Meteor.,* **10**, 1103-1121.

Oliver, V.J. and M.B. Oliver, 1951: Meteorological analysis in the middle latitudes. *Compendium of Meteor.,* Amer. Meteor. Soc., 715-727.

Orlanski, I., 1975: A rational subdivision of scales for atmospheric processes. *Bull. Amer. Meteor. Soc.*, **56**, 527–530.

Pedlosky, J., 1992: *Geophysical Fluid Dynamics,* 2nd Ed., Springer-Verlag, 710 pp.

Petersen, R.A., and J.H. Homan, 1989: Short-range forecasting and nowcasting using a simple, isentropic prediction model. *Wea.and Fore.,* **4**, 5-23.

Petterssen, S., 1956: *Weather Analysis and Forecasting*, 2nd Ed., **1**. New York, McGraw-Hill, 320-339 pp.

Richardson, L.F., 1922: *Weather Prediction by Numerical Process*. Cambridge University Press, Cambridge. 236 pp.

Rochette, S.M., J.T. Moore, and P.S. Market, 1999: The importance of parcel choice in elevated CAPE computations. *Natl. Wea. Dig*, **23**, 20-32.

Rossby, C. G., 1932: Thermodynamics applied to air mass analysis. *MIT Meteorology Papers 1*, No. 3. 48 pp.

Saucier, W.J., 1955: *Principles of Meteorological Analysis*. University of Chicago Press, 438 pp.

Starr, V.P., 1945: A quasi-Lagrangian system of hydrodynamical Equations. *J. Meteor.,***2**, 227-237.

Sutcliffe, R. C., 1947: A contribution to the problem of development. *Quart. J. Roy. Meter. Soc.,* **73**, 370-383.

Uccellini, L.W., 1976; Operational diagnostic applications of isentropic analysis. *Natl. Wea. Dig.,* **1**, 4-12.

Webster, S., J. Thuburn, B. Hoskins, and M. Rodwell, 1999: Further development of a hybrid-isentropic GCM. *Quart. J. Roy. Meteor. Soc.*, **125**, 2305-2331.

Wilks, S, Daniel, 2011: *Statistical Methods in the Atmospheric Sciences*. International Geophysics Series, Vol. 100, Academic Press, 464 pp.

Yang, F., 2011: Review of NCEP GFS forecast skills and major upgrades. Presented in oral session, American Meteorological Society 91st Annual Meeting, Seattle, WA.